Lin, Yan (2011) Investigating stimulus induced metabolic changes in human visual cortex using functional magnetic resonance spectroscopy at 7T. PhD thesis, University of Nottingham.

Access from the University of Nottingham repository:
http://eprints.nottingham.ac.uk/14589/1/555737.pdf

Copyright and reuse:

The Nottingham ePrints service makes this work by researchers of the University of Nottingham available open access under the following conditions.

- Copyright and all moral rights to the version of the paper presented here belong to the individual author(s) and/or other copyright owners.
- To the extent reasonable and practicable the material made available in Nottingham ePrints has been checked for eligibility before being made available.
- Copies of full items can be used for personal research or study, educational, or not-for-profit purposes without prior permission or charge provided that the authors, title and full bibliographic details are credited, a hyperlink and/or URL is given for the original metadata page and the content is not changed in any way.
- Quotations or similar reproductions must be sufficiently acknowledged.

Please see our full end user licence at:
http://eprints.nottingham.ac.uk/end_user_agreement.pdf

A note on versions:

The version presented here may differ from the published version or from the version of record. If you wish to cite this item you are advised to consult the publisher’s version. Please see the repository url above for details on accessing the published version and note that access may require a subscription.

For more information, please contact eprints@nottingham.ac.uk

Investigating Stimulus Induced Metabolic Changes In Human Visual Cortex Using Functional Magnetic Resonance Spectroscopy at 7T

by

YAN LIN, MD

Thesis submitted to the University of Nottingham for
the degree of Doctor of Philosophy

July 2011

Abstract

This thesis concerns the investigation of metabolic changes in ^{1}H metabolite levels in the human visual cortex due to visual stimulation using proton magnetic resonance spectroscopy (^{1}H-MRS) at 7T. The work described in this thesis has been undertaken by the author and collaborators at the Sir Peter Mansfield Magnetic Resonance Centre at the University of Nottingham.

Detection of functional changes in ^1H metabolites may enable a greater understanding of neurotransmitter activity and metabolic pathways used for energy synthesis during activation of brain tissue. Previous ^{1}H MRS studies of the activated human brain mainly focused on observing lactate (Lac) changes. More recent studies by Mangia *et al*, taking advantage of the increased signal and spectral resolution at 7T, have investigated the change in the level of Lac, glutamate (Glu), Aspartate (Asp) and Glucose (Glc) during activation. However, Mangia did not measure significant change in the level of gamma aminobutyric acid (GABA) and Glutamine (Gln), which might be expected to change due to increased neurotransmitter cycling rates during activation.

Given that the metabolite changes observed due to visual stimulation were relatively small. We used a long, intense visual stimulus, designed to retain attention, to confirm and quantify the changes in the levels of Glu, GABA, and Gln, and to further investigate the Lac and Asp response to visual stimulation. Our present re-

sults using a moving stimulus of full-screen flickering contrast-defined wedges, have demonstrated many more metabolic changes throughout two different time scales of stimulation. Small ($2 \sim 11\%$) but significant stimulation induced increases in Lac, Glu and glutathione (GSH) were observed along with decreases in Asp, Gln and glycine (Gly). In addition, decreases in (intracellular) Glc and increases in GABA were seen but did not reach significance. The opposite changes in Glu and Asp are indicative of increased activity of the malate-aspartate shuttle, which taken together with the opposite changes in Glc and Lac reflect the expected increase in brain energy metabolism. The increases in Glu and GABA coupled with the decrease in Gln can be interpreted in terms of increased activity of the Glu/Gln and Gln/Glu/GABA neurotransmitter cycles. An entirely new observation is the increase of GSH during prolonged visual stimulation. The similarity of its time course to that of Glu suggests that it may be a response to the increased release of Glu or to the increased production of reactive oxygen species. Gly is also a precursor of GSH and a decrease on activation is consistent with increased GSH synthesis. Together these observations constitute the most detailed analysis to date of functional changes in human brain metabolites.

Interestingly, the Lac response was confined to the first visual stimulus. It is possible that processes triggered during the first period of visual stimulation, could continue for a while after stimulation has ended. If this is an important mechanism of the activity-stimulated brain Lac response, shortening the duration of the first stimulus might lead to an increase in Lac response during the second period of stimulation. With this in mind, we designed a repeated visual stimulation paradigm, varying the duration of the first stimulation (shorter than 9.9-min, based on our previous results), to see the effect on the Lac response during the second visual stimulation period. A gradual increase in Lac under the prolonged stimulation, following the first brief stimulation (1s, 16s and 48s, respectively), was observed and maintained until the end of these

periods. Lac responses during the second stimulation period looked similar whether the first stimulation was 1s or 16s. With the increase of first visual stimulus duration (48s), the Lac response under the second stimulation period was slightly diminished. No significant Lac accumulation can be evident to the second stimulation, when the initial stimulation was 288s. The averaged Lac level was considerably below baseline after cessation of the first 288s stimulus. It is possible that the increased glycolytic flux, triggered during the initial longer stimulation, would still continue for a while during recovery, accounting for the decreased brain Lac level during resting periods from stimulation. Further experiments are ongoing, varying the duration of the second resting periods, to see the effect on the Lac response to the second stimulation.

Keywords MR spectroscopy; visual stimulation; energy metabolism; neurotransmitters; lactate; malate aspartate shuttle; antioxidants.

Acknowledgements

Although my name is written on the first pages of this thesis, the work presented is in reality the combined efforts of a number of people, to all of whom, I owe a great deal.

Firstly, I would like to express many thanks to my supervisor Professor Peter Morris, whose strong support, excellent advice, creative ideas, and accessibility has been invaluable to me throughout my PhD in Nottingham. I am very much indebted to Mary Stephenson for her professional technical assistance and useful discussions on different aspects of this work I will be forever grateful for.

I would like to acknowledge Xin Lijing, from Centre d'Imagerie BioMedicale (CIBM) of the UNIL, UNIGE, HUG, CHUV and EPFL, Switzerland, for making available to me their LCModel basis dataset. I also thank Antonio Napolitano, Sam Wharton and Olivier E. Mougin for their assistance in MATLAB programming and Denis Schluppeck for providing the visual stimulus. Continuing on a professional level, I would like to thank Andy Peters, for his kind help on the technical aspects of the 7T scanner and software.

Throughout my time at SPMMRC I have been surrounded by great people. Thank you so much to my good office friends Sam, Gerda, Steve, Glyn, Andre, Amany, Olivier, Rosa, Dan, Mo etc, and all other nice people at the MR centre, who have made my

time in Nottingham such an enjoyable and memorable experience.

I would like to thank Prof Wu Ren Hua and Frieda from Shantou University Medical College, China, for their strong support and encouragement during my PhD study in Nottingham. I also gratefully acknowledge the Medical Research Council for Programme Grand Support and for a Dorothy Hodgkin Postgraduate Award (YL) in partnership with GlaxoSmith Kline.

Finally and most importantly is the appreciation I reserve for my family. I am eternally grateful to my husband and my Mum who have always given me the love, support and enthusiasm I have needed throughout my education.

Contents

7 Dynamics of stimulus-induced lactate changes in human visual cortex detected by ^{1}H MRS at 7T 130

Chapter 1

Introduction

1.1 ^{1}H-MRS studies of human brain metabolism under visual stimulation

Magnetic Resonance Spectroscopy (MRS) is a non-invasive method that allows the measurement of the concentrations and synthesis rate of individual metabolites in the brain and other organ systems in precisely defined regions guided by MR imaging (MRI). MRS techniques have advanced significantly over the last several decades and can be performed on any nucleus possessing a magnetic moment. *In vivo* the nuclei mainly used include ^{1}H, ^{13}C and ^{31}P. The proton (^{1}H) is the most commonly employed nucleus in the brain, due to its high abundance and sensitivity *in vivo*. A number of metabolites including N-acetyl-L-aspartate (NAA), creatine (Cr), choline (Cho), myo-inositol (mIn) and Lac etc, can be potentially measured by ^{1}H-MRS at low field. Higher field strengths allow many more metabolites levels to be reliably measured, up to 20 at 7T[1, 2], including those involved in neurotransmission, Glu, GABA and Gln.

The issue of neuronal activation metabolism was raised by the observation obtained with PET by Fox *et al.*[3, 4], who found an uncoupling between oxygen and Glc consumption, suggesting a focal mismatch between the variations of $CMRO_2$ (cerebral metabolic rate of oxygen, 5%), CMR_{glc} (cerebral metabolic rate of Glc, $30 \sim 50\%$) and CBF (cerebral blood flow, $30 \sim 50\%$) during prolonged stimulation. They suggested the possibility that certain types of functional activity might selectively stimulate anaerobic glycolysis. The ^1H MRS method can provide interesting experimental evidence on this metabolic issue, since it is a valid tool for investigating human metabolism *in vivo* allowing direct measurement of metabolic changes during neuronal activation through continuous acquisition of MR spectra. By means of such an approach, a biphasic time course of Glc concentration due to 30 min of photic stimulation was observed by Chen *et al.*[5]. They found an initial decrease of Glc followed by a slow increase toward baseline. They utilized simple Michaelis-Menten kinetic modelling to obtain the variation of CMR_{glc}, which was estimated to increase by 22% during stimulation. Glc consumption during the stimulation has also been observed in other ^1H MRS studies[6].

The metabolic events of energy cost during functional activity remain subject to intense debate. The human brain has a high energy requirement. Even though it constitutes only 2% of the body's weight, the brain accounts for almost 20% of the global resting metabolism. Glc has been traditionally considered as the primary energy source for neurons and its consumption rate increases up to 50% when the brain responds to external stimuli[7, 8, 9]. But several lines of *in vitro* and *in vivo* evident have demonstrated that a number of compounds, such as Lac, Pyr, acetate (Ace), Glu, Gln, can also be oxidized by neurons[10], serving as an alternative oxidative substrate to fuel brain cells[11]. Among the substrates for energy generation, Lac plays a crucial role in energy homeostasis in both physiological and pathological conditions[12], and has been receiving special attention in the human activated brain. Lac was reported to be equivalent to Glc with regard to its easy access to the neuronal tricarboxylic acid (TCA) cycle [13]. Furthermore, Lac has been proposed to have some advantages compared to Glc during neuronal activation, since it can be converted to Pyr in the absence of ATP [14].

Research over the past two decades has renewed interest in Lac, which is no longer regarded as an useless end product of anaerobic glycolysis[15, 16], but as an oxidative substrate for energy metabolism. ^{1}H MRS has been used in a number of studies, under a variety of experimental conditions and functional paradigms, to non-invasively assess the temporal changes of Lac in the activated human brain[17, 18, 7, 6, 19, 20, 21, 22, 23]. Though studies observing Lac during stimulation have come to various different conclusions, much evidence indicates that Lac does play a major role in aerobic energy metabolism in the brain. ^{1}H MRS studies showing increased Lac during neuronal activation support a broader role for Lac in brain energy metabolism than was traditionally recognized[17, 18, 7, 6, 19, 20, 21, 22, 23]. Using ^{1}H MRS, Prichard et al.[17], first reported changes in Lac level during sustained visual stimulation, measuring a 60% increase in Lac level during the first six minutes of activation, followed by a decrease back towards baseline over the following 15-20 minutes. Sappey-Marinier *et al.*[18] measured up to a 250% increase of Lac in the first 6.4 min during visual stimulation and return towards baseline during the second 6.4 min block. Frahm *et al.*[6] observed a 68% increase in the Lac level during the first half of a 6 min stimulation period, followed by a decrease to the basal level during ongoing stimulation. Since sustained visual stimulation is not associated with hypoxia [6, 23], these findings of increased Lac under stimulation argue against the historical view that hypoxia is the precondition for Lac production. However, the feasibility of measuring Lac changes under stimulation has been challenged by other authors: Merboldt *et al.*[7] could not detect any reproducible time-course of Lac during several kinds of visual stimulation; Boucard *et al.*[19] failed to detect any Lac signal during prolonged stimulation. The results described above are not unanimous, probably due to low Lac concentrations and to different experimental conditions.

More recent studies by Mangia *et al.*[23], taking advantage of the increased SNR and spectral resolution at 7T, with ultrashort TE and a long TR, have investigated many more metabolic changes under two paradigms of visual stimulation lasting 5.3 and 10.6 minutes. They observed significant increased Lac and Glu and decreased Asp, Glc also showed a tendency to decrease during activation. The decreased Glc with increased Lac suggests an increase oxidative energy metabolism, which is further sustained by an increase in the activity of the malate-asparate shuttle (MAS), reflected in the increase in Glu and decrease in Asp concentrations as a consequence of the rate limiting Glu-Asp antiporter at the inner mitochondrial membrane. This work has significantly improved our understanding of how brain energy metabolism underpins brain function. It was well established that increased Glc oxidation due to stimulation could be coupled with the increased neurotransmitter cycling fluxes [24]. Therefore, observations of increased Glu due to the stimulation might be expected to be accompanied by changes in Gln or GABA, due to increased cycling rates during activation. However, these changes were not seen. Also, the observed Lac level during activation at 7T by Mangia *et al.*[23] is different from those measured by Pritchard and Sappey-Marinier, which may be due to differences in experimental protocol. Pritchard and Sappey-Marinier used long TE PRESS sequences to measure Lac, which result in underestimation, as Lac is in a "short T_2 pool", whilst Mangia *et al.* used an ultra-short TE (6ms) and long TR(5s) STEAM sequence, which minimizes T_2 and T_1 relaxation effects, and, ultimately leads to very reproducible results with a high SNR.

Despite the increased reliability of metabolite quantification attainable at ultra-high fields, the temporal and spatial resolution of functional ^{1}H MRS does not provide direct evidence to differentiate the contributions of the neuronal and astrocytic compartments, because the measured signal is averaged from a relatively large volume of cortex. However, ^{13}C MRS with ^{13}C-labelling substrates, can be used to discriminate glutamatergic (excitatory) and GABAergic (inhibitory) neuronal activity and allows determination of the separate rates of Glc oxidation in these cell types as well as neurotransmitter cycling and TCA cycle rates[25, 26, 27, 28, 29, 30, 31]. More detailed information related to ^{13}C MRS is discussed in the following section.

1.2 General information about ^{13}C-MRS

^{13}C-MRS developed 30 years ago is the application of nuclear magnetic resonance with respect to carbon. It is analogous to proton MRS and allows the identification of carbon atoms in an organic molecule just as proton MRS identifies hydrogen atoms. ^{13}C MRS can provide "fingerprints" of organic compounds, due to the carbon atom being the fundamental constituent (backbone) of organic compounds. Advantages of ^{13}C-MRS compared with ^{1}H-MRS are the lack of background signal due to water and its large chemical shift range of 200 ppm, enabling the distinction of individual carbon atom sites within a compound that cannot be resolved by ^{1}H-MRS.

However, the natural abundance for ^{13}C is only roughly 1.1% of the total carbon and its gyromagnetic ratio (γ) is approximately one-fourth of that the proton. These two circumstances make ^{13}C-MRS a relatively insensitive technique. Despite these difficulities, advances in magnet technology and acquisition techniques make ^{13}C MRS a viable tool for studying human brain metabolism. The low abundance of the ^{13}C nucleus can be turned into an advantage through the use of highly enriched ^{13}C-labeled substrates to enhance sensitivity, with little or no background interference from endogenous metabolites. This makes ^{13}C interesting to provide specific and quantitative information about metabolites and metabolic pathways like the tricarboxylic acid (TCA) cycle and the Glu/Gln cycling rate. The high chemical specificity of ^{13}C MRS, can distinguish ^{13}C label incorporation not only into different molecules, but also into specific carbon positions within the same molecule. This enables ^{13}C label incorporation in active metabolites to be followed and measured, such as Glu, Gln, Lac, Asp, non-invasively throughout metabolic pathways. By following the flow of ^{13}C label from Glc, acetate, and other precursors into these metabolites, ^{13}C-MRS can now be used to discriminate glutamatergic (excitatory) and GABAergic (inhibitory) neuronal activity. The first MR observation of the Glu-Gln cycle was by Badar-Gofer*et al.* [32] using ^{13}C labelled acetate in studies of superfused brain slices. Subsequently, ^{13}C labelled glucose studies in humans enabled the cycling rate to be accurately measured [33]. Measuring changes in this rate during visual stimulation has proven to be a challenge in humans[34]. However, in animal studies, it allows us to differentiate the separate rates of Glc oxidation in these cell types as well as neurotransmitter cycling and TCA cycle rates[25, 26, 27, 28, 29, 30, 31].

Metabolic fluxes are not directly measured by ^{13}C MRS, but are obtained on the basis of the adopted mathematical models and experimental conditions. Detail information can be found in Chapter 8.

1.3 Thesis overview

MRS is feasible on any nucleus possessing a magnetic moment. The work presented in this thesis is focused on the investigation of metabolic changes in the human visual cortex under visual stimulation, using functional ^{1}H-MRS at 7T.

Chapter 2 begins with the physical basis of NMR to provide a background to the work carried out. This chapter focus more on the dynamic processes underlying MRI, including T_1 and T_2 relaxation.

Chapter 3 reviews the static aspects of MRS. Factors influencing spectra in MRS are discussed such as chemical shift and J-coupling. The advantages of performing ^1H MRS at higher field strengths (7T), include higher SNR, increased spectral resolution, increased spatial resolution and increased temporal resolution are described. This is followed by a discussion of techniques used for *in vivo* proton MRS and a description is given of ^1H metabolites commonly observed in the human brain. Signal localization techniques of ^{1}H MRS are described, including STEAM, PRESS and water suppression techniques. Spectral quantification is then explained, focusing on acquisition, post-processing and quantification. Finally, general information about ^{13}C MRS is introduced briefly.

Chapter 4 describes the basis of fMRI, which is very much relevant to the work presented in this thesis and includes a discussion of neuronal coupling, Blood Oxygenation Level Dependent (BOLD) contrast and Echo Planar Imaging (EPI).

An initial fMRS study at 7T, used a Light Emitting Diode (LED) goggle stimulus, is described in Chapter 5. Two different spectral quantification methods (QUEST in jMRUI and LCModel) are compared. Using a LCModel basis dataset with 21 metabolites, we found increased Glu compatible with decreased Asp and Gln during two 9.9-min periods of stimulation. Increased Glu with decreased Asp due to stimulation are consistent with previous reports and suggest a stimulus driven increase in oxidative energy metabolism. The opposite changes with increased Glu and decreased Gln might indicate an increase in excitatory neurotransmitter cycling in the visual cortex during stimulation. This work has been presented in May 2010 at the International Society for Magnetic Resonance in Medicine (ISMRM), in Sweden (Stockholm).

Given that the metabolite changes observed due to visual stimulation were relatively small, further experiments were carried out, with a more intense visual stimulus (moving contrast-defined wedges). This is described in Chapter 6 and was designed to elicit larger metabolite changes. The first study consisted of a 6.6 min baseline followed by 13.2 min of visual stimulation and 19.8 min recovery. The aim of this experiment was to confirm and quantify the changes in the levels of Glc, Lac, Glu and Asp and to further investigate GABA and Gln in response to functional visual stimulation, as well as to observe post-stimulus recovery. The second study involved two 9.9 min rest periods interleaved with two 9.9 min stimulation periods, in order to investigate whether the response to further periods of stimulation are identical, or differ from the initial response. These further studies demonstrated a peak in Lac levels followed by a subsequent decline towards baseline during the stimulus, and a failure to rise again on subsequent stimulation. This work was orally presented in May 2011 at ISMRM in Canada (Montreal).

Based on the phenomenon of lack of Lac response during the second part of stimulation, illustrated in Chapter 6, further studies were carried out to see how variations of the duration of the initial stimulation period effects the brain Lac response under the second long-term visual stimulation in the visual cortex (Chapter 7).

Since ^{1}H-MRS only allows observation of pool size of the metabolites, further measurements of the metabolic cycling rate using ^{13}C MRS with infusion of ^{13}C labelling in the visual cortex during neuronal activity are planned. Chapter 8 outlines how *in vivo* ^{13}C MRS studies can be carried out in the human brain after infusion of the ^{13}C-labelling substrates. Four stages have been introduced in detail, including the choice of ^{13}C-labelled substrate, ^{13}C NMR spectral detection, ^{13}C labelling time course analysis, choice of metabolic modelling compartment and mathematical expression of the compartmental model. This is then followed by results from the initial experiments for parameter optimization, mainly related to the flip angle optimization, decoupling optimization and TR optimization, which were carried out during the first year of PhD study. Some future work is also proposed.

Finally, the main conclusions drawn from the experiments described in this thesis are presented in Chapter 9.

Chapter 2

Nuclear magnetic resonance (NMR)

2.1 Introduction

Nuclear Magnetic Resonance (NMR) is a phenomenon which occurs when the nuclei of certain atoms are placed in a static magnetic field and exposed to a second oscillating magnetic field. Some nuclei experience this phenomenon and others do not, this depends on whether they possess a property called spin. Spin can be thought of as a small magnetic field and will cause the nucleus to produce an NMR signal. NMR is a very detailed method of chemical analysis for organic compounds. It can tell us the number of hydrogen atoms in a molecule and their related positions in the carbon chain. The theory of NMR has been well established. This chapter focuses on the basic principles involved in magnetic resonance that are relevant to the work presented in this thesis.

2.2 The physical basis of NMR

2.2.1 What is spin?

NMR relies on the magnetic properties of atomic nuclei. Spin is a fundamental property, like electrical charge or mass, and is quantized in multiples of 1/2. A nucleus containing an odd number of protons, neutrons or both has a nuclear spin. Individual unpaired electrons, protons and neutrons each possesses a spin of 1/2 and have intrinsic spin angular momentum, J. The spinning nucleus, like an electric current, generates a tiny magnetic field. When placed in a magnetic field of strength B, spinning protons acting like bar magnets, can line up with or against the field, like a compass needle in the earth's magnetic field (see Fig. 2.1). There is a low energy state where the poles are aligned N-S-N-S and a high energy state N-N-S-S.

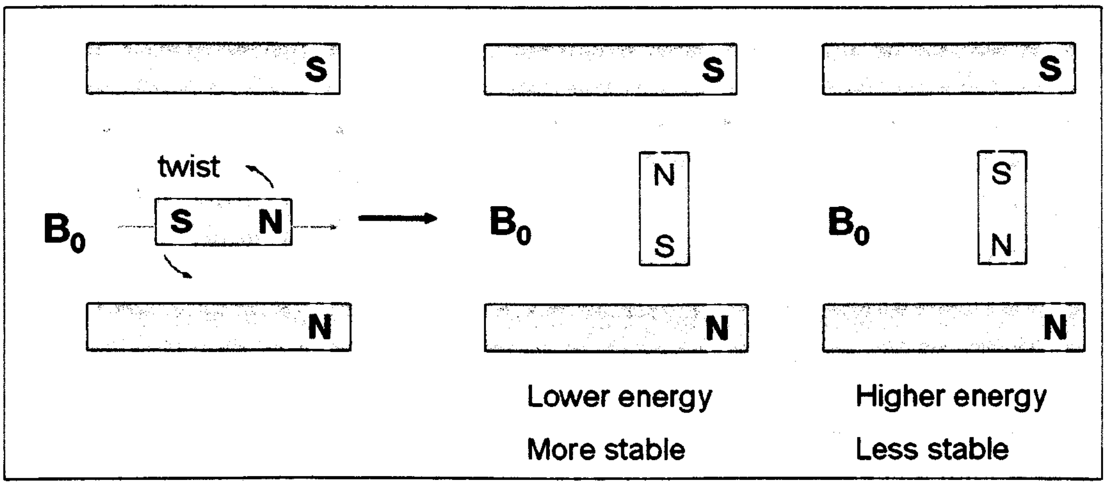

Figure 2.1: Spinning protons acting like bar magnets, can line up with the field or line up against it.

As the nuclei are charged, they also possess a magnetic moment μ given by:

$$\mu = \gamma J \tag{2.1}$$

Table 2.1: Properties of more commonly observed nuclei in NMR. Note: the relative sensitivity depends on the third power of γ, the ratio of γ_C/γ_H=1/4, leading to a sensitivity of 1/64. By setting the relative sensitivity of ^1H to be 100, the relativity sensitivity of ^{13}C is approximately 1.6.

Nucleus	Spin	Natural abundance	$\gamma/2\pi$ (MHz/T)	Relative sensitivity $(\gamma^3/(\gamma_H)^3)$	Frequency at 3T (MHz)	Frequency at 7T (MHz)	Chemical shift range (ppm
^{1}H	1/2	99.98 %	42.57	100	127.7	298.0	10
^{13}C	1/2	1.1 %	10.71	1.6	32.1	74.95	200
^{19}F	1/2	100 %	40.07	83	120.2	280.5	150
^{31}P	1/2	100 %	17.25	6.6	51.8	120.8	50

where γ is the gyromagnetic ratio, which has the value of 42.58MHz/T for the proton. μ is parallel to and proportional to the spin angular momentum vector, J. Table. 2.1 shows the relative abundance and gyromagnetic ratios of some important nuclei.

2.2.2 Procession in a magnetic field (classical description)

If a bar magnet is placed in a magnetic field, it experiences a turning force or torque, trying to align it with the applied field. Similarly a nuclear magnetic moment (μ) in a magnetic field experiences a torque. However, because it is spinning and has angular momentum, the resultant movement is not simply an aligning rotation but a circular motion called precession (like a gyroscope, see Fig. 2.2).

For electricity and magnetism, the torque (T) on a magnetic dipole (μ) in a mag-

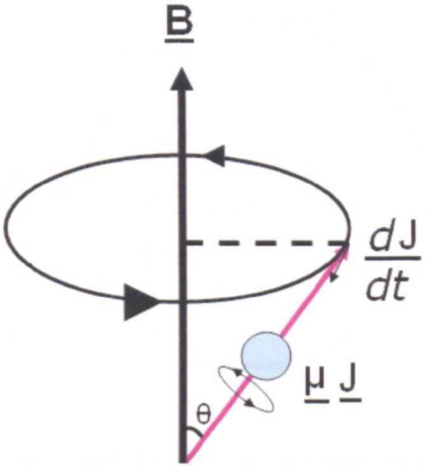

Figure 2.2: Gyroscope effect

netic field (B) is

$$T = \mu \times \mathbf{B} = \mu \ Bsin\theta \tag{2.2}$$

and from mechanics $T = \frac{dJ}{dt}$, where J is the angular momentum. Therefore:

$$\frac{dJ}{dt} = \mu \times \mathbf{B} = \mu \ Bsin\theta \tag{2.3}$$

and $\frac{dJ}{dt}$ must be perpendicular to both μ and B, and J (as μ is parallel to J). Therefore, J changes in a direction that is perpendicular to J, which means that it must precess. This is the gyroscope effect.

The angular frequency of precession?

From Fig 2.3, the arc length is equal to the radius multiplied by the angle subtended

$$\frac{dJ}{dt}\delta t = Jsin\theta\delta\phi \tag{2.4}$$

Combining Equations (2.3) and (2.4) gives

$$\frac{\delta\phi}{\delta t} = \frac{\frac{dJ}{dt}}{Jsin\theta} = \frac{\mu \ Bsin\theta}{Jsin\theta} = \frac{\gamma JBsin\theta}{Jsin\theta} = \gamma B \tag{2.5}$$

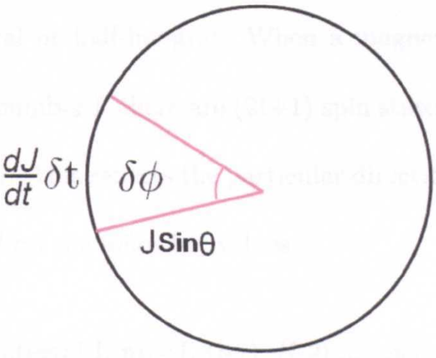

Figure 2.3: View from the above of Fig 2.2. In a time δt the projection of J, perpendicular to B, sweeps out an angle $\delta\phi$.

Defining the frequency of precession to be $\omega = \frac{\delta\phi}{\delta t}$ gives

$$\omega = \gamma B \tag{2.6}$$

This is the **Larmor equation**, and the frequency of precession, ω, is known as the Larmor frequency, ω_L.

2.2.3 Energy quantization (quantum mechanical description)

The classical view of magnetic resonance is insufficient to explain all aspects of the NMR phenomenon as the nucleus is just treated as a macroscopic object like a billiard ball. We must also consider the quantum mechanics of the nucleus in a magnetic field. From the view of quantum mechanics, spin angular momentum, J, is a vector quantity and its amplitude is given by:

$$J = (\frac{h}{2\pi})\sqrt{I(I+1)} \tag{2.7}$$

where h is *Planck*'s constant(h=6.626x10^{-34} J s) and I is the spin quantum number, which can only be integral or half-integral. When a magnetic field is applied, for a particular spin quantum number I, there are (2I+1) spin states related to the magnetic spin quantum number, m_I. This reflects the particular direction of angular momentum, which can be taken based on the following values:

For integral I: m_I=I, (I-1), (I-2),......,0,......,-I

For half integral I: m_I=I, (I-1), (I-2),......,1/2, -1/2,......,-I

The component of angular momentum in the z direction is defined by:

$$J_z = (\frac{h}{2\pi})m_I \tag{2.8}$$

Therefore, for a proton for which $I = \frac{1}{2}$, there are two quantum states: $m_I = +\frac{1}{2}$, $m_I = -\frac{1}{2}$, with the spin axis pointing "up" or "down", as shown in Fig. 2.4.

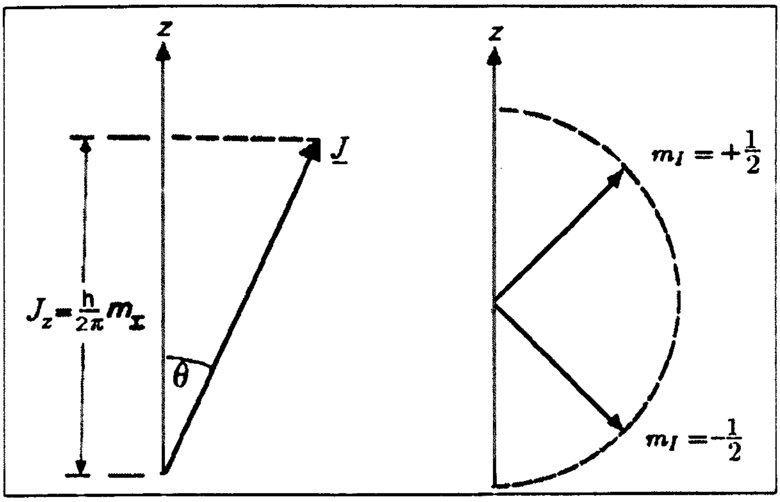

Figure 2.4: The z-component of spin angular momentum for I=1/2

Since the angular momentum is quantized, the magnetic moment will also be quantized. Therefore the magnetic moment along the longitudinal z axis is given by:

$$\mu_z = \gamma J_z = \gamma(\frac{h}{2\pi})m_I \tag{2.9}$$

In an external magnetic field B_0, a magnetic moment in the z direction acquires a magnetic energy defined as:

$$E = -\mu_z B_0 = -\gamma J_z B_0 = -\gamma(\frac{h}{2\pi})m_I B_0 \tag{2.10}$$

Because it is a quantum phenomenon, for a proton with $I = \frac{1}{2}$, there are only two energy levels and no possible states in between. Therefore for protons in a magnetic field there are two Zeeman energy levels (see Fig. 2.5, negative symbol indicates the lowest energy when μ is parallel to B):

$$E_{1/2} = -\gamma(\frac{h}{4\pi})B_0 \tag{2.11}$$

$$E_{-1/2} = \gamma(\frac{h}{4\pi})B_0 \tag{2.12}$$

The nuclei can undergo a transition between the two energy states by the absorption of a photon. A particle in the lower energy state absorbs a photon and ends up in the upper energy state. This transition is fundamental to all forms of spectroscopy. The energy of this photon must exactly match the energy difference between the two states[35]. This occurs provided that:

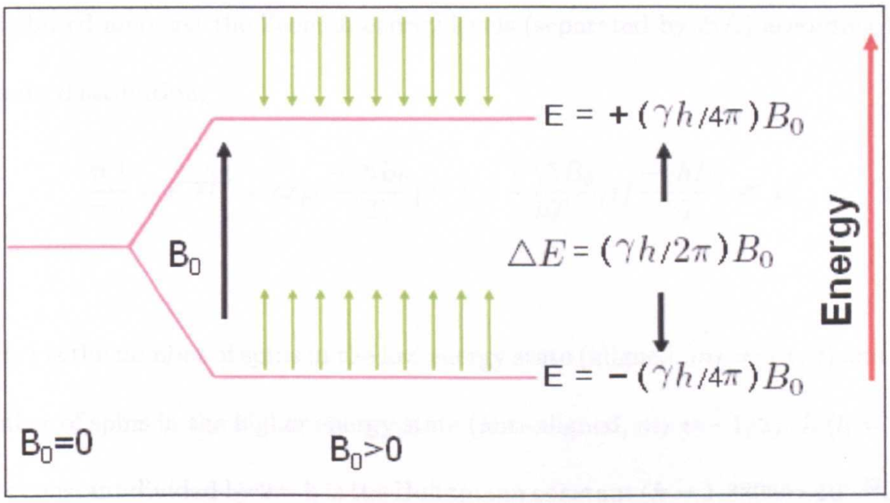

Figure 2.5: Energy levels for I=1/2.

$$\Delta E = \gamma(\frac{h}{2\pi})B_0 \tag{2.13}$$

As can be seen from Equation 2.13, the energy separation between the two quantum states is proportional to the strength of the external magnetic field, and increases as the field strength is increased. A large energy separation results in a more sensitive NMR experiment and better separation of the resonance frequencies of nuclei in different chemical environments. Therefore, much effort and expense has been put into designing and building bigger and stronger superconducting magnets for NMR.

2.2.4 Macroscopic magnetization

NMR only considers bulk magnetization (the sum of the magnetization of the individual spins). For a spin $\frac{1}{2}$ nucleus in thermal equilibrium with its surroundings, the spins are distributed amongst the Zeeman energy levels (separated by ΔE) according to the Boltzmann distribution:

$$\frac{n\downarrow}{n\uparrow} = e^{\frac{-\Delta E}{kT}} = exp[\frac{-\gamma\hbar B_0}{kT}] \sim 1 - \frac{-\gamma\hbar B_0}{kT}, if \frac{-\gamma\hbar B_0}{kT} \ll 1 \qquad (2.14)$$

Where $n\uparrow$ is the number of spins in the low energy state (aligned, $m_I = +1/2$) and $n\downarrow$ is the number of spins in the higher energy state (anti-aligned, $m_I = -1/2$). $\hbar$ ($\hbar = \frac{h}{2\pi}$) is Planck's constant divided by 2π, k is the Boltzmann constant ($k = 1.38066 \times 10^{-23} Jk^{-1}$) and T is the temperature in Kelvin. As there are only two states, the total number of spins N is given by:

$$N = n\uparrow + n\downarrow \qquad (2.15)$$

Since the Zeeman energy is small compared to the average energy available at room temperature (kT) i.e $kT \gg \Delta E$, and both $n\uparrow$ and $n\downarrow$ are very close to half the total number of spins in the sample, the net population difference can be approximated to:

$$n\uparrow - n\downarrow = N[\frac{1-exp(\frac{\gamma\hbar B_0}{KT})}{1+exp(\frac{\gamma\hbar B_0}{KT})}] \simeq \frac{N\gamma\hbar B_0}{2kT} \tag{2.16}$$

It is the population difference ($n\uparrow$ - $n\downarrow$) that gives rise to a net bulk magnetisation within the material which is the only thing we can observe by NMR. This population difference is one of the fundamental factors determining the basic NMR signal. Because $kT \gg \triangle E$, the population difference is very low. Therefore NMR has inherently low sensitivity. It can be seen from Equation 2.16 that the bulk magnetization is proportional to the magnitude of the applied static field (B_0) and to the total number of spins in the sample and inversely proportional to the temperature. Thus, sensitivity can be improved by decreasing the temperature of the system or increasing the magnetic field.

2.2.5 Sensitivity of the NMR experiment

NMR has inherently low sensitivity due to its small population difference at thermal equilibrium. Another important aspect is the relative sensitivity of different nuclei with different gyromagnetic ratios (γ). There are three ways in which γ affects the sensitivity of the NMR signal. (1). The population difference at thermal equilibrium is proportional to the γB_0 (see Equation 2.16). (2). The nuclear magnet precession induces a NMR signal in the receiving coil. The amplitude of the NMR signal is proportional to the strength of the nuclear magnet, which is related to the gyromagnetic ratio (γ). (3). According to the equation 2.6, the rate of the nuclear precession is also proportional to γB_0. As for any electrical generator, higher voltage can be generated if the crank runs faster. From these considerations, we can say that the amplitude of the NMR signal (sensitivity) for a spin -1/2 nucleus is proportional to:

$$[N \times \gamma B_0/T] \times \gamma \times [\gamma B_0] = N(\gamma)^3(B_0)^2/T \tag{2.17}$$

This equation tells us that the sensitivity of NMR depends on the number of spins in the sample (N), the third power of γ and the square of B_0, as well as being inversely proportional to the absolute temperature (T). So, it is worth trying to build up stronger and more powerful magnets and to try to develop new techniques to cool down the coil without freezing the sample (noise decreases with decreased T).

2.3 Excitation and detection in NMR

2.3.1 RF pulse in NMR

In order to observe nuclear magnetization, the precessional motion needs to be detected. However, at thermal equilibrium, the spins have no phase coherence in the transverse plane and the net longitudinal magnetization (in the Z axis) is a static vector. Nuclear magnetization can only be observed by rotating the net longitudinal magnetization towards the transverse plane (xy-plane), which is perpendicular to B_0. This can be accomplished using a second magnetic field in the transverse plane, oscillating in the RF (MHz) range: the radio frequency (RF) pulse. They are the primary tools used to perform the desired spin manipulations like excitation, inversion and refocusing.

An ideal RF pulse is a short ($\sim 10 \mu s$), and very high power (50-300 W) pulse of radio frequency power applied to the probe coil, with a specific frequency, amplitude, and phase. It has a rectangular envelope: the power switches on and instantly reaches full power, then goes instantly to zero at the end of its duration. The pulse creates an oscillating magnetic field (B_1), which rotates in the xy-plane at the frequency of the pulse.

To probe the nuclear magnetisation, RF magnetic fields of appropriate energy (frequency) are applied to excite transitions between the Zeeman energy levels. The photon frequency required can be calculated as follows:

$$\Delta E = \frac{h}{2\pi}\gamma B_0 = h\nu \tag{2.18}$$

so

$$\nu = \frac{\gamma}{2\pi}B_0 \tag{2.19}$$

RF magnetic fields are conventionally referred to as B_1 fields to distinguish them from the static, B_0, field. B_1 is not static but is oscillating at frequency w_1, which must be at or very close to the Larmor frequency w_L. The duration of the pulse is called the pulse width, which is usually measured in microseconds. The phase of the pulse is determined by its starting point in the sine function. A special coil (antenna) is used to produce the RF field and this coil is tuned to the required resonant frequency.

The rotating frame

It is usual to think of RF pulses in the rotating frame. The lab frame is defined to have coordinates (x, y, z). In the lab frame the B_1 field is rotating (at Larmor frequency w_L) in the xy-plane.

Imagine standing on a record player that is rotating clockwise at the frequency of the RF pulse w_L. If you are rotating with the record, the record appears stationary. We define a new rotating frame of reference on the record (x', y', z'). In this frame the B_1 field is stationary. The lab frame and rotating frame are related by:

$$z' = z$$

x' rotating at frequency w_L with respect to x.

y' rotating at frequency w_L with respect to y.

To transform the spins into the rotating frame, a fictitious field of amplitude $w_L\ /\gamma$ must be applied (to cancel their rotation). If w_1, the frequency of the pulse, is close to the Larmor frequency of the spins (w_L), then the result of this is that B_L transforms to (approximately) zero in the rotating frame (this makes sense as spins are not precessing about z' in that frame).

The Effect of an RF pulse on the net magnetization

Previously we considered the precession of a single spin. The net magnetization, M_0, will also precess about the field that is not collinear with it. In the rotating frame, the only field acting is the w_1 component of the RF field (usually called B_1), since the static field B_0 has transformed to zero in the rotating frame. The magnetization will now precess around B_1, and so the bulk magnetization rotates in $y'z'$ plane.

The duration (τ) and strength (B_1) of the RF pulse determines the flip angle (α) of the RF pulse (that is the angle through which the bulk magnetization M_0 is rotated by the pulse), such that:

$$\alpha = \gamma B_1 \tau \tag{2.20}$$

A 180^o pulse flips the magnetization from z to -z and it is said that the magnetization is inverted. We will see that this pulse can also refocus magnetization. A 90^o pulse flips the magnetization to the xy-plane and it is said that the magnetization is excited. Following a 90^o pulse M_z=0 and M_{xy}=M_0. More generally, a α^o pulse acting on equilibrium magnetisation will reduce M_z from M_0 to $M_0 cos(\alpha)$, and increase M_{xy} to $M_0 sin(\alpha)$.

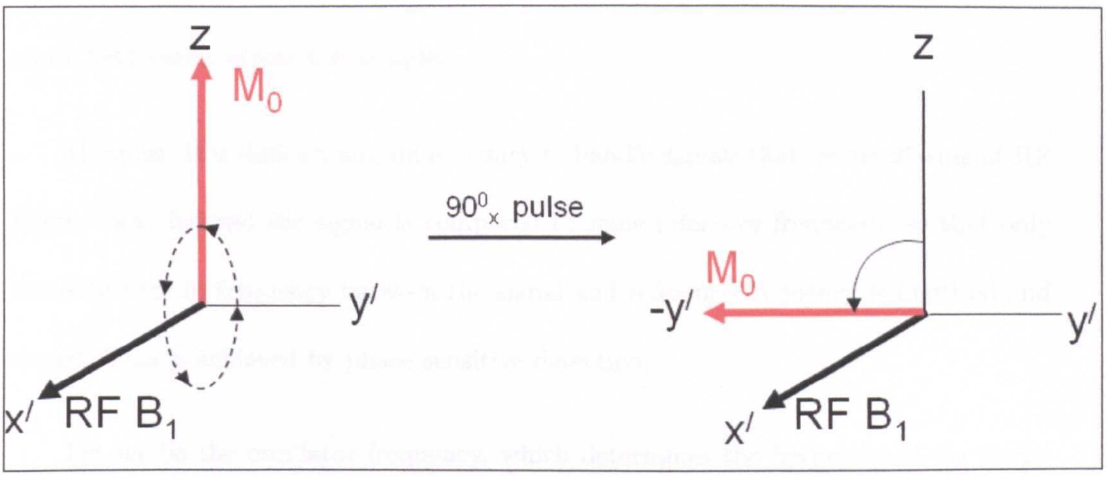

Figure 2.6: Magnetisation tipped by an 90^0 RF pulse in the rotating frame. The RF pulse magnetic field (B_1 along the x' axis) exerts a torque on the net magnetization vector (M_0 in the Z direction) and rotates it in a plane perpendicular to the B_1 field vector (in a counter clockwise direction from the +z axis toward the $-y'$ axis in the rotating frame).

2.3.2 Signal detection

As described above, after a 90^o pulse the bulk magnetisation, M_0, has been tipped into the xy-plane (all the spins are in phase with no net population difference between the up and down states). Once the RF pulse is switched off, the xy-magnetization created by the pulse, will now precess about the main field B_0 at the Larmor frequency.

Phase sensitive detection (PSD)

It is important to know the exact frequency of the received signal as this is used to encode images, as well as to perform spectroscopy in analytical NMR. We have assumed above that the spins are all precessing at the same Larmor frequency (w_L), but in practice there will be a variation in frequency across the sample, as the local static field varies across the sample.

However, it is difficult and unnecessary to handle signals that are oscillating at RF frequencies. Instead the signal is compared to some reference frequency, so that only the difference in frequency between the signal and reference frequency is digitised and stored. This is achieved by phase sensitive detection.

Let w_1 be the oscillator frequency, which determines the frequency of the transmitter and receiver, and which is in general set to be approximately equal to the mean Larmor frequency of the sample (w_L). In practice the Larmor frequency varies across the whole sample, as the local static field varies across the sample.

The signal from the scanner (V_s) at frequency w_L is compared to a reference signal (V_r), which is oscillating at the same frequency as the transmitter w_1.

$$V_s = V_{so} cos \omega_L t \tag{2.21}$$

$$V_r = V_{ro} cos \omega_1 t \tag{2.22}$$

These signals are multiplied together so that the detected signal (V_d) is given by

$$V_d = V_{so} V_{ro} cos \omega_L t cos \omega_1 t = \frac{1}{2} V_{so} V_{ro} (cos(w_L - w_1)t + cos(w_L + w_1)t) \tag{2.23}$$

2.4 Interactions between nuclei

The equations of motion for a system of spins were classically derived assuming there are no interactions between nuclei. However, interactions between nuclei have very important effects in NMR, which will be described in detail in the following section.

2.4.1 the Bloch equations

In general an RF pulse reduces M_z; it also causes the spins to come into phase with each other and hence creates a transverse component of the magnetisation M_{xy}. Following a pulse, the longitudinal and transverse components of the magnetisation will return to their equilibrium states as shown in Fig. 2.7. Longitudinal recovery to equilibrium position $M_z = M_0$, depends on exchange of spin energy with lattice and is determined by the longitudinal (spin-lattice) time constant T_1. Transverse decay depends on relative dephasing of spins (loss of phase coherence) and is determined by the transverse (spin-spin) time constant T_2.

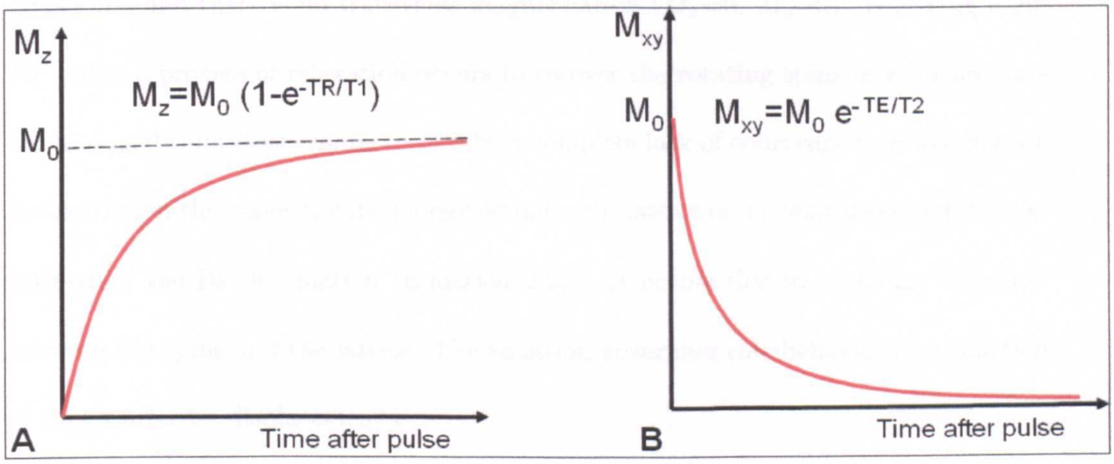

Figure 2.7: A: Longitudinal recovery described by the T_1 (spin-lattice) relaxation time. B: Transverse decay described by the T_2 (spin-spin) relaxation time.

If at time, t, the magnetisation has components M_x, M_y and M_z, then the rate of change of the magnetisation can be described by the **Bloch equations**. These are empirical equations, that is to say they were written down as the result of experimental observations, not derived:

$$\frac{dM_z}{dt} = -\frac{(M_z - M_0)}{T_1} \tag{2.24}$$

$$\frac{dM_x}{dt} = \frac{-M_x}{T_2} + \gamma M_y B_0 \tag{2.25}$$

$$\frac{dM_y}{dt} = \frac{-M_y}{T_2} - \gamma M_x B_0 \tag{2.26}$$

Solutions to these equations give rise to the graphs and equations in Fig. 2.7 for the appropriate boundary conditions (M_{xy}(t=0)=M_0; M_z(t=0)=0).

2.4.2 T_1 processes

At equilibrium, the net magnetization vector lies along the z direction (the applied magnetic field B_0) and is called the equilibrium magnetization M_0. In this configuration, the z component of magnetization M_z (referred to as the longitudinal magnetization) equals M_0 and there is no transverse magnetization (M_x=0, M_y=0). Following a 90^0 RF pulse, a process of relaxation occurs to recover the rotating spins in xy-plane back to the equilibrium state, characterized by a complete lack of coherence (random phase). Relaxation in the z-axis is called longitudinal, spin-lattice or T_1 relaxation and it is described by the Bloch equation (Equation 2.25). It occurs due to exchange of energy between the spins and the lattice. The equation governing this behavior as a function of time t after its displacement is :

$$M_z = M_0(1 - e^{-t/T_1}) \tag{2.27}$$

T_1 is specific for different kinds of matter and depends on the magnetic field strength: the higher the magnetic field the longer the T_1. If the net magnetization is placed along the -z axis after a 180^0 pulse (the magnetisation is completely inverted which means that $M_z(0) = -M_0$), the equation governing this behavior as a function of the time t after its displacement is:

$$M_z = M_0(1 - 2e^{-t/T_1}) \tag{2.28}$$

2.4.3 Measurement of T_1: an inversion recovery sequence

If a 180^0 RF pulse is applied it will invert the longitudinal magnetisation to $M_z(0) = -M_0$. The longitudinal magnetisation (M_z) will then recover towards its equilibrium distribution with a time constant T_1. However, the z magnetization can not be directly observed. Therefore, the recovery period should be followed by a 90^0 RF pulse which converts the z magnetization into observable xy-magnetization (Fig. 2.8). The magnitude of the FID (Free Induction Decay) signal arising from this xy-magnetization (and the peak height in the spectrum) should be directly proportional to the longitudinal magnetization just before the 90^0 RF pulse (existing at time TI, known as the inversion time). We can use the Bloch equations to calculate how this M_z signal depends on both T_1 and TI (see Equation 2.29).

The boundary conditions are that initially at TI=0, the equilibrium magnetisation is completely inverted and the longitudinal magnetisation, M_z is equal to $-M_0$. At a certain time later the longitudinal magnetisation has recovered to zero, and this inversion time is called the null point. After that it continues to recover beyond back to its equilibrium value where M_z is equal to M_0. In general, at a time TI after the inversion pulse, the longitudinal magnetisation has recovered to an arbitrary value M_z(t=TI). This signal measured at a range of values of TI, M_z(t=TI) can be fitted to this expression to measure T_1. (Often describe this as NMR signal S, where S=$S_0(1 - 2e^{\frac{-TI}{T_1}})$.

A simple way to estimate T_1 without making a plot is to look for a null or near-null condition for a given peak. That is: S=$S_0(1 - 2e^{\frac{-TI}{T_1}})$=0, which occures when $T_1 = TI/ln(2)$. Knowledge of T_1 relaxation is required for the signal acquisition and the design of optimal timings for data acquisition (see Chapter 8.2.4).

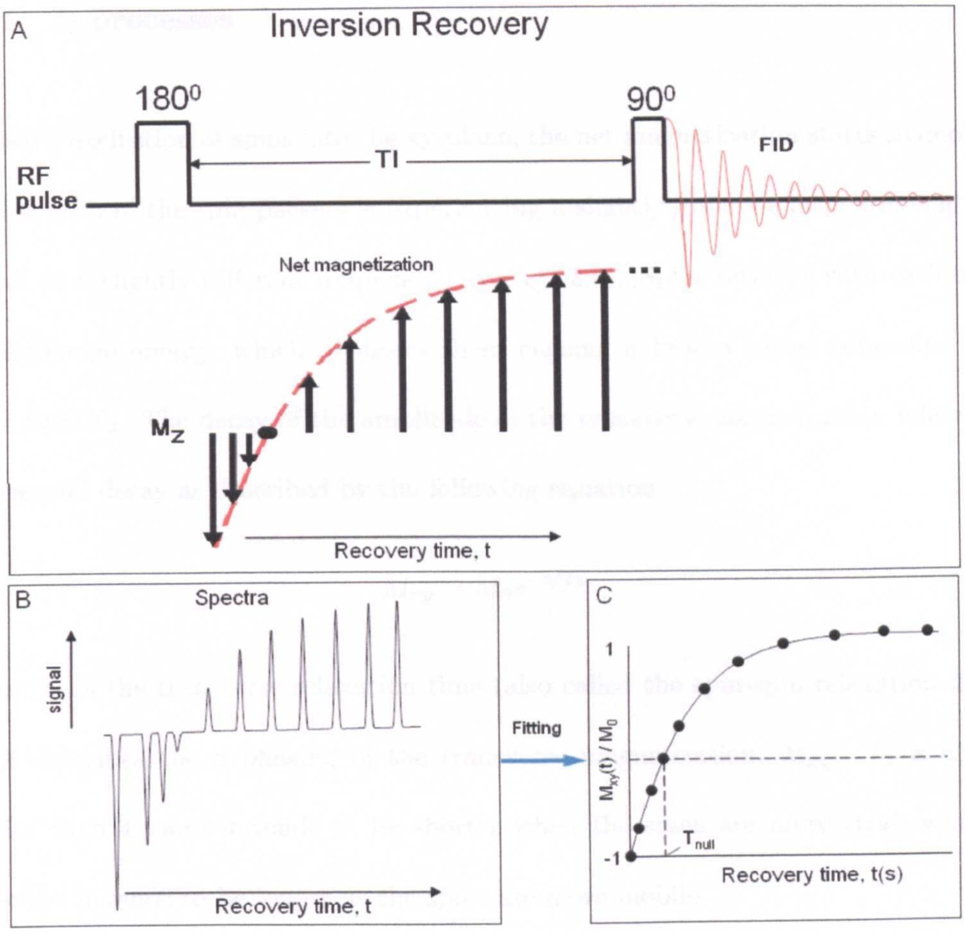

Figure 2.8: Inversion recovery (IR) experiment for measuring T_1 (A). The initial amplitude of the FID (signal amplitude) in an inversion recovery experiment will depend on the magnitude of M_z prior to the 90^0 pulse, which in turn depends on the inversion time TI. At a certain time known as T_{null} (the "null time") the longitudinal magnetisation is actually zero. For TI=0, we should see an upside-down spectrum, with each peak at its maximum height but inverted (B). As the delay is increased each peak will become less intense, pass through zero and finally become positive. T_1 relaxation constants can be obtained by fitting the spectra in B with Equation 2.29 (C), giving an estimate of the T_1 relaxation time. The time of zero-crossing of the longitudinal magnetization, t_{null}, is given by $T_1 ln(2)$.

2.4.4 T_2 processes

Following excitation of spins into the xy-plane, the net magnetization starts to dephase because each of the spin packets is experiencing a slightly different magnetic field and rotates at a slightly different frequency (see Fig. 2.9). Spins interact with each other and exchange energy, which dephases them causing a loss of phase coherence with decay time T_2. The decay of the amplitude of the transverse magnetisation follows an exponential decay as described by the following equation.

$$M_{xy} = M_0 e^{-t/T_2} \tag{2.29}$$

Where T_2 is the transverse relaxation time (also called the spin-spin relaxation time), which describes the dephasing of the transverse magnetization, M_{xy}. T_2 is always smaller than T_1 and it tends to be shorter when the spins are more rigid, while in molecules it tends to be longer as the spins are more mobile.

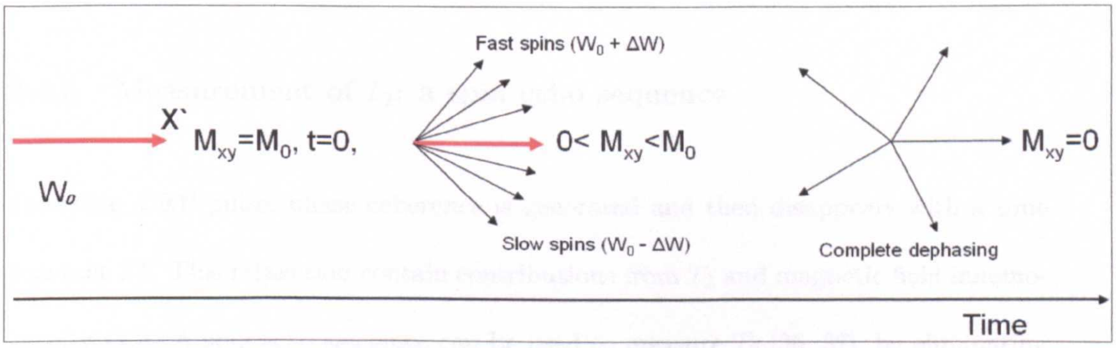

Figure 2.9: In the rotating frame, a spin processing at ω_0 is stationary. Spins in high fields precess faster than w_0 with frequency $\omega_0 + \Delta\omega$. Spins in lower fields precess slower than w_0 with frequency $\omega_0 - \Delta\omega$. These spins interact with each other and exchange energy, causing a loss of the transverse magnetization ($M_{xy} = 0$).

In real systems, the NMR signal decays faster than by spin-spin interaction alone.

Two factors contribute to the decay of transverse magnetization. Molecular interactions lead to a pure T_2 molecular relaxation effect. In addition, variations in B_0 lead to an inhomogeneous T_2 effect, which can be described by the constant T_2'. The combination of these two factors results in the decay of transverse magnetization, with time constant, T_2^*. The relationship between the T_2 from molecular processes and that from inhomogeneities in the magnetic field is as follows.

$$\frac{1}{T_2^*} = \frac{1}{T_2} + \frac{1}{T_2'} \tag{2.30}$$

NOTE: T_2' processes are generally static in time, so it is possible to rephase them. Natural T_2 processes vary with time, and hence cannot be rephased.

Since neighbouring nuclei experience slightly altered magnetic fields, the precessional frequency of these spins will also be altered. The spread of resonant frequencies $\triangle\omega_L$ leads to intra-voxel dephasing.

2.4.5 Measurement of T_2: a spin echo sequence

Following a 90° pulse, phase coherence is generated and then disappears with a time constant T_2^*. This relaxation contain contributions from T_2 and magnetic field inhomogeneity (T_2'). A spin echo sequence can be used to measure T_2 [36, 37], by eliminating the contribution from T_2'.

Following a 90° pulse, the spins are rotated to M_y, where they precess coherent transverse magnetisation, $M_{xy} = M_0$, then decays with T_2^* due to static (T_2') and varying (T_2) processes. If a 180° pulse is applied after a time TE/2, where TE is the echo time (the time between the 90° pulse and the top of the spin-echo), then M_{xy} is reversed. For static (T_2') processes, spins that were precessing faster than average, are still doing so, and so they will then catch up with the bulk magnetisation after a time

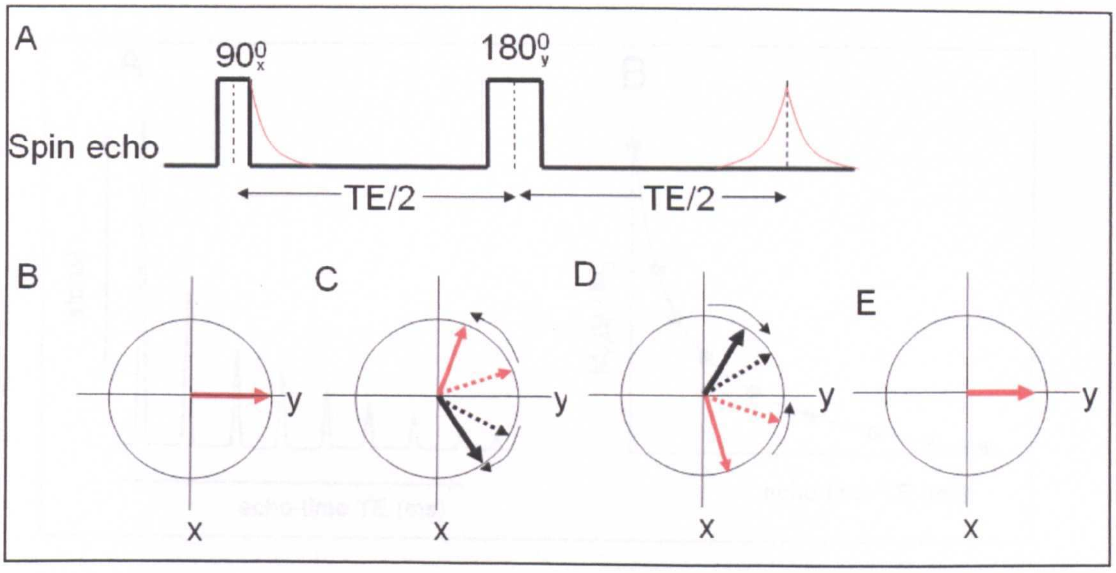

Figure 2.10: Spin-echo formation. A: spins are excited and transverse magnetization (phase coherence) is generated along the y-plane after 90^o RF pulse. B: the magnetization starts to lose coherence during the subsequent delay (the first half of echo time), due to the B_0 magnetic field inhomogeneity and frequency offset. C: A 180^o refocusing pulse inverts all the magnetization vectors along the y axis at the time of TE/2. D: The spins rephase during the second half of the echo time due to the same magnetic field inhomogeneity and frequency offset. Comparing the transverse magnetization between B and E, the transverse magnetization has decayed due to T_2 relaxation.

TE (similarly spins precessing slower than average will be caught up with). For varying T_2 processes, the fields are constantly varying, so the spins will not rephase exactly, as the field experienced will have changed in each time interval. The refocused signal (echo amplitude) will therefore be attenuated by T_2 processes. If data are collected at varying echo times (TE values) then the signal versus TE decay curve can be fitted to an exponential curve, according to:

$$M_{xy} = M_0 e^{\frac{-TE}{T_2}} \tag{2.31}$$

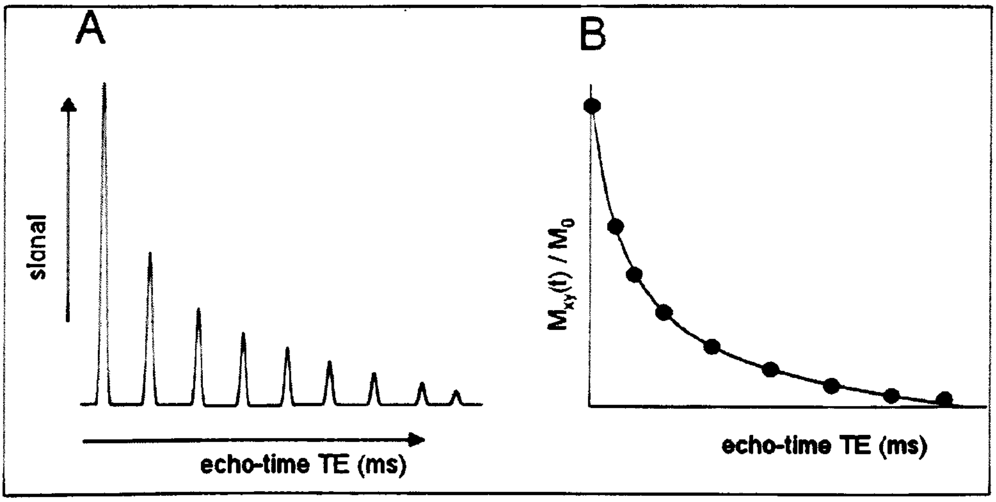

Figure 2.11: Measurement of T_2 relaxation time through the use of the spin-echo method. A: Spectra obtained with different TE values. B: T_2 relaxation constant can be obtained by fitting the data presenting in A into the equation 2.32.

2.5 Free induction decay (FID)

The FID is the basic form of the signal detected in NMR. The signal oscillates at the Larmor frequency, w_L and will decrease as a function of time, due to T_2 relaxation. However, macroscopic and microscopic inhomogeneity in the main magnetic field B_0 will create a distribution of local different B_0 magnetic fields across sample, leading to a distribution of Larmor frequencies. This distribution can lead to a more rapid loss of transverse magnetization, which decays with a decay time T_2^*, as shown in Fig. 2.12. The signal decays to nothing over a period of approximately $5T_2^*$.

2.6 the Fourier transform

Following a RF pulse which is calibrated to rotate M_0 by 90^o, the net magnetization is placed in the transverse plane of the rotating frame of reference. The magnetization

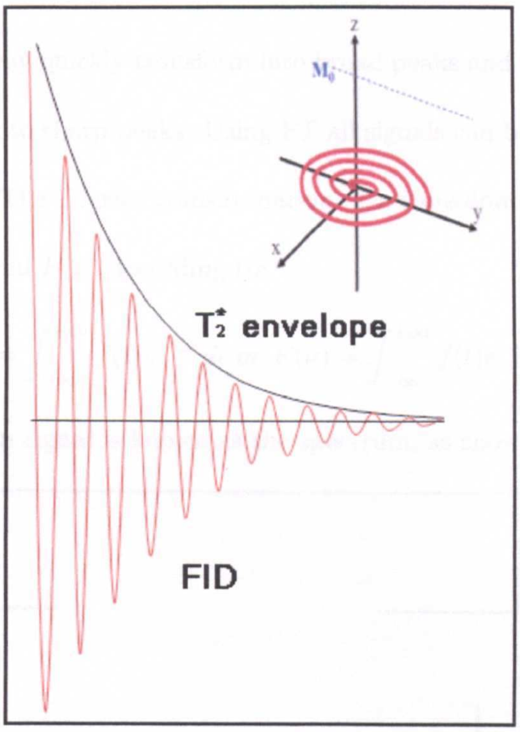

Figure 2.12: Free Induction Decay (FID). Signal is oscillating at the Larmor frequency and has a signal decay whose envelope has a T_2^* decay.

precesses about B_0 at the Larmor frequency and induces a signal in a receiving coil positioned in the transverse plane.

The raw data or FID is a series of intensity values collected as a function of time, which exhibits a single decaying sine wave (from a single proton signal) or a complex sum of a number of decaying sine waves (from many different types of protons with different chemical shifts) with different frequencies and amplitudes in time. The time-dependence of the signal intensity (FID) holds all the relevant information about the nuclear spins, like their resonance frequencies and relative abundance. However, they are seldom used directly. Normally the FID is converted into the frequency-domain data by mathematical calculation called the Fourier transformation (FT), which essentially looks at the sine wave and analyses it to determine the frequency. This frequency appears as a peak in the spectrum, which is a plot in the frequency domain of the same data. Signals that decay quickly transform into broad peaks and the signals that last a long time transform into sharp peaks. Using FT all signals can be separated according to their frequencies. The Fourier transformation of a time-domain signal f(t) gives a frequency-domain signal $F(\omega)$ according to:

$$F(\omega) = \int_{-\infty}^{+\infty} f(t)e^{-i\omega t}dt \; or \; F(\nu) = \int_{-\infty}^{+\infty} f(t)e^{-i2\pi\nu t}dt \tag{2.32}$$

This frequency domain signal is known as the spectrum, as shown in Fig. 2.13.

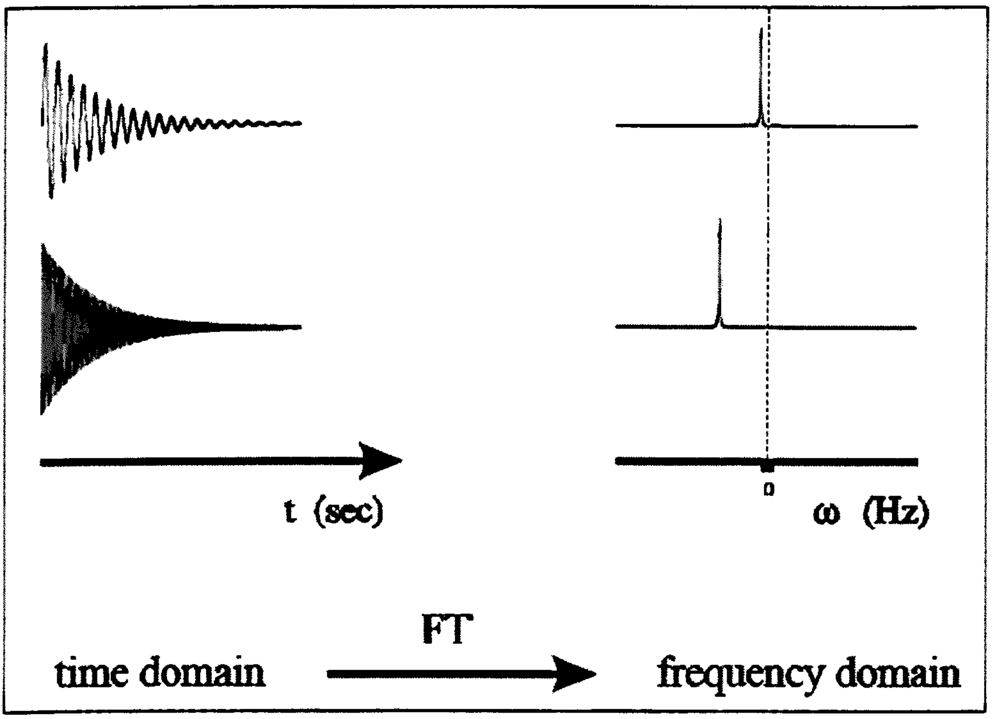

Figure 2.13: Time domain data can be converted into Frequency domain data by Fourier Transformation(FT).

2.7 Phase cycling

A multiple-pulse NMR experiment is designed to manipulate the spins in certain carefully defined way so as to produce a particular spectrum. However, a given pulse sequence usually affects the spins in several different ways, and as a result the final spectrum may contain coherences other than those intended when the experiment was designed. The presence of such coherences may result in extra crowding in the spectrum, they may obscure the wanted peaks and may also lead to ambiguities of interpretation.

In the development of multiple-pulse NMR, phase cycling has been the principle method to keep the signal we want and cancel certain signals which is mostly the spectral artifacts created by non-ideal conditions in the NMR electronics. The most likely cause of the artifacts is that the two receiver channels, real and imaginary, have unequal gain or amplification. Phase cycling eliminates these artifacts by changing the phase of the RF pulse in a fixed pattern (e.g., 0^0, 90^0, 180^0, and 270^0 in scans 1, 2, 3 and 4) and changing the phase of the receiver. The number of scans should be an integer multiple of the phase cycle length to assume optimal cancelation of artifacts. The computer combines the real and imaginary spectra from each channel for each step of the sequence to generate the final phase cycled spectrum. In this process the desired signals add, but the artifacts (undesired signals) cancel, due to their different phase relations. However, the phase cycle cancellation probably makes matters worse if the first scan or two are acquired with the nuclei not at steady state. It is therefore important to establish a steady state using dummy (or steady-state) scans, which include a relaxation delay, pulse, and acquisition time just like normal scan, but the data are not stored.

Chapter 3

Magnetic resonance spectroscopy (MRS)

Magnetic Resonance Spectroscopy (MRS) works on the same basic principles as NMR, to study physical, chemical, and biological properties of matter. As can be seen from the Larmor equation, the difference between two energy levels of an NMR-active nucleus is directly proportional to the applied magnet field strength. Due to different environments and therefore different shielding from the static magnetic field, the nuclei "feel" slightly different fields. Hence, all differently bound atoms of one species show slightly varying energy level differences which is very important for NMR spectroscopy.

3.1 Chemical shift

The resonance frequency is not only a characteristic of the type of nucleus but also varies slightly depending on the position of that atom within a molecule (the "chemical environment"). This occurs because the bonding electrons create their own small magnetic fields, which subtract from, or add to the external fields, therefore modifying the external magnetic field in the vicinity of the nucleus.

$$B_{eff} = B_0(1 - \sigma) \tag{3.1}$$

Where σ is the "shielding constant" . This is the basis of the **NMR spectrum**. Nuclei in different functional groups are distinguished on the basis of their different electronic environment. This subtle variation, on the order of one part in a million (ppm), is called the chemical shift (normally designed by the Greek letter delta, δ) and provides detailed information about the structure of the molecules. δ (ppm) is normally measured from some arbitrarily chosen reference:

$$\delta = \frac{(f - f_{ref}) \times 10^6}{f_{ref}} \tag{3.2}$$

where f is the observed frequency and f_{ref} is the reference frequency. The reference compound should be chemically inert and its chemical shift should be independent of external variables such as temperature or ionic strength. It should also have a strong singlet resonance peak separated from the others. Tetramethylsilane (TMS) is usually used as reference compound for ^1H and ^{13}C NMR. However, TMS is not present in *in vivo* systems, therefore it cannot be used as an internal reference. For *in vivo* ^{31}P NMR, the normal choice of reference (for which δ is set to 0) is PCr, whereas for *in vivo* brain ^{1}H MRS, N-acetyl aspartate (NAA) at 2.01ppm is the choice of reference.

A graph of the resonant frequencies over a very narrow range of frequencies centred on the fundamental resonant frequency of the nucleus of interest is called a spectrum (see Fig. 3.1), and each peak in the spectrum represents a unique chemical environment within the molecule being studied. For example, Lac has six peaks due to its two unique carbon positions in the molecule: the doublet proton spectrum resonance at 1.33ppm comes from the CH_3 group, split by the protons of the CH group; the quartet spectrum downfield at 4.10ppm comes from the CH group, split by the three protons of the CH_3 group. The splitting comes from J-coupling, which will be described in detail in the following section.

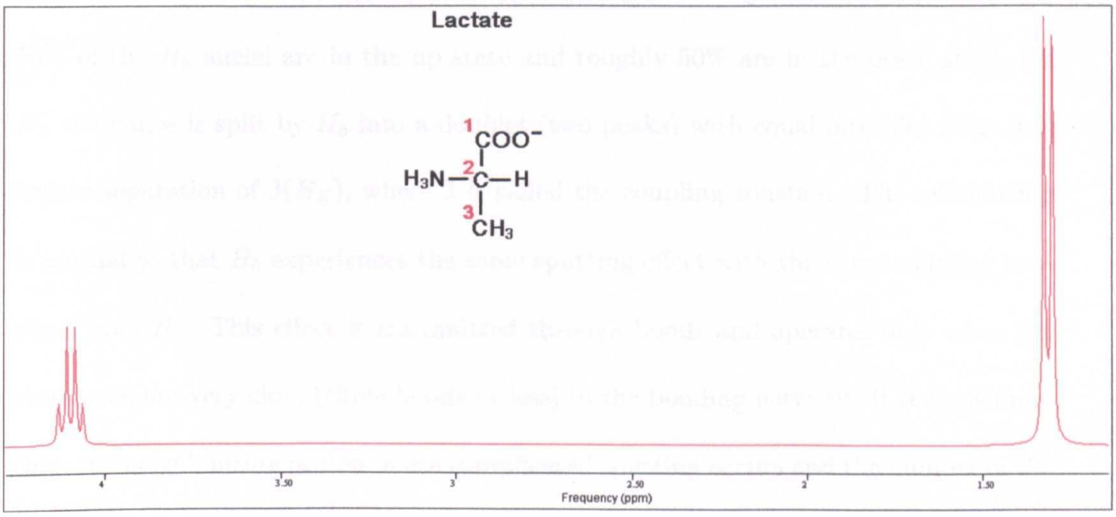

Figure 3.1: Spectral patterns for Lactate at 7T simulated by NMR Scope in jMRUI using the experimentally measured NMR parameters from reference [38].

3.2 Scalar spin-spin coupling

Peaks are often split into multiple peaks due to interactions between nonequivalent protons on adjacent carbons, called spin-spin coupling, which is another valuable piece of information about molecular structure. Nonequivalent protons on adjacent carbons have magnetic fields that may align with or oppose the external field. This magnetic coupling causes the proton to absorb slightly downfield when the external field is reinforced and slightly upfield when the external field is opposed. All possibilities exist, so the signal is split. Consider two protons ($H_aC - CH_b$) with different chemical shifts on two adjacent carbon atoms within a molecule. The magnetic nucleus of H_b can be either aligned with ("up") or against ("down") the magnetic field of the spectrometer (Fig. 3.2 and Fig. 3.3). Since the resonant frequency is always proportional to the magnetic field experienced by the nucleus, this changes the frequency of H_a so that it now resonates at one of two frequencies which are very close together. As approximately 50% of the H_b nuclei are in the up state and roughly 50% are in the down state, the H_a resonance is split by H_b into a doublet (two peaks) with equal intensity (Fig. 3.3) with a separation of J(H_Z), where J is called the coupling constant. The relationship is mutual so that H_b experiences the same splitting effect with the same coupling constant from H_a. This effect is transmitted through bonds and operates only when the two nuclei are very close (three bonds or less) in the bonding network. If there is more than one neighbouring proton, more complicated splitting occurs and the number of the peaks is equal to one more than the number of neighbouring protons giving rise to the splitting. For example, if there are two neighbouring protons ($H_aC - C(H_b)_2$), there are four possible ways for two H_b protons to align with or against the magnetic field of the spectrometer: both "up", both "down", the first "up" and the second "down", the first "down" and the second "up". If both H_b spins are "up", the H_a resonance is shifted to the right of ν_a by JH_z. If both are "down", the H_a resonance is shifted to the left of ν_a by JH_z. If one is "up" and one is "down", the effects cancel each other and the H_a proton absorbs at its normal chemical shift position (ν_a). Because there are two ways in can happen, the central peak resonance at ν_a is twice as intense as the outer resonances, giving a "triplet" pattern with intensity ratio 1:2:1 (Fig. 3.4). Similar arguments apply for larger numbers of neighboring spins which split the H_a resonance peak into one more peak than the number of H's on the adjacent carbon ("n+1 rule")(Fig. 3.5).

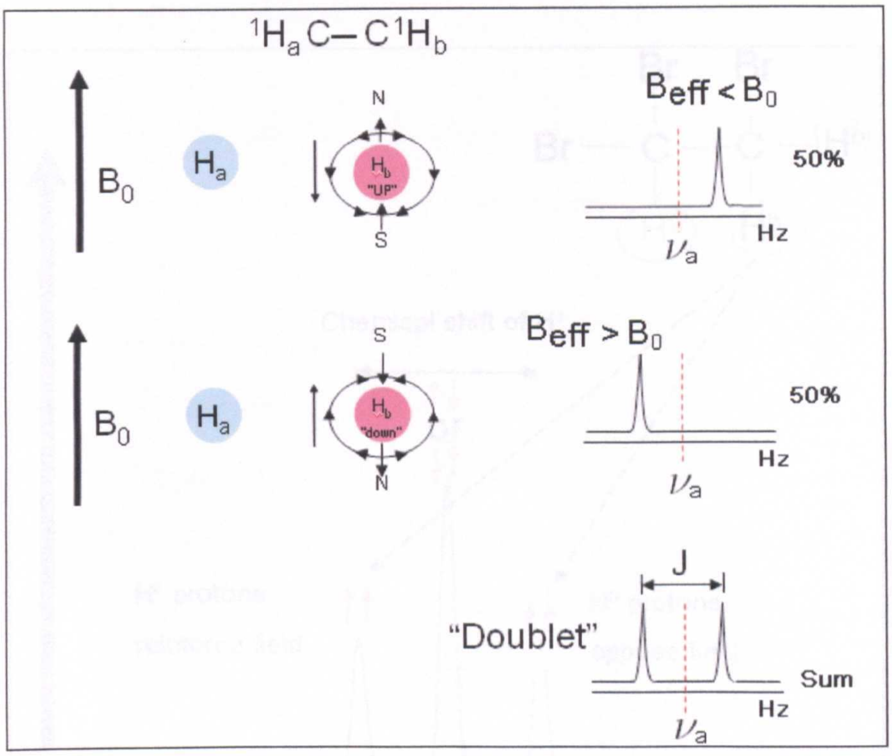

Figure 3.2: Spin-spin coupling

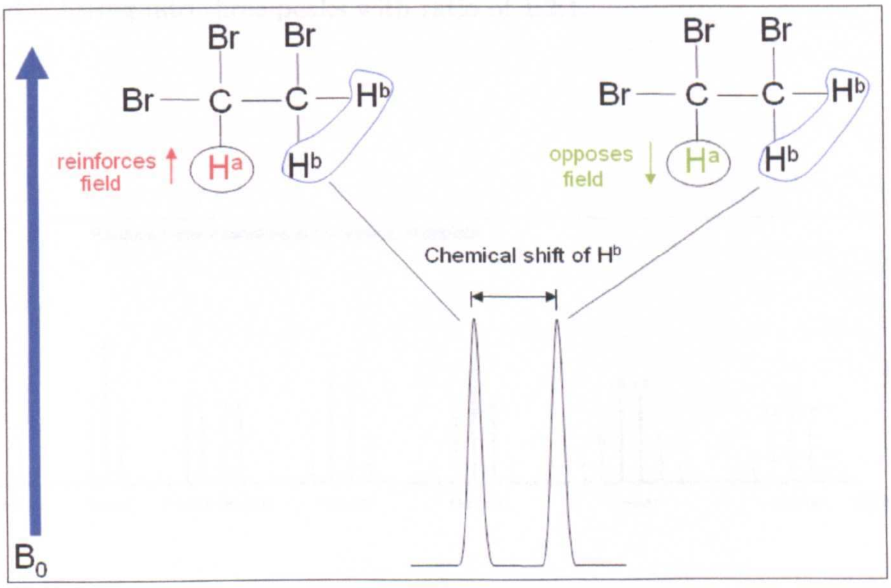

Figure 3.3: Spectral structure showing example of proton (H^b) coupled to one proton(H^a) and splitting into two peaks with ratio of 1:1.

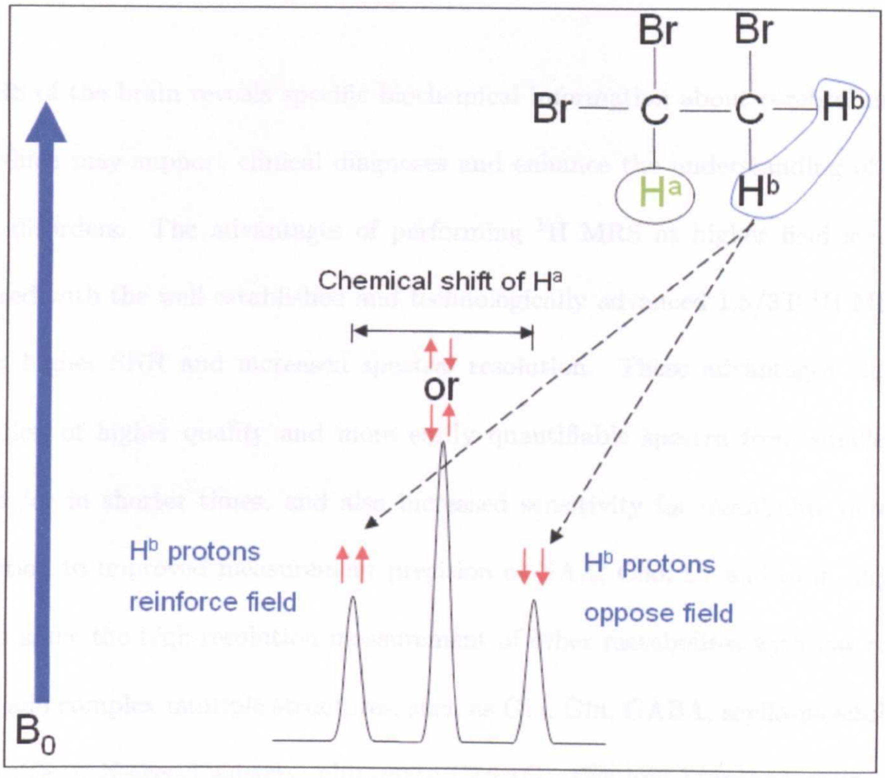

Figure 3.4: Spectral structure showing example of proton(H^a) coupled to two protons (H^b) and splitting into three peaks with ratio of 1:2:1.

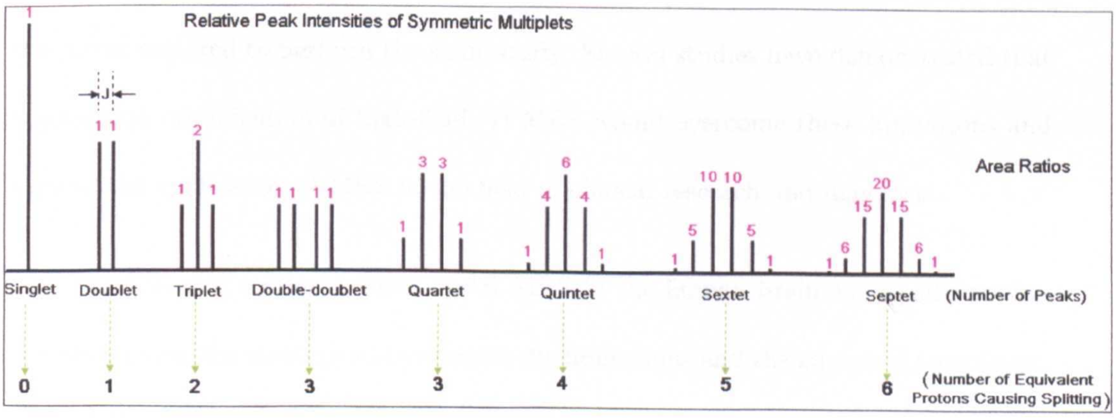

Figure 3.5: The N+1 Rule

3.3 Improved spectral quality at high field strength (7T)

^{1}H MRS of the brain reveals specific biochemical information about cerebral metabolites, which may support clinical diagnoses and enhance the understanding of neurological disorders. The advantages of performing ^{1}H MRS at higher field strengths, compared with the well-established and technologically advanced 1.5/3T-^{1}H MRS, include a higher SNR and increased spectral resolution. These advantages allow the acquisition of higher quality and more easily quantifiable spectra from smaller voxels and /or in shorter times, and also increased sensitivity for metabolite detection. In addition to improved measurement precision of NAA, Cho, Cr and mIn, high-field systems allow the high-resolution measurement of other metabolites with low concentration and complex multiple structures, such as Glu, Gln, GABA, scyllo-inositol, Asp, taurine (Tau), N-acetyl aspartyl glutamate (NAAG), Glc and branched amino acids, thus extending the range of metabolic information. However, these advantages may be hampered by intrinsic field-dependent technical issues, such as shorter T_2 relaxation times, higher acoustic noise, increased chemical shift artifact errors, increased magnetic susceptibility, larger eddy current effects, as well as more challenges in designing appropriate radiofrequency coils, increased magnetic field instability and increases in the power required to perform the same study. Several studies have demonstrated that appropriate optimization of high-field ^{1}H MRS would overcome these limitations and expand the application of MRS in the field of clinical research and diagnosis.

The following section focuses on ^{1}H MRS in the human brain at 7T, illustrating the advantages, the strategies to overcome the limitations and the advanced techniques.

3.3.1 Signal-to-noise ratio

The intensity of the MR signal is correlated linearly with square of the strength of the magnetic field (B_0^2), but noise goes with B_0. Thus, in theory, the signal-to-noise ratio ($SNR \propto \frac{S}{N} \propto \frac{B_0^2}{B_0} \propto B_0$) would be increased by $\frac{7}{3}$ =2.33 when switching from a 3T system to a 7T system. In practice the improvement has been shown to range from 20% to 46%[39, 40]. In a realistic MRS experiment, the SNR depends on several other variables, such as T_1 and T_2 relaxation times, types of sequence, number of signal averages, size of sample volume, radiofrequency effects, shimming efficacy and water suppression performance [41]. At high field, T_1 relaxation times increase, leading to increased signal saturation for a given repetition time, while T_2 relaxation times decrease. Therefore, the theoretical doubling of SNR cannot be achieved, due to the use of repetition times (TR) $< \infty$ and echo times (TE) > 0 [39]. One possible approach to increase the SNR is the use of multiple receive coils (which could also be used at lower field). The SNR increases with the number of coil elements, mainly for the regions next to the coil array and to a lesser extent for those towards the centre of the imaged object[42].

3.3.2 Spectral resolution

Spectral resolution refers to the ability to distinguish adjacent peaks. Despite shorter T_2 relaxation times and increased local and global susceptibility broadening, the increase in frequency scales at 7T yields improved spectral resolution, compared with 1.5T and 3T. This improves quantification of J-coupled metabolites, such as Glu, Gln and GABA, as well as others signals of scyllo-inositol, Asp, Tau, NAAG, Glc and branched amino acids. Clinical 1.5T scanners equipped with ^{1}H MRS packages allow the quantification of NAA, Cho, Cr and Lac at long echo-time, and further metabolites, such as myo-

Ins and *Glu* + *Gln* at short echo time. Glu and Gln present strong coupling and extensive spectral overlap at 1.5T, making their measurement difficult and prone to large uncertainties. They are readily measured as total Glx (Glu+Gln). In addition, the measurement of GABA at 1.88, 2.28, and 3.01ppm is difficult due to its relatively low concentrations in the human brain and the overlap with signals from other molecules including macromolecules, Cr, Glu and Gln [43]. Higher field MR scanners increase the separation between peaks, as well as increasing SNR, allowing a more accurate identification and quantification of each metabolite (see Fig. 3.6 and Fig. 3.7)[39, 40, 44, 45, 1].

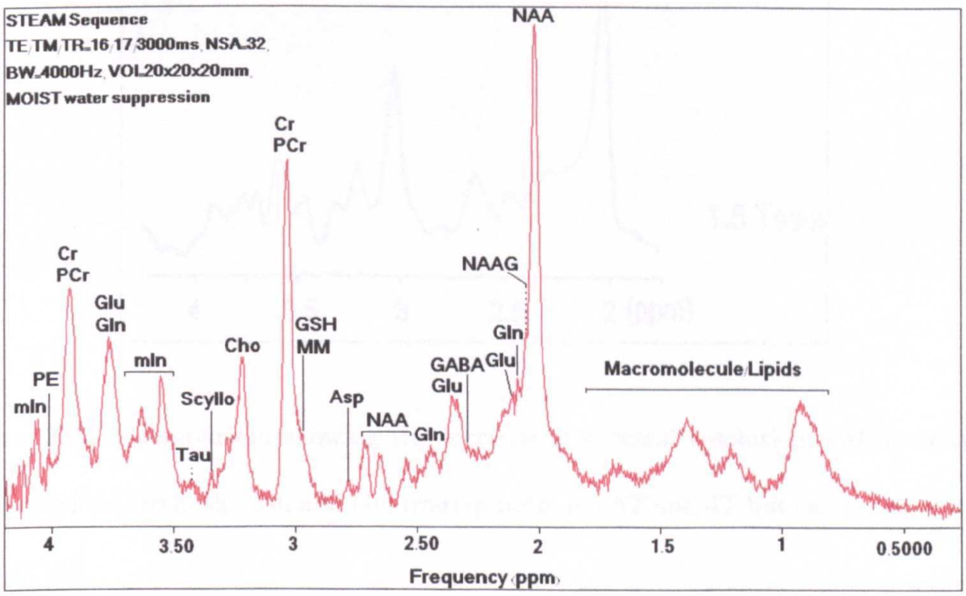

Figure 3.6: A representative raw 7T proton spectrum acquired using a short TE STEAM sequence in human brain on visual cortex. Acquisition parameters are as follows: TE/TM/TR=16/18/3000ms, NSA=32, BW=4000Hz, VOI=20x20x20mm, acquisition time=1.6 mins.

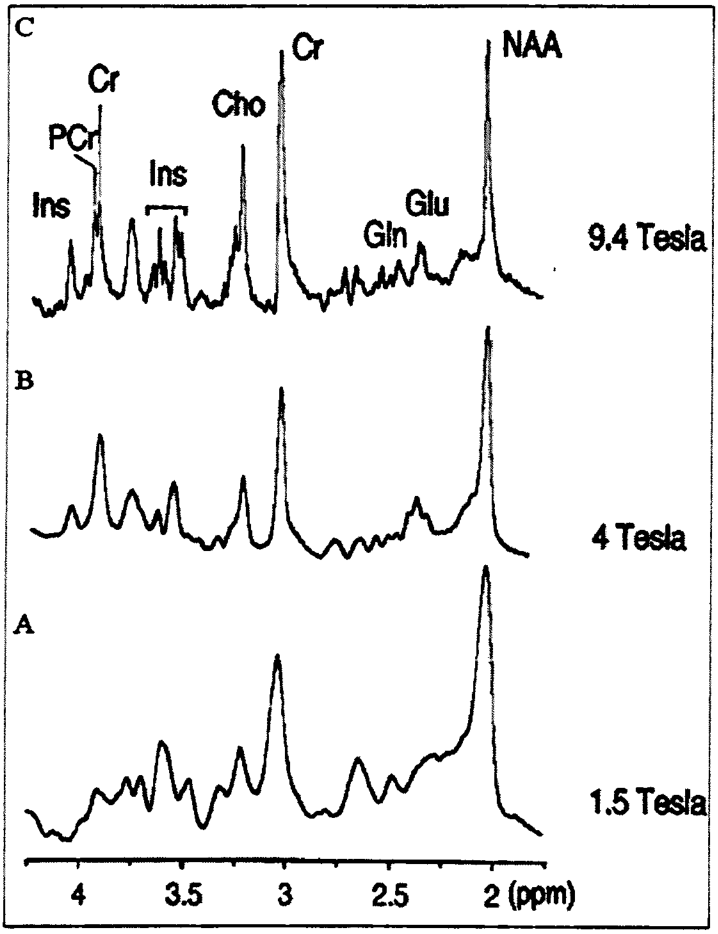

Figure 3.7: A comparison showing the increase in spectral resolution with increased magnetic field strength. Glu and Gln overlap both at 1.5T and 4T but can be separated at 9.4T[44].

3.3.3 Spatial resolution

Increased spatial resolution at high field strength allows the separation between different anatomical structures, between normal and pathological tissues, or between different pathological structures. It is commonly accepted that the SNR per unit time of ^{1}H MRS is linearly proportional to the voxel volume and reducing the MRS voxel substantially lowers the SNR. However, at 3T and higher, voxels below 1 cm^3 can be obtained with still good SNR and acceptable acquisition times [46, 47]. Furthermore, decreasing voxel size, will increase the magnetic homogeneity and T_2^*, therefore resulting in a strong decrease of linewidths for metabolites allowing improved quantification. Higher spatial resolution also improves the matching of metabolic and anatomical information, eliminating partial volume effects and enhancing the clinical value of ^{1}H MRS[48]. It is possible to acquire spectra from a single-voxel or from 2D and 3D multivoxels, which is generally referred to as Chemical Shift Imaging (SCI) or MRS imaging (MRSI) (see Fig3.8), thus enabling the evaluation of metabolite concentration differences between grey and white matter based on imaging segmentation[49, 50].

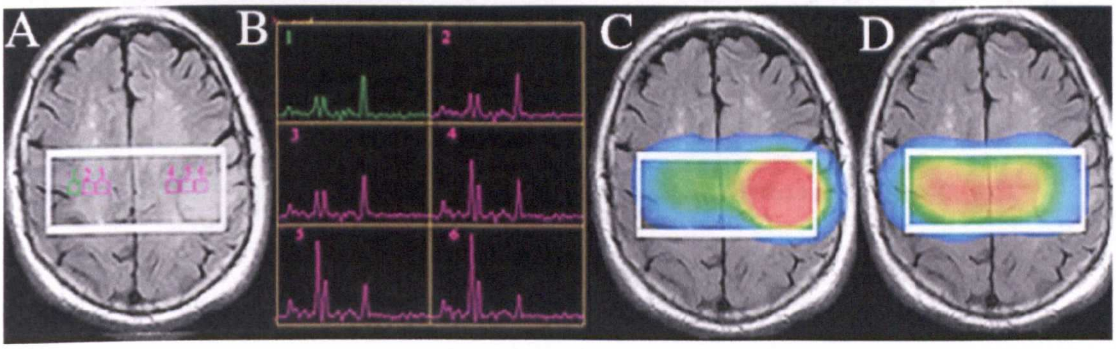

Figure 3.8: Example of 2D multivoxel SI at 3T using PRESS (TR 2000/TE 144ms)[51]. (A) Axial FLAIR images from a 71-year-old male showing a high grade glioma in the left parietal region and the volume of interest. (B) Spectra from the corresponding boxes in A. Choline (C) and N-acetylaspartate (D) maps showing elevated choline and decreased N-acetylaspartate in the tumor area. The color scale depicts the strongest metabolite signal with red and the weakest with dark blue.

3.3.4 Temporal resolution

Higher field strength (higher than 3T) considerably reduces the acquisition time for a given SNR. Benefiting from the increased SNR at high field strengths, a decreased number of acquisitions (NSA) can yield the same SNR as obtained at 1.5T, when using 3T or higher magnetic fields, bringing about the shorter acquisition times. The advantages of shorter examinations for patients, radiologists, technicians are obvious[46].

3.4 *In vivo* ^1H magnetic resonance spectroscopy

^{1}H nuclei are highly sensitive in NMR due to the high natural abundance and high gyromagnetic ratio. Since nearly all metabolites contain protons, *in vivo* ^{1}H NMR spectroscopy has developed into a useful tool for observing, identifying and quantifying a large number of biologically important compounds in tissue.

3.4.1 Commonly detectable ^{1}H metabolites in human brain

Localization methods with TEs of 135-270 ms have been applied to detect information about metabolites such as NAA, Cr, Cho, Lac by ^1H-MRS at lower field strength[52, 53]. With decreasing TE and increasing spectral resolution and signal at high field strength, the ability to resolve J-coupled spin systems, such as Glu, Gln, mIn and Glc has been substantially increased. Short echo time localization methods minimize T_2 relaxation effects, which increases the sensitivity and reliability of metabolite quantification, especially for the strongly coupled spin systems, such as Glu, Gln. Metabolites commonly identified in the human brain are as follows:

N-Acetyl Aspartate (NAA)

NAA is exclusively localized in the central and peripheral nervous systems. In ^{1}H NMR spectra of normal brain tissue, the NAA resonance at 2.01ppm is the most prominent peak and has been used as a marker of neuronal density. This is supported by the observation of a decrease in NAA intensity in disorders which are accompanied with neuronal loss, such as chronic stages of stroke[54] , tumors[55] and multiple sclerosis[56].

NAA has also been used as an internal reference since its concentration is relatively immune to acute metabolic disturbances such as ischemia or hypoxia. However, care is required when using NAA as an internal reference since NAA concentration is not uniform over the entire brain, with higher concentrations in gray matter (8-11mM) as compared with white matter (6-9mM)[57, 58]. Furthermore, NAA signal overlaps with Glu, N-acetly containing metabolites, such as NAAG, and macromolecules, at shorter echo times[59].

Creatine (Cr) and Phosphocreatine (PCr)

In ^{1}H NMR spectra of normal tissue, the singlet resonances at 3.03ppm and 3.93ppm arise from the methyl and methylene protons of Cr and PCr, respectively. Together they are often refered to as "total creatine" (tCr). In the brain, Cr and PCr are present in both neuronal and glial cells. As a mechanism for the storage and transmission of phosphate-bound energy, Cr/PCr play essential roles in the energy metabolism of the brain[60]. Cr/PCr can undergo phosphorylation-dephosphorylation reactions catalyzed by the enzyme creatine kinase:$ADP + PCr \leftrightarrow ATP + Cr$. If oxidative phosphorylation cannot be maintained to supply ATP, PCr can provide the phosphate group to ADP to form ATP and reduce the extent of non-oxidative glucose consumption, which can reduce neuronal death due to a delayed decrease of ATP under hypoxic stress, and protect the normal brain function against the accumulation of Lac. Total Cr at 3.03ppm is frequently used as a reference of concentration in ^1H spectroscopy since the concentration is thought to be relatively constant both in normal and diseased brains.

Choline-containing Compounds(tCho)

Besides resonances from NAA and total creatine, the most prominent resonance in ^{1}H NMR spectra from brain arises from the methyl protons of choline-containing compounds at 3.2ppm. Since the resonance contains contributions from free choline, glycerophosphorylcholine (GPC) and phosphorylcholine (PC), it is often refered to as "total choline" (tCho). Choline-containing compounds are involved in pathways of phospholipid synthesis and degradation, thereby reflecting membrane turnover. Increased choline signal is observed in cancer[61], Alzheimer's disease[62] and multiple sclerosis[63], while decreased choline levels are associated with liver disease and stroke[64].

Glutamate (Glu) and Gamma-amino butyric acid (GABA)

Glu and GABA are the major excitatory and inhibitory neurotransmitters in the cortex, together accounting for ~90% of synapses. Glu and GABA are mainly localized in specialized neurons, referred to as glutamatergic and GABAergic neurons, respectively. Glutamatergic and GABAergic neurons rely on Gln from astrocytes to maintain neurotransmitter homeostasis. It is well established that the amino acid Glu serves a multitude of roles in the mammalian brain. Glu is a component of energy metabolism and the principal excitatory neurotransmitter, accounting for 80 ~ 90% of the synapses in the brain[65]. It is also the immediate precursor for synthesis of GABA in neurons and Gln in astrocytes [66]. Furthermore, Glu has many other fates in the brain, including oxidation for energy, incorporation into proteins, and formation of GSH [67]. Glu is present in all cell types with the largest pool in glutamatergic neurons and smaller pools in GABAergic neurons and astrocytes. Glu has a complex NMR spectrum with a signal spread out over many low intensity resonances. Signal from the single ^{2}CH methine proton (see Fig .3.9) appears as a doublet-of-doublets at 3.75ppm, while the resonances from the other four protons appear as multiplets between 2.04ppm and 2.35ppm. Glu and Gln are virtually indistinguishable at lower magnetic fields (See Fig. 3.7 (A and B)), whereas the Glu-$^4CH_2$ and Gln-$^4CH_2$ protons become separate resonances at magnetic field strengths of 7T (see Fig. 3.6) and higher (see Fig. 3.7(C)). Abnormal levels of Glu and GABA have been linked to a wide range of neurodegenerative diseases, such

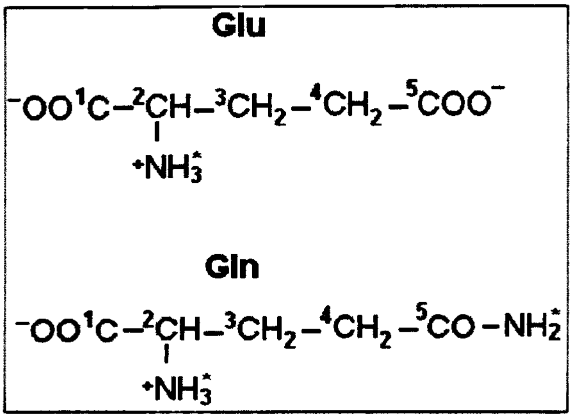

$$^{-}OO^{1}C-{}^{2}\underset{{}^{+}NH_3^{*}}{\underset{|}{C}}H-{}^{3}CH_2-{}^{4}CH_2-{}^{5}COO^{-}$$

$$^{-}OO^{1}C-{}^{2}\underset{{}^{+}NH_3^{*}}{\underset{|}{C}}H-{}^{3}CH_2-{}^{4}CH_2-{}^{5}CO-NH_2^{*}$$

Figure 3.9: Chemical structure for Glu and Gln.

as multiple sclerosis (MS)[68], Amyotrophic Lateral Sclerosis (ALS)[69], Schizophrenia or Depression[70]. 1.5T ^{1}H-MRS has been used as a noninvasive tool to assess the role of Glu in the human brain. However, at short TE, Glu is virtually indistinguishable from Gln and they can only be measured together as total Glx (Glu+Gln). GABA concentrations are relatively low in the human brain and the proton signals of GABA at 1.88, 2.28, and 3.01ppm underlie signals from other molecules of higher concentration, so it is difficult to measure GABA at 1.5T and 3T. Studies at higher magnetic fields (7T) enables better resolution of Glu and GABA, leading to a greatly enhanced quantification accuracy.

Glutamine (Gln)

Gln is an important component of intermediary metabolism and is primarily located in astrocytes at a concentration of 2-4mM[71]. Gln is synthesized from Glu by Gln synthethase in the astrocytes and converted back to Glu by glutaminase in neurons. Besides its role in the Glu-Gln neurotransmitter cycle, a main function of Gln is in ammonia detoxification [72]. Gln is structurally similar to Glu and as a result its chemical shifts and scalar coupling interactions are also similar. The ^{2}CH methine proton resonates as a triplet at 3.76ppm, while the multiplets of the four methylene protons are closely grouped between 2.12ppm and 2.46ppm. In order to understand the role of Gln in intermediary metabolism, the separate detection of Gln from Glu is essential.

Glutathione (GSH)

GSH is a tripeptide of the glutamate (GSH-Glu), glycine (GSH-Gly) and Cysteine residues (GSH-Cys). GSH is a powerful antioxidant found inside different kinds of cells, including those of the central nervous system, due to its unique capacity as a reducing agent[73]. In addition to performing its well-established free radical scavenger role in human brain, GSH is also involved in the processes underlying memory[74]. A decrease in GSH concentration has been associated with degenerative diseases of aging and the pathogenesis of several diseases, including Amyotrophic Lateral Sclerosis[75], Alzheimer‘s[76] and Parkinson‘s disease[77]. GSH exists primarily in its reduced form (GSH). The oxidized form (GSSG) presents a smaller fraction (1%) and can not be detected by *in vivo* MR methods.

Unfortunately the ^1H spectrum is crowded, due to the small chemical shift range (around 10 ppm) and its specificity suffers from the complex peak pattern due to J-coupling. Another difficulty encountered in ^1H-spectroscopy is the necessity to eliminate the large water and the lipid signals that obscure the metabolites presenting at millimolar or sub-millimolar concentrations. I am going to discuss these in the following Section.

3.5 Signal localization

3.5.1 Surface coil

Surface coils can be designed in various sizes and shapes to suit different objects or regions of interest. They are mainly used on superficial areas of the body over which the coil is placed. Surface coils have a good SNR for tissues adjacent to the coil, but are poor for the deeper tissue, due to the signal decrease with distance. One of the main problems associated with the use of a surface coil is the inhomogeneous B_1 field they generate. Variations in the spin rotation due to inhomogeneities in B_1 can lead to a decrease in signal and incorrect quantification of metabolite concentrations. Furthermore, localization by surface coil alone is generally inadequate for deep-lying organs due to contaminating signals from intervening surface tissues.

3.5.2 Single voxel localization

It is possible to apply a sequence of pulses such that only spins in a localised volume of interest (VOI) are excited and refocused to produce a signal. This voxel localisation method allows the determination of the position and size of the volume, normally guided using ^{1} H images. All localization methods rely on the selection of a spatially selective slice by the application of a frequency-selective RF pulse in combination with a magnetic field gradient. Spatially dependent magnetic field gradients are at the heart of most spatial localization methods and are necessary for *in vivo* NMR spectroscopy to restrict signal detection to a well-defined VOI. Upon spatial localization, the unwanted signals from outside of the VOI, like extracranial lipids in MRS applications of the brain can be removed. Furthermore, the magnetic field homogeneity and water suppression within the VOI can be greatly improved, thereby increasing the spectral resolution. Different methods for achieving voxel localisation are described in the following sections.

Point RESolved Spectroscopy(PRESS)

PRESS is a localization technique which uses a multi echo single shot technique to obtain spectral data from a VOI[78]. PRESS consists of a 90^o excitation pulse and two 180^o refocusing pulses ($90^o - 180^o - 180^o$) (see Fig. 3.10). The 90^o slice selective pulse and associated magnetic field gradient, applied at time t=0, will excite all spins in the plane of the pulse. At time $t = \frac{TE_1}{2}$, the first slice selection 180^o pulse is applied, a spin echo then is formed at time TE_1. The second 180^o pulse is applied at time $t = TE_1 + \frac{TE_2}{2}$, which acts to refocus all the spins in the region acted on by all three pulses, giving a second spin echo at time $t = TE_1 + TE_2$. The three RF pulses are frequency selective and are applied in combination with magnetic field gradients thus leading PRESS to be capable of three-dimensional localization of a voxel. The three slice selective pulses in combination with the gradients are applied perpendicular to each other so that only spins in the VOI are excited to produce a signal. Signal outside this volume is either not excited or not refocused, leading to rapid signal dephasing by crusher magnetic field gradients. A crusher gradient consist of two lobes with the same polarity, one immediately before the refocusing pulse and the second one immediately after. However, after the selective RF pulse is applied in the transversal plane, the transverse magnetization at different spatial locations will generally not lie exactly along its perpendicular axis in the rotating frame due to the different precessional frequency caused by the slice-selection gradient, which dramatically reduces the signal due to phase dispersion. Therefore, slice-refocusing gradient following the slice-selection gradient is used to compensate for phase dispersion deriving from the slice-selection gradient. The slice-refocusing gradient has opposite polarity compared with the slice selection gradient (see Fig. 3.10).

The PRESS sequence becomes increasingly dependent on T_2 as the time between the first and second pulse is increased. This makes PRESS less suitable for detection of signals with short T_2 metabolites. Also, higher power is needed due to the use of two slice selective 180^o pulses. However, PRESS is less susceptible to motion and has a better SNR (100% refocused signal with PRESS compared with 50% with STEAM) than stimulated echo acquisition mode (STEAM).

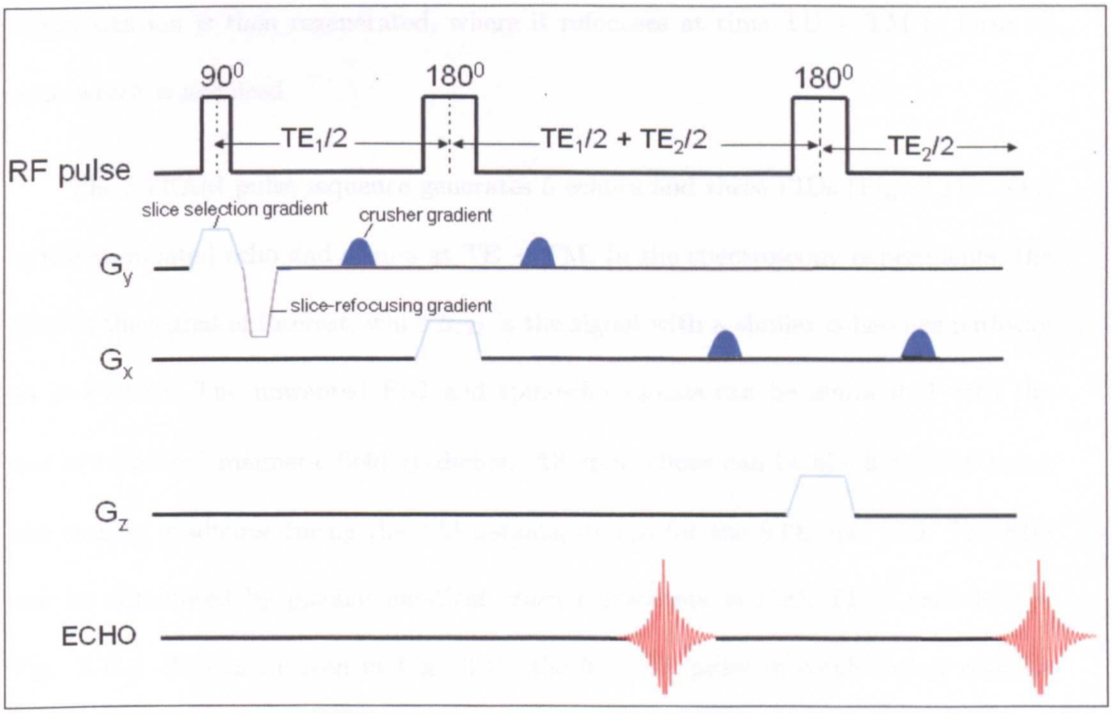

Figure 3.10: Pulse sequence for PRESS localisation. The continuous green line in G_y, G_x and G_z indicates the slice selection gradients, followed by a slice-refocusing gradient lobe (grey). The block blue markers indicate the crushers gradients.

STimulated echo acquisition mode (STEAM)

The STimulated Echo Acquisition Mode (STEAM) sequence is similar to the PRESS sequence (see Fig. 3.11). The essential difference is that STEAM utilizes three slice-selective 90^o pulses ($90^o - \frac{TE}{2} - 90^o - TM - 90^o - \frac{TE}{2} - Acq$) and localization is achieved on a spatially selective stimulated echo, rather than on a spin echo as in PRESS. The first 90^o slice selective pulse and associated dependent magnetic field gradient, applied at time t=0, will excite all spins into the xy plane (generating transverse magnetization). At time $\frac{TE}{2}$ the second 90^o pulse is applied perpendicular to the first one, which rotates this magnetisation into the xz plane. At time TE/2 + TM, the third 90^o pulse rotates the remaining longitudinal magnetisation back into the xy plane and transverse magnetization is then regenerated, where it refocuses at time TE + TM to form an echo which is acquired.

The STEAM pulse sequence generates 5 echoes and three FIDs (Fig. 3.11). STE is the stimulated echo and occurs at TE + TM. In the spectroscopy experiments, the STE is the signal of interest, while S_{123} is the signal with a similar coherence pathway as in PRESS. The unwanted FID and spin-echo signals can be eliminated with the use of "crusher" magnetic field gradients. All spin-echoes can be eliminated by using the crusher gradients during the TM periods, except for the STE and FID. The FID can be eliminated by placing identical crusher gradients in both TE/2 periods (see Fig. 3.11). As can be seen in Fig. 3.12, the first 90^o pulse in combination with its respective gradient rotates all the spins into the transverse plane (A). During a time TE/2 after the first pulse, the magnetization dephases completely due to the effect of the TE crusher gradient and B_0 inhomogeneities (C). At time TE/2, the second 90^o pulse is applied perpendicular to the first one, which rotates this magnetisation into the xz-plane. So that vector 1 and 3 lie on the z-axis, while spin vector 2 and 4 continue to precess (C,D) and form an echo along the -y-axis(E). During the mixing time TM, the transverse components (50% of this magnetisation) decay away with time constant T_2, but spin vectors 1 and 3 decay more slowly, with time constant T_1., Therefore, only a net coherent longitudinal component remains (G). At time TE/2 + TM, the third

90^o pulse rotates the remaining magnetisation (longitudinal component) back into the transverse plane (H), and resumed precession produces another echo, at time TE + TM. This form of echo is known as a stimulated echo and is dependent on T_1 relaxation, but has no T_2 dependence.

The main problem with STEAM is its inherent loss of signal. The refocused signal is only 50% compared with the PRESS sequence, however, this reduction in signal to noise is often compensated for by using the extremely short echo time, down to 1ms [79]. Furthermore, compared with the PRESS sequence, the STEAM sequence has a lower power deposition due to the use of slice selective 90^o rather than 180^o pulses.

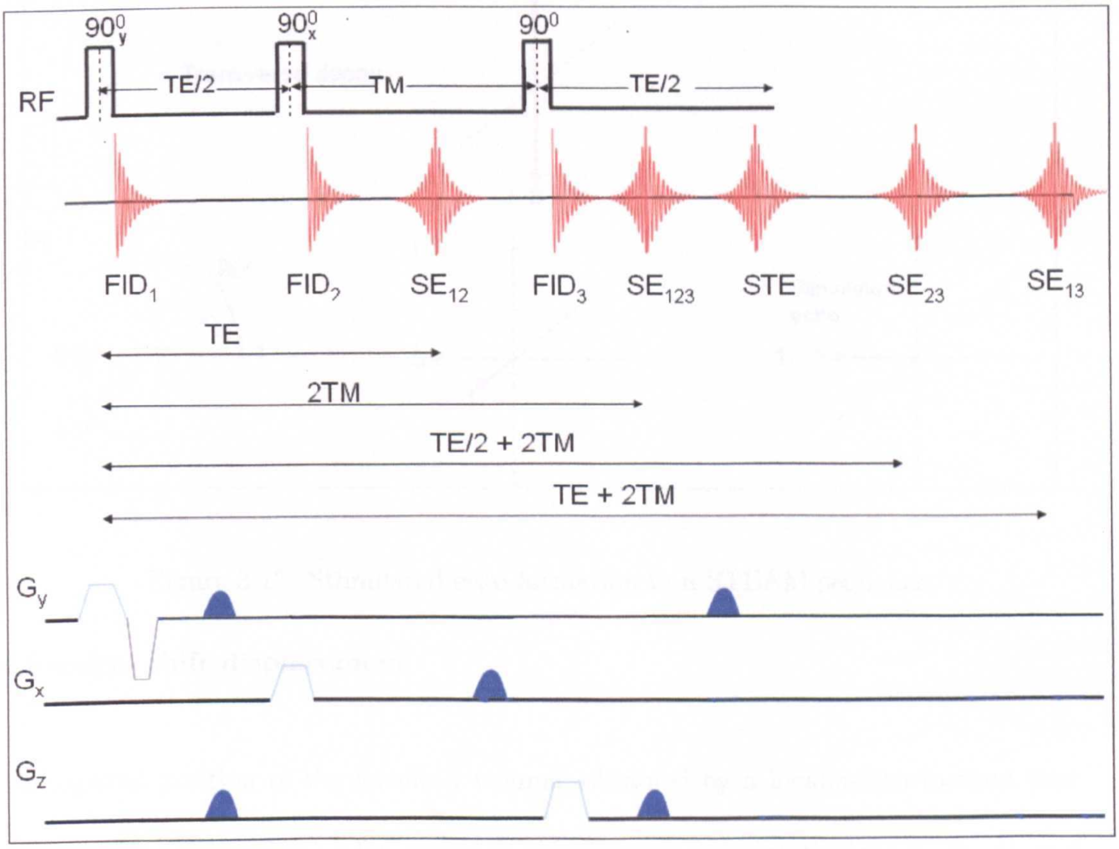

Figure 3.11: Pulse sequence for STEAM localisation. The spin echo SE_{12} is the signal formed by pulse 1 and 2 and occurs at position TE, SE_{13} at TE+2TM, SE_{23} at TE/2+2TM, and S_{123} is the signal occurring at position 2TM (TM=mixing time) and is due to refocusing by pulses 2 and 3 of magnetization excited by pulse 1.

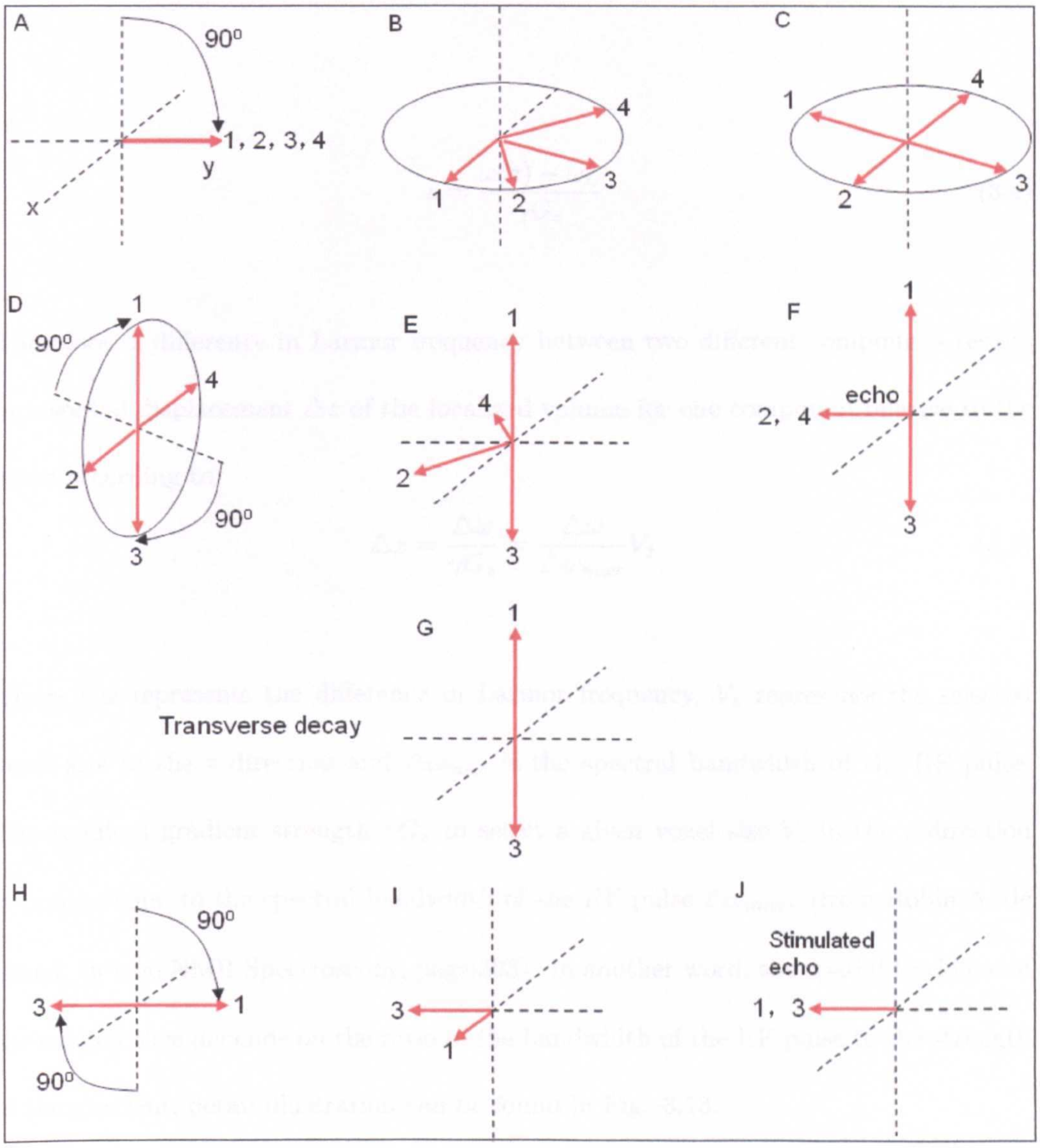

Figure 3.12: Stimulated echo formation in a STEAM sequence.

Chemical shift displacement

The spatial position of the localized volume, obtained by a localization method that employs frequency selective RF pulses in the presence of magnetic field gradients, will be linearly affected by the chemical shift of the compound under investigation. The frequency of spins with Larmor frequency ω_L in the presence of a magnetic field gradient G_z in the z direction is given by:

$$\omega(z) = \omega_L + \gamma z G_z \tag{3.3}$$

or

$$z = \frac{\omega(z) - \omega_L}{\gamma G_z} \tag{3.4}$$

Therefore, a difference in Larmor frequency between two different compounds results in a spatial displacement Δz of the localized volume for one compound relative to the other according to:

$$\Delta z = \frac{\Delta\omega}{\gamma G_z} = \frac{\Delta\omega}{\Delta\omega_{max}} V_z \tag{3.5}$$

where $\Delta\omega$ represents the difference in Larmor frequency, V_z represents the selected voxel size in the z direction and $\Delta\omega_{max}$ is the spectral bandwidth of the RF pulse. The required gradient strength γG_z to select a given voxel size V_z in the z direction is proportional to the spectral bandwidth of the RF pulse $\Delta\omega_{max}$. (from Robin A. de Graaf. in vivo NMR Spectroscopy, page:303). In another word, the spatial thickness of the excited slice depends on the ratio of the bandwidth of the RF pulse to the strength of the gradient, detail illustration can be found in Fig. 3.13.

For example, the difference in Larmor frequency between water(4.7ppm) and glutamate(2.35ppm) at 7T is approximately 700 Hz. For selection of a $2 \times 2 \times 2$ cm volume using a RF pulse with a bandwidth of 4000Hz gives a displacement between the water and Glu resonances in each spatial direction of:

$$\Delta z = \frac{\Delta\omega}{\Delta\omega_{max}} V_z = (700/4000) \times 2cm = 0.35cm \tag{3.6}$$

For the complete 3D volume, the water and Glu resonance only have $\frac{(2cm-0.35cm)^3}{(2cm)^3} = 56.15\%$ of their corresponding voxels in common. This could result in misinterpretations of absolute concentrations.

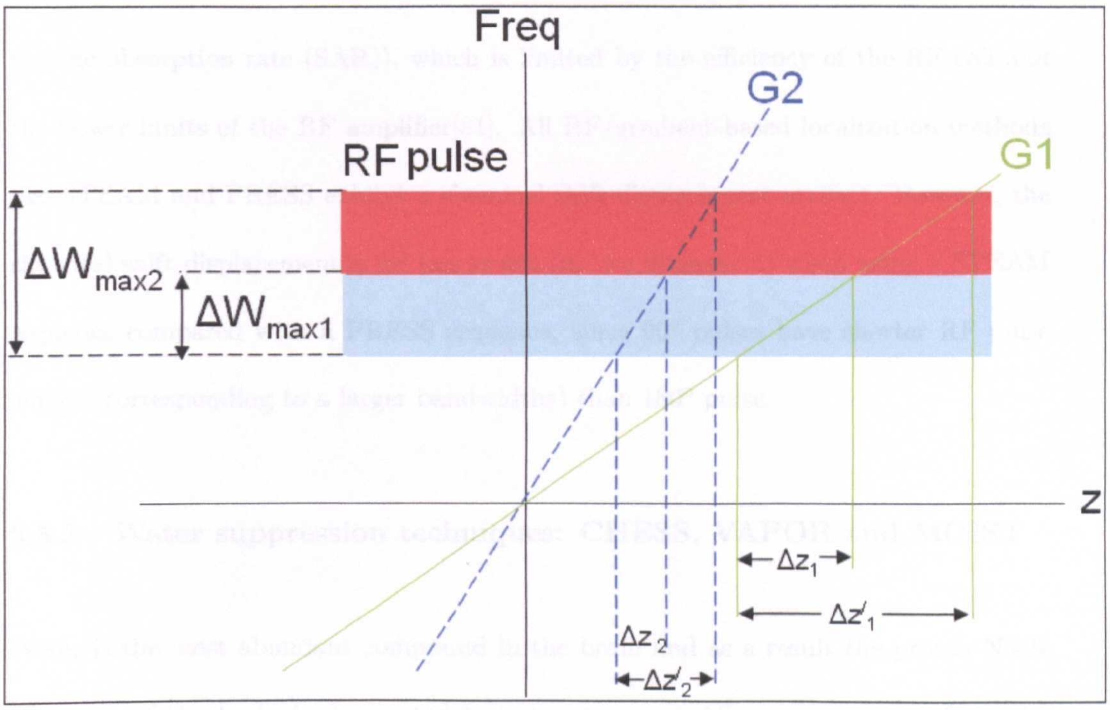

Figure 3.13: Slice selection. RF excitation pulse is applied in the presence of z-gradient. Increasing the bandwidth of the RF pulse (from $\triangle\omega_{max1}$ to $\triangle\omega_{max2}$) with the same gradient strength (G1 or G2) excites a thicker slice (e.g., $\triangle Z_1^{/} > \triangle Z_1$, or $\triangle Z_2^{/} > \triangle Z_2$). Similarly, increasing the gradient strength (from G_1 to G_2) with the same RF bandwidth ($\triangle\omega_{max1}$ or $\triangle\omega_{max2}$) excites a thinner slice (e.g., $\triangle Z_2 < \triangle Z_1$, or $\triangle Z_2^{/} < \triangle Z_2^{/}$).

Equation 3.5 reveals that the chemical shift displacement artifact gets more pronounced at higher magnetic fields (since $\triangle\omega$ increases with magnetic field strength). Also the artifact is inversely proportional to the RF pulse bandwidth[80], as well as proportional to the voxel size. The spatial slice-select offsets between the centres of slices of spins with different chemical shifts can be minimized by increasing the magnetic field gradient strength and shortening the RF pulse length, which (for a constant voxel size) corresponds to an increase in spectral bandwidth of the RF pulse. Overall, broad bandwidth RF pulses permit the use of strong field gradients for the selection and minimization of the chemical shift displacement error. However, higher bandwidth pulses require higher RF power(an increase in RF power implies in turn an increased specific absorption rate (SAR)), which is limited by the efficiency of the RF coil and the power limits of the RF amplifier[81]. All RF/gradient-based localization methods like STEAM and PRESS exhibit a chemical shift displacement artifact. However, the chemical shift displacement is far less severe (in two dimension) when using a STEAM sequence compared with a PRESS sequence, since 90° pulses have shorter RF pulse length (corresponding to a larger bandwidths) than 180° pulse.

3.5.3 Water suppression techniques: CHESS, VAPOR and MOIST

Water is the most abundant compound in the brain and as a result the proton NMR spectrum of the brain is dominated by a resonance at 4.7ppm originating from the two protons of water(e.g. Fig. 3.14(A)). The concentration of metabolites is often over 10000 times lower than that of water. The presence of the large water resonance leads to the baseline distortions and spurious signals due to vibration-induced signal modulation (e.g. Fig. 3.14 (B)) which in turn make the detection of metabolites unreliable [82, 83]. Suppression of the water signal eliminates baseline distortions and spurious signals, leading to a reliable and consistent detection of metabolite spectra (e.g. Fig. 3.14 (C)).

One of most obvious choices for water suppression is to utilize the difference in chemical shift (resonance frequency) between water and the other resonances. Pulse sequences with water suppression are designed in such a manner that metabolites resonance are rotated to the transverse plane for detection, while the water magnetization is returned to the longitudinal axis at the end of the sequence, making it unobservable. However, due to the small chemical shift difference, resonances at or near the water resonance will also be suppressed. Here, water suppression methods utilized throughout this work will be described: CHESS, VAPOR and MOIST.

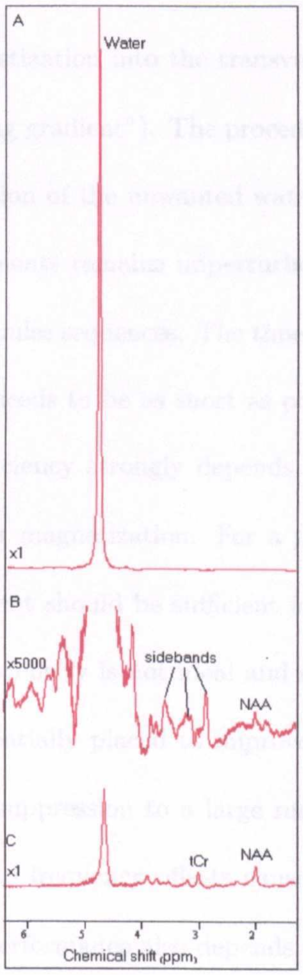

Figure 3.14: Demonstration of the necessity of water suppression in vivo. (A) A localized single voxel ^1H NMR spectrum acquired from visual cortex in the human brain is dominated by the singlet resonance of water. (B) Though small signals can be detected in the presence of a large water signal. Variation-induced sidebands of the water obscure the metabolite signal. Sidebands: an additional frequency produced as a result of a modulation, that is not necessarily present in either of the original signals and can severely interfere with low concentration peaks. (C) Removal of water resonance and consequently any associated sidebands, results in an artifact-free ^1H-NMR spectrum which allows reliable detection and quantification of metabolites.

CHESS method (Chemical-Shift-Selective)

The CHESS method (Chemical-shift-selective saturation) is amongst the most popular of water-suppression techniques[84]. This approach consists of a selective RF pulse which rotates the water magnetization into the transverse plane prior to a dephasing gradient ("homogeneity spoiling gradient"). The procedure leaves the spin system in a state where no net magnetisation of the unwanted water component is retained while the wanted metabolite components remains unperturbed. Therefore, CHESS can be added at the beginning of any pulse sequences. The time gap between CHESS sequence and the first excitation pulse needs to be as short as possible to reduce the signal recovery due to T_1. CHESS efficiency strongly depends on the RF pulse performance in selectively exciting all water magnetization. For a perfectly homogeneous B_0 and B_1 field, a single CHESS element should be sufficient for accurate water suppression. However, in practice, B_0 homogeneity is not ideal and several CHESS elements (usually two to six) must be sequentially placed to improve the suppression. A series of CHESS elements uniform the suppression to a large range of frequency, thus making the suppression less sensitive to frequency offsets caused by B_0 magnetic field inhomogeneity. Furthermore, the performance also depends on the nutation angle and the suppression is perfectly reached only at 90^o. In particular, if the relaxation is not taken into account, the residual longitudinal magnetization M(0) after CHESS elements is a function of the nutation angle $M_z(\theta) = M_0 cos^n(\theta)$. Therefore six CHESS elements would lead the residual magnetization along the z axis to be less than 0.035% for nutation angles, $75^o \leq \theta \leq 105^o$, providing sufficient water suppression with a tolerance to the B_0 inhomogeneity of 30% around the nominal nutation angle of 90^o[84].

More recently, methods have been developed for T_1 and B_0 insensitive CHESS-based water suppression, by optimizing the inter-pulse delay and the nutation angles of the different CHESS elements. These methods include VAPOR and MOIST.

VAPOR method (variable pulse power and optimized relaxation delays)

Suppression of the water signal during ^1H magnetic resonance spectroscopy requires nulling of the longitudinal component of the water magnetization and is therefore affected by T_1 relaxation, RF pulse flip angles (which depend on B_1) and sequence timing. *In vivo* applications, T_1 and B_1 inhomogeneity within the sample may cause spatially inhomogeneous water suppression. VAPOR uses optimized frequency-selective perturbations, interleaved by optimized T_1 recovery delays to make the suppression insensitive to T_1 and B_0 inhomogeneity. The VAPOR method consists of seven CHESS suppression pulses and seven T_1 recovery delays (see Fig. 3.15). For a nutation angle β of 95^o, the longitudinal magnetization prior to nonselective excitation ends up very close to zero despite the presence of T_1 relaxation. Optimizing the last time delay t7 can be performed to adjust the water suppression. Even when the nutation angle is not correctly calibrated, the magnetization can reach close to zero due to the optimized pulse and delay combination.

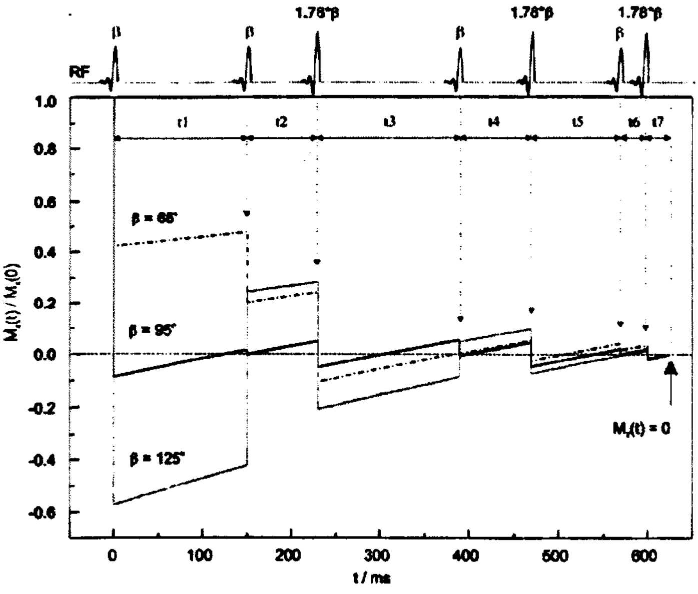

Figure 3.15: Seven CHESS water suppression scheme (VAPOR) with optimized flip angles and timing[79]

MOIST method (Multiply Optimized Insensitive Suppression Train)

MOIST (Multiply Optimized Insensitive Suppression Train) uses a train of four very selective RF pulses designed for B_1 and water T_1 insensitivity, each having a numerically optimized flip angle. Nulling the longitudinal water magnetization requires a fixed relationship between the RF flip angles, the interpulse delays, and the range of T_1 in the voxel. Similar to other water suppression techniques, effective water suppression using MOIST requires complete dephasing of the transverse water magnetization and the nulling of the longitudinal magnetization at the time of the the first RF pulse in the localization sequence. Fig. 3.16 shows a comparison of water suppression efficiency available on our Philips 7T. It can be seen that MOIST achieves the best water suppression performance, showing the smallest residual water/metabolite signal ratio. MOIST method was used for the work in this thesis.

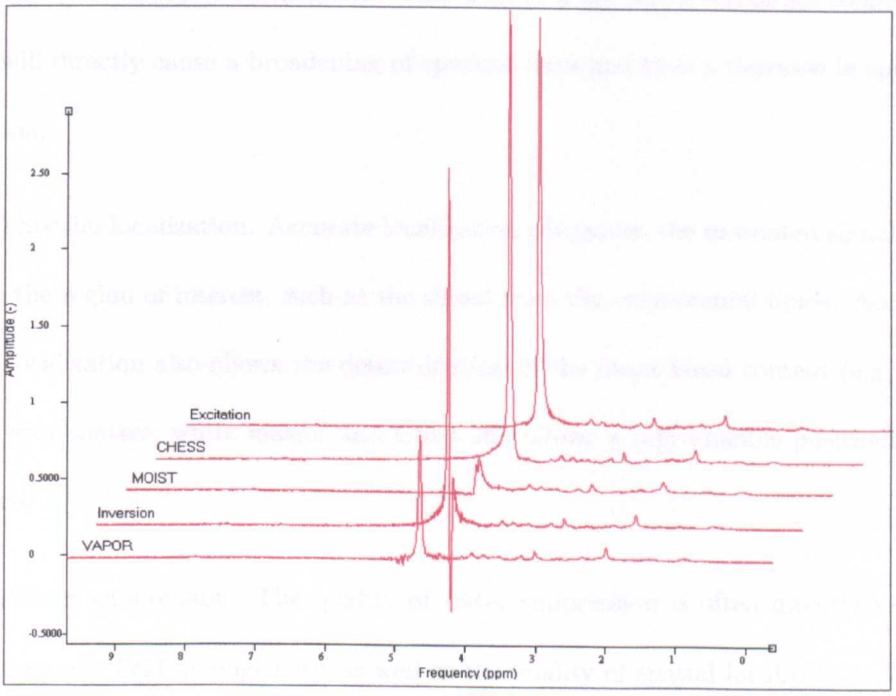

Figure 3.16: Comparison of water suppression efficiency available on the Philips 7T. The ratio of residual water/metabolite signal is the smallest when using the MOIST method, which was used for the work in this thesis.

3.6 Spectral quantification

3.6.1 Data acquisition

The first and the most important step in obtaining reliable metabolite concentrations concerns proper acquisition of the raw time-domain signal. The quality of the acquired signal in terms of sensitivity, resolution, artifacts and general information content directly determines the accuracy and reliability by which metabolite levels can be estimated. A short summary of the important considerations concerning the optimal data-acquisition will be given.

(1) B_0 and B_1 homogeneity. The most important parameters determining the spectrum quality is the magnetic field homogeneity across the region of interest. Inhomogeneity in the external magnetic fields lead to a spread in resonance frequencies which will directly cause a broadening of spectral lines and thus a decrease in spectral resolution.

(2) Spatial localization. Accurate localization eliminates the unwanted signal from outside the region of interest, such as the signal from the extracranial lipids. Accurate spatial localization also allows the determination of the exact voxel content (e.g. fraction of grey matter, white matter and CSF) and allows a reproducible positioning of the voxel.

(3)Water suppression. The quality of water suppression is often directly related to the magnetic field homogeneity, as well as the quality of spatial localization. Water suppression techniques can typically achieve suppression factors of 10000. The shape of the suppressed water resonance is much more important than the absolute suppression. A relatively large, but approximately Lorentzian shaped water resonance can be readily removed by post-processing methods. However, an incompletely dephased water resonance, spreading out over a wide frequency ranges, will lead to a significant baseline distortion, which can not be readily removed by post-processing methods.

3.6.2 Data post-processing

Following data acquisition, a post processing step is often desired to improve the acquired data. Before performing the FT, zero filling and line broadening can be done to enhance the quality of the spectrum. After the FT, phase correction and frequency alignment of multiple spectra, eddy current and lineshape corrections, residual water removal, baseline correction and the exclusion of the additional unacceptable data can be performed to improve the spectral data.

Zero filling

Zero filling is the process of extending the acquired FID (which has decayed to zero amplitude) artificially through adding a string of points with zero amplitude to the FID before FT. This process does not affect the peak positions, intensities and linewidths of the spectrum but the displayed spectrum contains more points and its spectral resolution increases. For a given experiment with 256 points sampled and T_{acq} (acquisition time)=334 ms, giving a dwell time (DW, the delay between samples)=$\frac{T_{acq}}{Nsamples} = \frac{334ms}{256} = 1.3ms$, the Spectral Width (SW)=$\frac{1}{DW} = \frac{1}{1.3ms} = 769Hz$ and the spectral resolution per point is 3 Hz (769Hz/256). This spectral resolution is too low to fully resolve the doublet with a J-coupling of 6Hz, which is only described by three points. Theoretically, better spectral resolution can be achieved through decreasing the spectral width or increasing the acquisition time. However, decreasing the spectral width can lead to a phenomenon called aliasing or folding, in which the peak appears at the wrong position in the NMR spectrum. Furthermore, increasing the acquisition time will lead to increased data storage and increased relative noise contribution as the signal intensity decreases with increasing acquisition time. Alternatively, we can zero fill the acquired data with 2304 points with zero amplitude before FT, we will get a spectrum with 2560 points describing the full 769Hz spectral window. Consequently, the spectral resolution is 10-fold greater (769Hz/2560=0.3Hz per point), and the same doublet peak would be described by 39 data points.

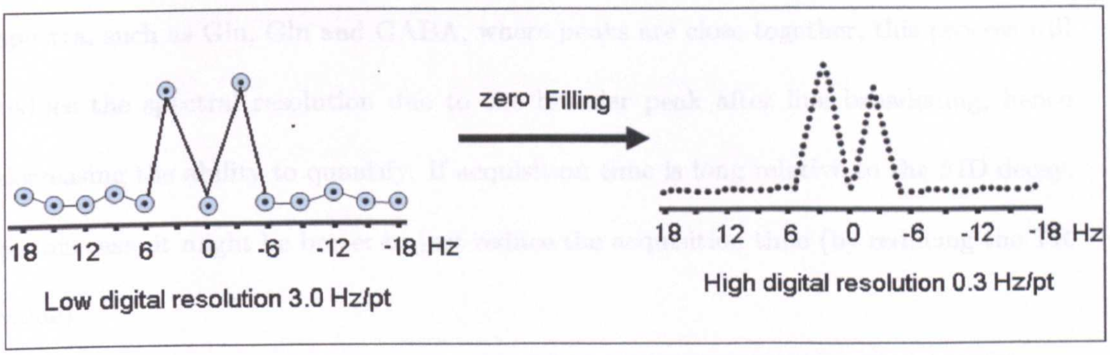

Figure 3.17: Effect of zero filling on the spectral resolution

Line broadening

The FID signal disappears into noise after approx 0.2s (we suppose the T_2 time is smaller than 200ms), even though we acquired data up to 2.0s. The noise from 0.2s to 2.0s in the FID only increases the noise in the spectrum and does not contribute to the peak height, so the SNR is reduced. Simply setting all the data after 0.2s to zero will introduce a sharp discontinuity in the FID at 0.2s, which could introduce artifacts into the spectrum. A smoother method is to multiply the FID by an exponential decay function that emphasizes the early data in the FID and reduces the contribution from later points (mostly noise)(Fig. 3.18). The steepness of this exponential multiplier can be varied but is optimum if it matches the natural decay of the signal. The net effect of line broadening by 2Hz is that the SNR (taking NAA at 2.01ppm as an example) is increased (from 19.3 to 27.5). However, we pay a price in broader peak (5.7 *vs.* 3.7 Hz), because faster decay of the signal leads to a broader peak. The line broadening reduces the absolute peak height, but the reduction in noise level more than compensates for this effect. If spectral crowding is not a problem, the increase in SNR due to line broadening is still worth the price especially for carbon where the signal is always weak. However, for the metabolites with lower concentration and complex multiple spectra, such as Glu, Gln and GABA, where peaks are close together, this process will reduce the spectral resolution due to the broader peak after line broadening, hence decreasing the ability to quantify. If acquisition time is long relative to the FID decay, in this case, it might be better to just reduce the acquisition time (by reducing the TR value).

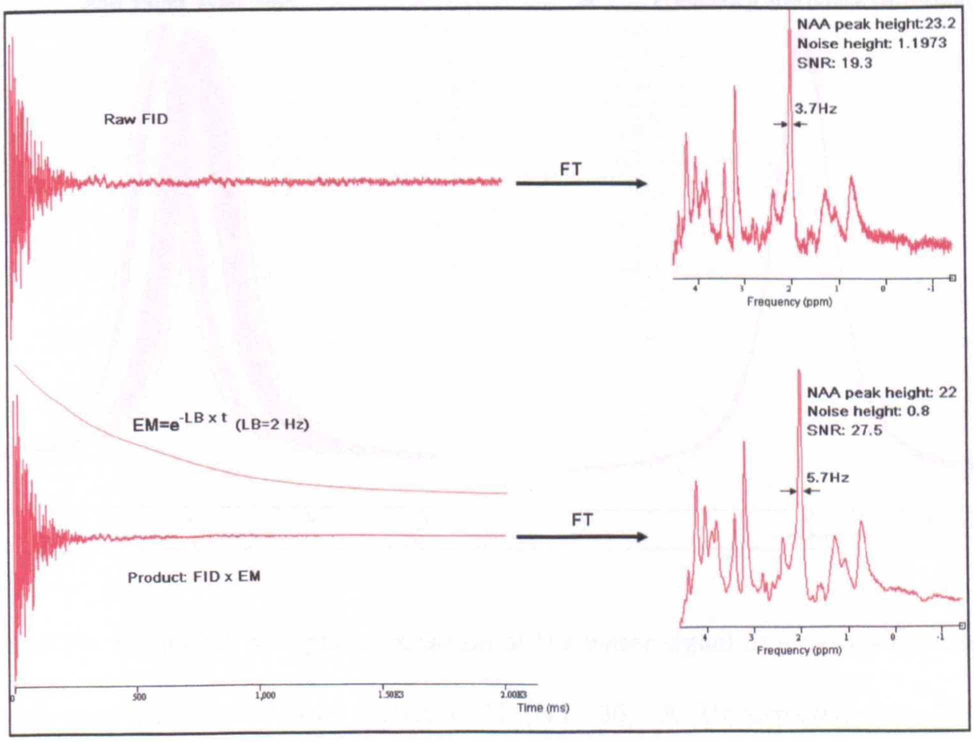

Figure 3.18: Effect of line broadening on the spectral resolution

Phasing and frequency alignment

High spectral quality is desirable for reliable and reproducible quantification of metabolites. To acquire the highest possible spectral resolution at high fields, elimination of all effects that unnecessarily increase the linewidth is desirable. Physiological motion, such as breathing and small random motions of the head, can cause frequency variations up to $\pm 2Hz$ at 7T [85] as well as phase fluctuation (Fig. 3.19 A). The frequency and phase fluctuations will reduce the SNR and increase the linewidth of the spectra. Both effects can be easily minimized by saving each acquired FID separately on disk and by applying corrections (including zero-order phase correction using jMRUI[86, 87] and frequency alignment using MATLAB [88]) after FT and before summation (Fig. 3.19.B). The correction significantly improves the spectral quality, reducing lineshape distortions and preventing signal loss.

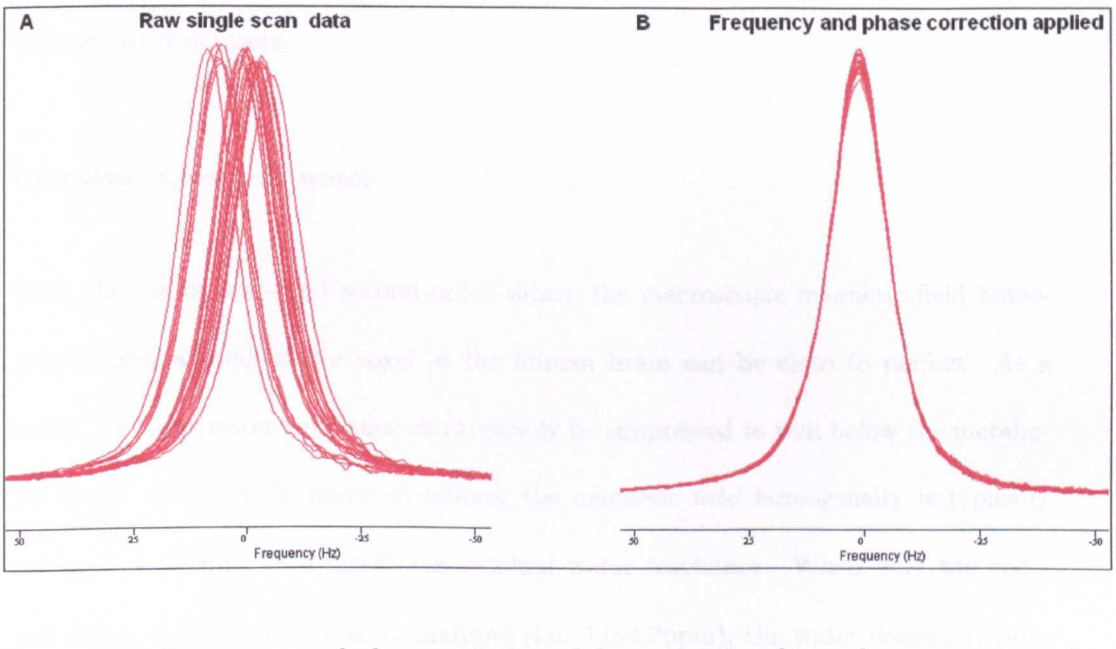

Figure 3.19: Frequency and phase variation of the water signal in a data set measured in single-scan mode from visual cortex at 7T (NT=36). A: Uncorrected data; B: data after frequency and phase correction.

Line shape correction

NMR resonance lines obtained *in vivo* are typically not well behaved due to residual eddy currents, magnetic field inhomogeneity and multi-exponential relaxation. Residual eddy currents are typically unavoidable and can lead to a time-varying magnetic field during signal acquisition, which distorts the NMR resonances. However, the time-varying magnetic fields are the same for all resonances. Therefore, when an unsuppressed on-resonance water signal is acquired, any temporal frequency variations in the water time-domain signal can be attributed to residual eddy currents. Applying the opposite phase modulation to the metabolite spectrum thus automatically cancels phase modulations due to residual eddy currents. Since the water and metabolite spectra are acquired with the same NMR sequence, the eddy current correction automatically performs a first-order phase correction which provides a tool for the automated phasing of large MRS datasets.

Removal of residual water

With the use of first- and second-order shims, the macroscopic magnetic field homogeneity over a small single voxel in the human brain can be close to perfect. As a result, the large water resonance can typically be suppressed to well below the metabolite levels. However, in many situations, the magnetic field homogeneity is typically not perfect, leading to a significant residual water resonance. When only the spectral region upfield from water is analyzed (i.e. 1.0-4.2ppm), the water doesn‘t require any further consideration provided that it does not distort the baseline. However, in cases where the water resonances do distort the baseline or when the complete spectral range is included in the fitting algorithm, the residual water resonance can still be removed. Hankel-Lanczos Singular Value Decomposition (HLSVD) is a reliable technique to remove the residual water resonance, which is based on the Lanczos algorithm and requires the computation of the truncated singular value decomposition of a Hankel matrix H [89]. Following a HLSVD, the singular values with frequencies corresponding to the water spectral region (indicated in Fig. 3.20A) are selected, the corresponding reconstructed NMR spectrum largely resembles the water resonance. Subtraction of the reconstructed water (Fig. 3.20 B) form the original spectrum yields a water-suppressed metabolite spectrum as shown in Fig. 3.20C.

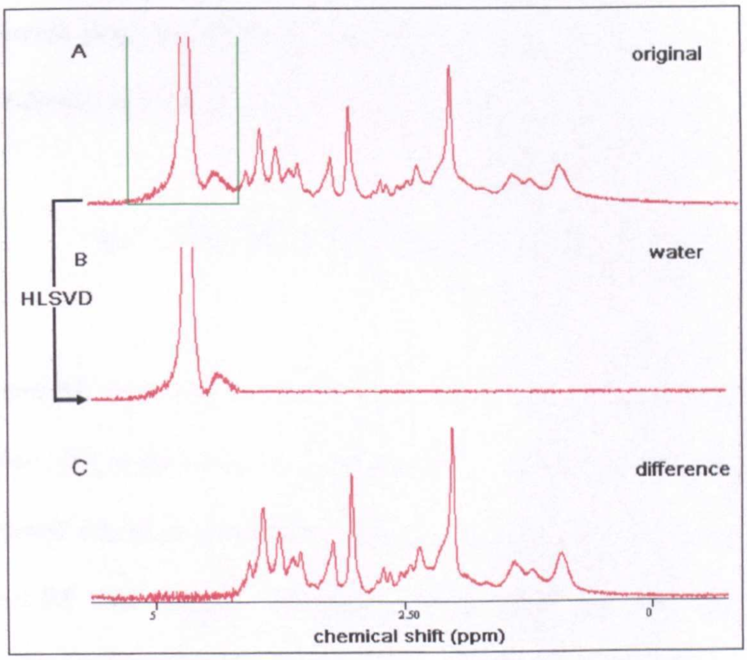

Figure 3.20: Post-acquisition water removal through the use of a HLSVD algorithm. A: Short TE ^{1}H NMR spectrum acquired from human visual cortex at 7.0T, displaying a relatively small amount of residual water signal. B: Theoretical water spectrum calculated from the singular values generated by a HLSVD of spectrum (A) of which the frequencies fall within the indicated boundaries. C: Difference between A and B.

3.6.3 Data quantification

Spectra obtained using MRS can be used to derive absolute concentrations, expressed in mmol L^{-1} or $\mu molg^{-1}$ of tissue in animal and human tissues *in vivo*. This originates from the fact that the thermal equilibrium magnetization M_0 is directly proportional to the number of spins N, which is proportional to the molar concentration. However, the thermal equilibrium magnetization M_0 can not be detected directly, but rather an induced current proportional to the transverse magnetization is observed. The signal from a metabolite M induced in a receiver coil following a particular MR sequence is given by:

$$S_M = NS \times RG \times \omega_0 \times [M] \times V \times f_{sequence} \times f_{coil} \tag{3.7}$$

where NS and RG equal the number of scans and receiver gain setting, ω_0 is the Larmor frequency, [M] is the molar concentration, V is the volume size. $f_{sequence}$ and f_{coil} are complicated functions describing the signal modulations due to the NMR pulse sequence and RF coil. $f_{sequence}$ will depend on the repetition time TR, the echo-time TE, the number and type of RF pulses, as well as the T_1 and T_2 relaxation times. f_{coil} contains factors related to the geometry and quality of the RF coil. However, several coil related factors in the f_{coil} function are unknown, and therefore direct calculation of the metabolite concentration [M] from the detected signal S_M is not possible. In practice all quantification methods utilize a calibration or reference compound with known concentration [R] (internal or external reference) to which the detected metabolite signals are referenced such that the metabolite concentration can be calculated according to:

$$[M] = [R]\frac{S_M}{S_R}C_{MR} \tag{3.8}$$

where S_R is the detected signal from the reference compound and C_{MR} is a correction factor accounting for differences in relaxation times T_1 and T_2, diffusion, gyromagnetic ratio, magnetic susceptibility, spatial position relative to the coil and, in general, any other differences between the reference compound and the metabolites.

The external reference method is based on the idea of repeating the identical NMR experiment (under identical experimental conditions as in vivo) in a phantom containing an aqueous solution of a reference compound with known concentration. An internal reference has conceptual simplicity and directness, because metabolite and internal reference signals are both acquired from the same VOI under the same loading conditions. The internal reference method is also insensitive to many of the experimental factors affecting the performance of the quantitative techniques, including effects related to loading, standing waves, B_1 inhomogeneities, practical issues of phantom positioning and user expertise and examination duration. ^{1}H MRS with internal reference exploiting tissue water has been usually used to acquire absolute metabolites concentration.

Since the calculation of a reliable correction factor C_{MR} can be very time-consuming, metabolite ratios have been widely used as an alternative for *in vivo* MRS, especially in the clinical field. The most compelling reason was that the correction factor C_{MR} is identical for both metabolites and ratios will not be sensitive to several experimental unknowns, difficult to obtain, or uncontrollable experimental conditions, e.g: B_1 inhomogeneities, instrumental gain drifts, localization method differences and voxel partial volume contamination from CSF[90]. However, unlike absolute concentrations, metabolite ratios can not give unambiguous information about metabolic changes. For example, an increase in the NAA-to-Cr ratio could mean that (1) the NAA concentration has increased, (2) the Cr concentration has decreased, (3) both the NAA and Cr concentration have changed. In order to reach conclusive statements about metabolic changes it is therefore crucial that absolute concentrations are obtained.

3.7 *In vivo* ^{13}C magnetic resonance spectroscopy

The element carbon consists of the stable isotopes ^{12}C and ^{13}C with 98.9 % and 1.1 % natural abundance, respectively [91]. Only the ^{13}C nucleus has a magnetic moment with I= 1/2, while the ^{12}C nucleus of the major isotope is non-magnetic. Therefore, nuclear magnetic resonance spectroscopy of carbon is limited to the investigation of ^{13}C. Furthermore, the gyromagnetic ratio of ^{13}C is only approximately one-fourth of that of the proton. Consequently, ^{13}C NMR spectroscopy is far less sensitive than ^{1}H MRS. There is usually no observable spin-spin splitting due to the adjacent carbons, because of the low natural abundance of ^{13}C.

Methods of *in vivo* ^{13}C MRS can be divided into two general strategies. The first strategy is natural abundance spectroscopy which is only limited to the metabolites with a high concentration in the body, such as glycogen and lipids. Glycogen plays an important role in human energy metabolism, being the natural storage form of glucose. Hence such studies are important for the understanding of normal carbohydrate metabolism and glycogen storage diseases like diabetes. Lipids, normally referred to as EMCL and IMCL (Intra- and Extramyocellular Lipids). EMCL is metabolically relatively inert, while IMCL can be mobilized and utilized for energy metabolism during exercise. IMCL levels has been found to be sensitive to physical exercise[92, 93, 94] and diet [95, 96]. The second strategy is ^{13}C-labelled enrichment, which allows label incorporation into active metabolites to be measured (Fig. 3.21). *In vivo* ^{13}C-MRS combined with ^{13}C-labelling administration is a useful tool to measure the synthesis rates and turnover of specific neurotransmitters non-invasively in the brain [97, 98, 99].

The chemicals that can most easily be detected with ^{13}C-MRS in the brain during infusions of ^{13}C-labeled substrates are Glc, Glu, Gln and GABA, which can be synthesized rapidly in about an hour [100]. Furthermore, many kinds of metabolic flux rates including astrocytic and neuronal Glc oxidation, Glu-Gln neurotransmitter cycling, GABA-Gln cycling, Gln synthesis, Pyr carboxylase flux, GABA synthesis, as well as neuronal α ketoglutarate-Glu exchange and other parameters can be determined from the measured time courses of appearance of label and fractional enrichments obtained experimentally with a metabolic model[101, 102, 72, 103, 104, 105, 106]. All these observations make it clear that ^{13}C MRS provides a unique insight into brain metabolism, with a chemical specificity and diversity of potential measurements not possible by other methods.

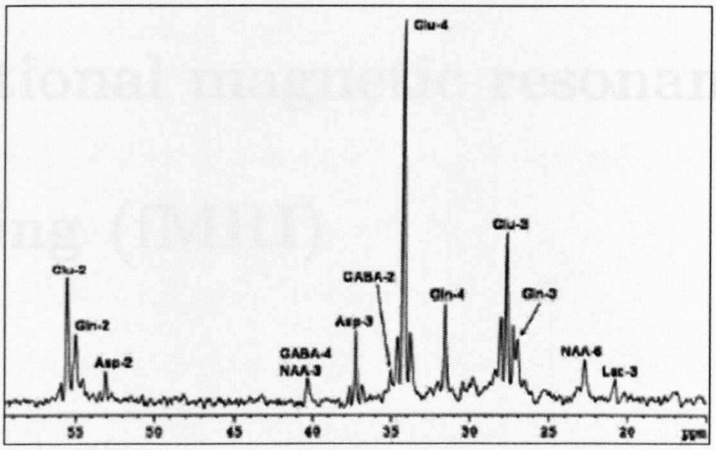

Figure 3.21: An example localized ^{13}C NMR spectrum of the rhesus monkey brain. The spectrum was accumulated for 1 hour from 80 to 140 min after the start of [1-^{13}C]glucose infusion. Twelve signals are clearly observed: Glu C2 (55.5ppm), Gln C2(55.0ppm), Asp C2(53.0ppm), GABA C4 and NAA C3(40.2ppm), Asp C3(37.4ppm), GABA C2(35.2ppm), Glu C4(34.2ppm), Gln C4(31.7ppm), Glu C3(27.8ppm), Gln C3(27.1ppm), NAA C6(22.8ppm) and Lac C3(21ppm)[107].

Chapter 4

Functional magnetic resonance imaging (fMRI)

4.1 Introduction

The brain consists of neurons and glial cells that mutually influence each other and collaborate to maintain normal brain function. It requires large amounts of energy to maintain homeostasis and to perform work. Energy is carried in the blood in the form of glucose and oxygen. Glucose is transported across the blood-brain barrier (BBB) and can be metabolized by anaerobic glycolysis and aerobic glycolysis in both glial cells and neurons. Neuronal activation triggers increased glucose consumption and glucose demand, with new glucose being brought in through the BBB by a stimulated increased cerebral blood flow (CBF)[108]. So a local increase in neural activity is coupled to an increase in CBF, glucose use and oxygen use[109].

Functional MRI (fMRI) and the basic method of BOLD imaging were introduced in 1993 by Seiji Ogawa [110]. fMRI is a relatively new procedure that uses MR imaging to measure the small metabolic changes that take place in the active part of the brain. Neurovascular and neurometabolic coupling help the brain to maintain an appropriate energy flow to the neural tissue under the conditions of increased neuronal activity. Brain activity is relatively localized. For example, when you have a light flashed in your eyes, an area of your brain known as the visual cortex responds. This leads to an increase in energy metabolism in that area. This also causes an increase in blood flow to create a large oxygen gradient to deliver oxygen rapidly. It therefore increases local blood oxygenation.

fMRI is based on detecting changes in the magnitude of the MR signal, due to a local increase in blood oxygenation resulting from elevated blood flow in active brain tissue. The principle of measurement is based on the assumption that there is a strong coupling between changes in neural activity, metabolism, vascular response and oxygen extraction in the area under investigation. fMRI does not measure neural activity directly, but relies on a cascade of physiological events linking neural activity to generate the signal.

4.2 Response to neuronal coupling

Neuronal activity triggers various responses that act together to adapt the delivery of energy substrate to the local neuronal needs. These responses are outlined in the following sections.

4.2.1 Neurovascular coupling

In addition to the neurons and glial cells in the brain tissue, there is a third cell partner, the vascular cell. Blood vessels are linked to neuronal function through the process of neurovascular coupling, that is, the coupling of vessel diameter and thus blood flow, to neuronal activity (see Fig. 4.1) [111]. Neurovascular coupling or functional hyperemia matches the supply of blood and nutrients to the local needs of the brain cells and brings about an increased blood flow after local neuronal activation. Neuronal activation triggers regional glucose consumption and glucose demand. As expected from neurovascular coupling, regional glucose use and consumption in the brain is strongly correlated with the local blood flow [112], therefore linking neuronal activity, glucose metabolism and cerebral blood flow.

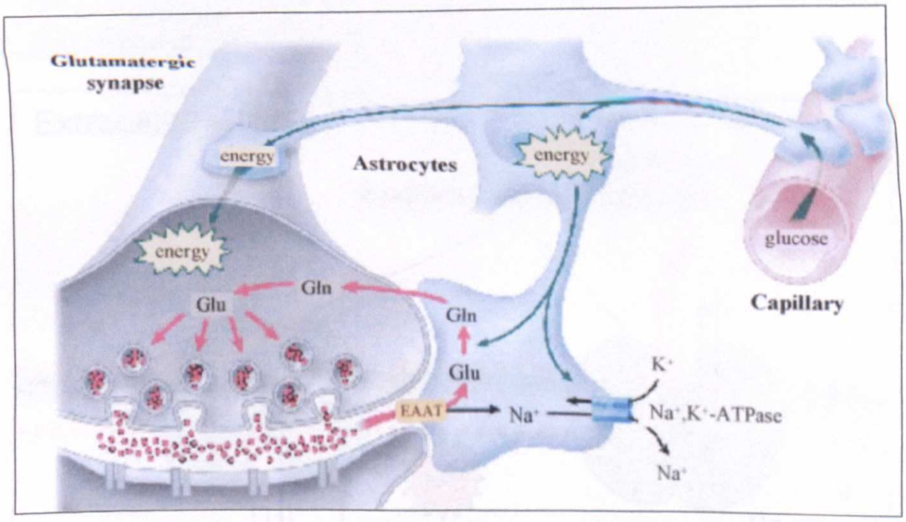

Figure 4.1: Cytological association between capillaries, astrocytes, and neurons in the mammalian brain provides the framework of neurovascular coupling[113].

4.2.2 Neurometabolic coupling

Neurometabolic coupling involves interactions (signals and transport) between neurons and astrocytes that trigger the glycolytic breakdown of glucose. It denotes the stimulation of increased energy metabolism to keep up with cellular ATP consumption. During neuronal activity, Glu is released from glutamatergic synapses and then is taken up by the astrocytes in co-transport with three sodium (Na^+) ions, whereas two potassium (K^+) ions are transported out[114] (see Fig. 4.1). Subsequent transport of three Na^+ ions out of astrocytes by plasma membrane Na^+/K^+-ATP_{ase} on astrocyte end-processes would consume one molecule of ATP[115, 116] (see Fig. 4.2). Synthesis of Gln from Glu and ammonia through Gln synthetase would require one more ATP molecule. These processes increase the astrocytic ATP consumption and drive glycolysis to back up the cellular ATP content. The product of glycolysis in astrocytes is Lac, which is assumed to be shuttled to the neurons for further breakdown in the TCA cycle[116, 117]. The neuronal Glu release and astrocytic glucose metabolism are therefore closely linked[118].

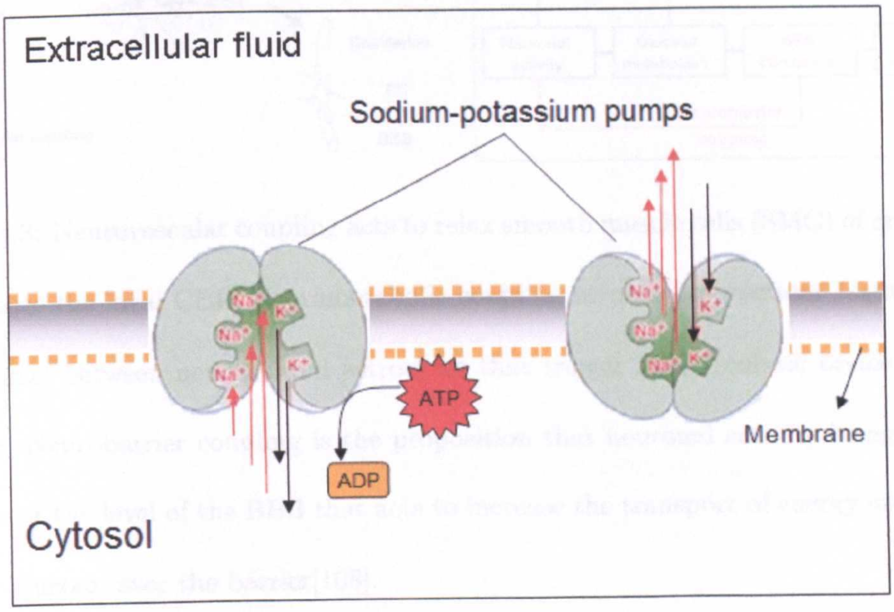

Figure 4.2: sodium-potassium pump

4.2.3 Neurobarrier coupling

Neurobarrier coupling is the proposition that neuronal activity brings about changes at the level of the BBB that act to increase the transport of energy substrate, mainly glucose, over the barrier[108]. Neurobarrier coupling involves the endothelial cells (EC) that make up the BBB. It has recently been suggested that astrocyte (same as glial cells) may play an important role in controlling changes in blood flow coupled to neural activity [119]. Astrocyte anatomy is ideal for regulating blood flow in response to local neuronal activity. Most of their cell membrane surrounds the neurons so can sense the neuronal Glu release. Astrocytes have extensions (endfeet) that are in close association with the majority of BBB endothelial cells, opening up the possibility that astrocytes-to-endothelial communication is involved in neurobarrier coupling.

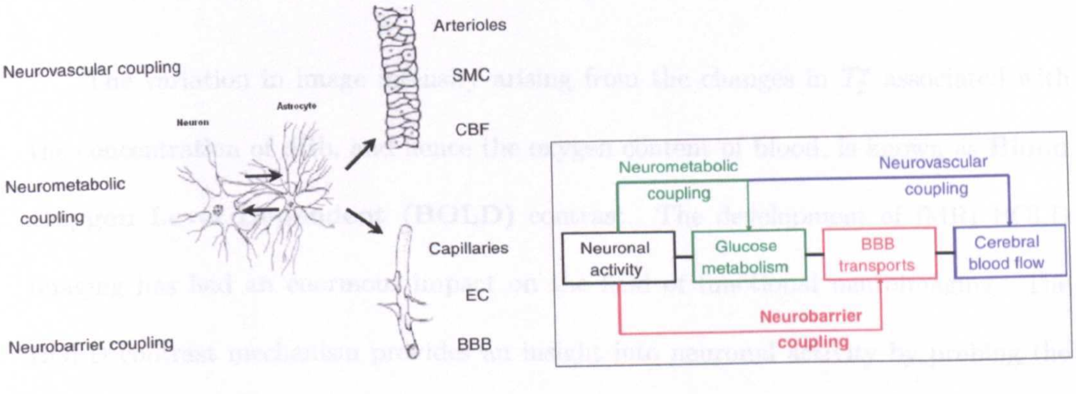

Figure 4.3: Neurovascular coupling acts to relax smooth muscle cells (SMC) of arterioles to increase the local CBF. Neurometabolic coupling involves interactions (signals and transports) between neurons and astrocytes that trigger the glycolytic breakdown of glucose. Neurobarrier coupling is the proposition that neuronal activity brings about changes at the level of the BBB that acts to increase the transport of energy substrate, mainly glucose, over the barrier[108].

4.3 Blood oxygenation level dependent (BOLD) contrast

The main fMRI contrast mechanism (BOLD) relies on the difference in magnetic properties of oxyhaemoglobin (Hb) and deoxyhaemoglobin (dHb)[111]. dHb is strongly paramagnetic: the Fe in the haemoglobin groups is in a high-spin ferrous (Fe^{2+}) state with 4 outer unpaired electrons . On oxygenation one of the electrons is transferred to the bound O_2 molecule and the haemoglobin changes to a low spin state which is diamagnetic. Hb is closely matched to the susceptibility of surrounding tissue, whilst dHb is paramagnetic relative to surrounding tissue. The susceptibility (χ) mismatch with surrounding plasma and tissue leads to a locally inhomogenous magnetic field distribution. This magnetic field shortens the T_2^* of deoxygenated blood and surrounding tissues. In summary, a rise in blood oxygenation increases the ratio of Hb (diamagnetic) to dHb (paramagnetic), which increases the T_2^* of extravascular tissue water.

The variation in image intensity arising from the changes in T_2^* associated with the concentration of dHb, and hence the oxygen content of blood, is known as **Blood Oxygen Level Dependent (BOLD)** contrast. The development of fMRI BOLD imaging has had an enormous impact on the field of functional neuroimaging. The BOLD contrast mechanism provides an insight into neuronal activity by probing the corresponding haemodynamic response.

4.3.1 Haemodynamic response function(hrf)

From the basic theory of the BOLD effect, a signal change is observed when the local deoxyhemoglobin content is altered. When a region of the brain is active, the regional blood flow and blood volume are substantially increased, but the oxygen consumption increases only slightly. The net result is an increase in the venous oxygenation, so a decrease in the proportion of deoxyhaemoglobin, an increase in T_2^* and hence an **increase** in tissue signal.

The **haemodynamic response function (hrf)** (see Fig. 4.4) is the time course of BOLD signal change due to stimulation. There are three key features: (1) A transient undershoot before the initial rise ("deoxy dip") has been reported and is suggested to be due to a drop in venous oxygenation before the blood flow increase has effect. (2) Following the initial dip $\sim 2s$ from stimulus onset, a large increase in local blood flow occurs along with a proportionate increase in glucose consumption. The increase in flow also means an increase in oxygenated blood which actually overcompensates for the oxygen consumption in the area[3, 4]. (3) A prolonged undershoot after the end of stimulation. This is argued to be due to stretching of venous vessels in response to increased blood flow (Balloon model).

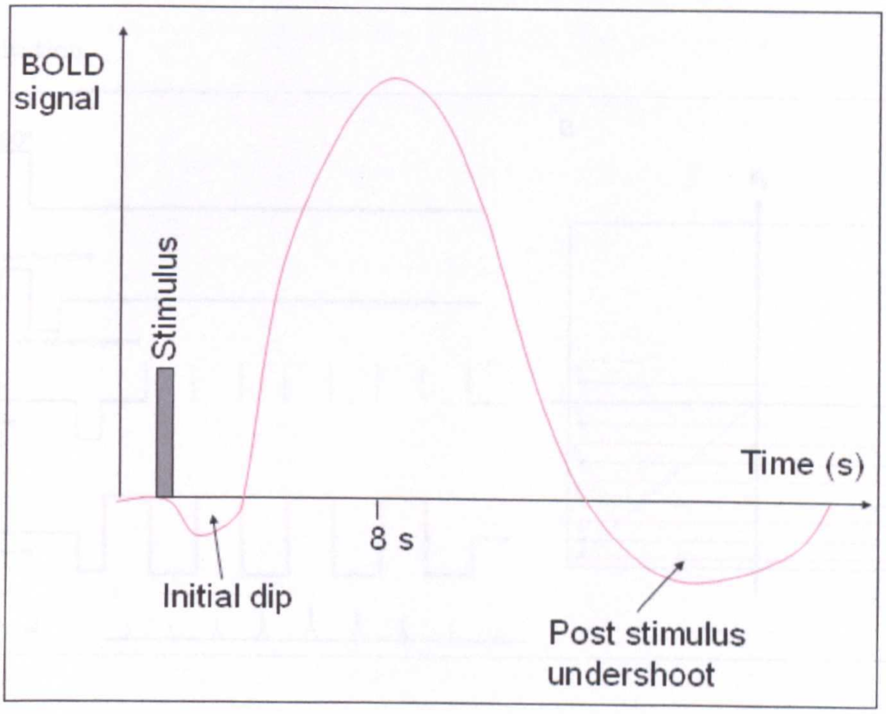

Figure 4.4: Haemodynamic response function(hrf)

4.4 Echo planar imaging

In 1977 Peter Mansfield proposed a method, Echo-Planar Imaging (EPI), to fill the entire k-space (refers to the raw data before reconstruction, usually a matrix, in which data from digitized MR signals are stored during data acquisition.) with rapid gradient switching following a single excitation. The development of EPI played a crucial role in advancing the field of functional imaging in MR. This ultra-fast imaging technique allows 2D images to be acquired in a few tens of milliseconds, making it ideal for applications such as: diffusion, perfusion, cardiac and BOLD imaging.

EPI (Fig. 4.5) uses a single shot gradient echo sequence and employs rapidly switching, bipolar readout gradients to generate a chain of gradient echoes, which are individually phase encoded, hence all lines in k-space can be mapped following a single RF excitation.

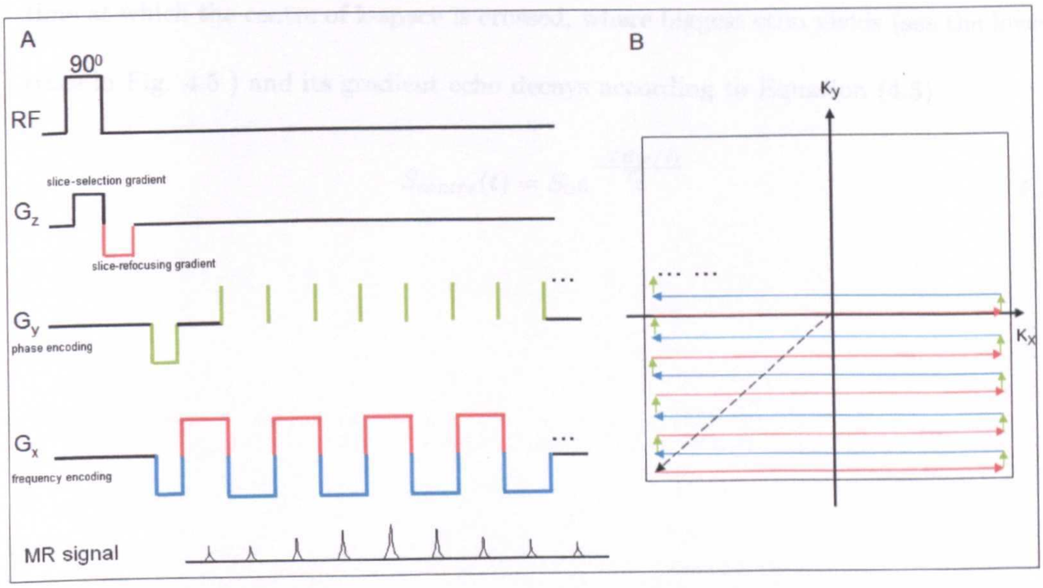

Figure 4.5: An EPI pulse sequence(A) and its k-space trajectory(B). Note that the directions of gradients are changed rapidly over time to allow the back-and-forth trajectory through k-space.

If the MR signal is considered (Fig. 4.5), it can be seen that, following an RF excitation, the transverse magnetization M_z decays according to Equation(4.1).

$$M_z(t) = M_z(0)e^{\frac{-t}{T_2^*}} \tag{4.1}$$

EPI has high T_2^* weighting. It maximally uses the transverse magnetization by implementing multiple acquisitions before the magnetization decays away due to T_2^* relaxation. For each acquisition, the corresponding gradient echo decays according to

Equation (4.2).

$$S_n(t) = S_0 e^{\frac{-TE(n)}{T_2^*}} \tag{4.2}$$

where n is the echo index in the echo train. Therefore, the degree of T_2^* weighting in the image can be altered by manipulation of the TE.

However, the contrast of the image is determined by the effective echo time (TE_{eff}), time at which the centre of k-space is crossed, where biggest echo yields (see the lowest trace in Fig. 4.5) and its gradient echo decays according to Equation (4.3).

$$S_{centre}(t) = S_0 e^{\frac{-TE(eff)}{T_2^*}} \tag{4.3}$$

Chapter 5

Investigation of metabolic changes in human visual cortex during neuronal activity using functional ^{1}H MRS at 7T: An initial study

5.1 Introduction

Functional proton MR Spectroscopy (fMRS) allows direct measurement of metabolic changes during neuronal activation through continuous acquisition of MR spectra[22, 7, 120, 121, 23]. This can provide great insight into the brain neurotransmitter activity and metabolic pathways used for energy synthesis during activation in working brain, which is of great importance for investigating the biomarkers for the neuropsychiatric and neurodegenerative diseases. Previous NMR studies of the activated human brain were mainly focused on observing Lac changes at lower magnetic fields, under a variety of experimental conditions and functional paradigms[22, 7, 122, 21]. However, increased spectral resolution and signal-to-noise ratio (SNR), available at 7T, provides improved metabolite discrimination and quantification[1]. More recent studies by Mangia *et al*, used a visual checkerboard stimulus at 7T, to investigate many more proton metabolic changes under two paradigms of visual stimulation lasting 5.3 and 10.6 minutes[23]. They observed Lac increased by 23% ± 5%, Glu increased by 3% ± 1%, Asp decreased by 15% ± 6% and the Glc concentration showed a tendency to decrease, during the activation periods. These results suggest a rise in oxidative energy metabolism under stimulation conditions.

Given that at 7T, the principle excitatory and inhibitory neurotransmitters (Glu and GABA, respectively) and glutamine (Gln) are well resolved [1], we therefore set out to establish whether there was evidence for stimulus-related changes in neurotransmitter levels. It has been well established that increased energy demands arising from visual stimulation stimulate blood flow and Glc oxidation [111, 112]. Glc is a necessary substrate to maintain neurotransmitter homeostasis during synaptic activity[123]. Since the main function of neurons is neurotransmission, it is not surprising that Glc energy consumption and neurotransmitter recycling rates have been observed to be correlated[26, 103]. Therefore, observations of increased Glu due to stimulation might be expected to be accompanied by changes in Gln or GABA, due to increased cycling rates during activation. If cycling rates of Glu and or GABA are increased it is likely that there will be a relative change in the proportions of the neurotransmitters and of Gln. However, these changes have not been previously discussed or measured.

5.2 Aim

The aim of this initial study was to confirm and quantify the changes in the levels of Glc, Lac, Glu and Asp and to further investigate GABA and Gln in response to functional visual stimulation.

5.3 Methods

5.3.1 Human subjects

Nine healthy subjects (6 males, 3 females, $age = 28 \pm 3$) without history of neurological disorders participated in this study. The study was ethically approved by the University of Nottingham Ethics Committee. All MR measurements were acquired using a Philips Achieva 7T MR system and a 16-channel SENSE head coil from Nova Medical.

5.3.2 Visual stimulus paradigm

The visual stimulus was delivered with red flashing light emitting diode (LED) goggles flickering at a frequency of 8 Hz. The flashing LEDs were positioned at the end of optical tubes which carried the signal into the scanner. The paradigm comprised two 9.9 minutes rest periods interleaved with two 9.9 minute stimulation periods (see Fig. 5.1).

5.3.3 Scanning protocol

An initial survey was carried out to enable positioning of slices for the fMRI task. An fMRI experiment was then performed (EPI, TE=26ms, TR=2200ms, spatial res-

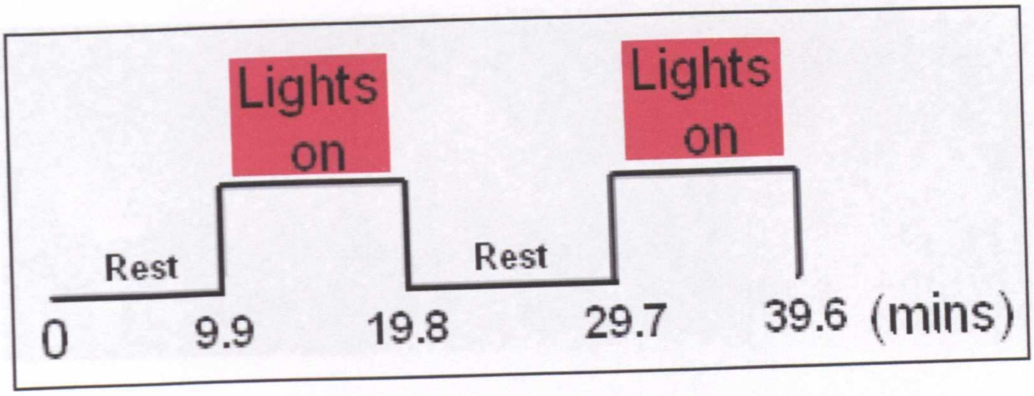

Figure 5.1: Paradigm for ^{1}H visual stimulus experiment

olution=2mm, functional paradigm: 4.4s stimulation and 28.6s rest, 8 repeats), to allow the activated regions to be immediately processed using the IViewBOLD software available on the Philips Achieva system. A 2cm cubic voxel was then positioned in the region of maximum activation in the visual cortex (defined from the fMRI study) for acquisition of the ^{1}H MR spectra (see Fig. 5.2). A STEAM sequence (TE/TM/TR=15/17/3000ms, spectral bandwidth 4000Hz, 4096 time points) was used for acquiring the metabolic data. Spectra were collected in blocks of 32 averages, with 6 blocks per 9.9 minute period ($(32+1) \times 3s \times 6 = 594s = 9.9minutes$). Water suppression was performed using CHESS [124]. A scan without water suppression was acquired at the beginning of every block for eddy current correction and for metabolite quantification.

5.3.4 Post-processing

Spectra were saved separately and then averaged into groups for further analysis in jMRUI and LCModel. Spectra from each subject acquired during two 9.9-minute resting and two 9.9-minute stimulation periods were summed accordingly for metabolite quantification. A group difference spectrum (Fig. 5.4) was generated using spectra from 9 subjects (group analysis). Specifically, the averaged spectrum acquired during two 9.9

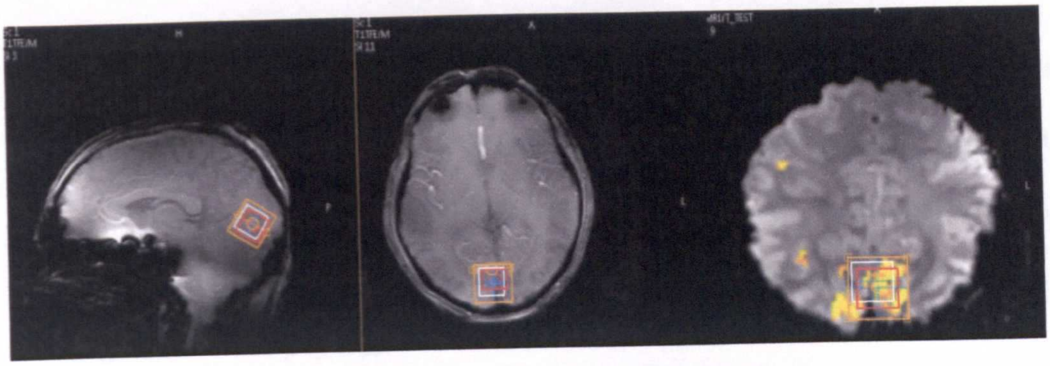

Figure 5.2: The right hand side image shows an activation map where a $8cm^3$ voxel was positioned inside the activated region of visual cortex for acquisition of the ^1H MR spectra. The two voxels shown in red and white are those from Glutamate and water respectively based on chemical shift calculations. The yellow box outside of the voxel shows the shim voxel. The images shown on the middle and left show the acquisition voxel overlaid on an anatomical image.

minute stimulation periods from 9 subjects (12 spectra per subject, resulting in 108 averaged spectra from 9 subjects) subtract that acquired during two 9.9-minute rest periods (108 averaged spectrum). An experimentally derived linebroadening of 0.5Hz was added to the group spectra acquired during stimulation duration, to compensate for BOLD changes in linewidth[125] .Appropriate white noise was added back to the spectra to keep signal to noise ratio constant. Subsequently, the resulting "BOLD free" difference spectrum was generated (Fig. 5.4.(D)).

5.3.5 Metabolite quantification using jMRUI QUEST

Averaged spectra for both rest and stimulation periods from each single subject were analyzed separately using Subtract-QUEST in jMRUI, with basis-sets simulated using NMR-SCOPE [126, 127]. Spin parameters were taken from Govindaraju *et al* [38]. 19 data points were omitted and the background signal was estimated from the first-points of the MRS signal using the Subtract-QUEST method. For each subject, the water signal was used as an internal reference and the levels of Lac, Glu, Gln as well as other brain metabolites were monitored and compared. A Wilcoxon signed rank test was conducted to compare the relative metabolite changes. Results were considered to be significant when $p \leq 0.05$.

5.3.6 Metabolite absolute quantification using LCModel

In vivo ^{1}H NMR spectra were analyzed using LCModel[128]. The LCModel analysis calculates the best fit to the experimental spectrum as a linear combination of model, solution spectra of brain metabolites. The following 20 simulated spectra were included in the basis dataset [2]: Alanine (Ala), Aspartate(Asp), Phosphorylcholine PCho, Creatine (Cr), Phosphocreatine (PCr), gamma-aminobutyric acid (GABA), Glutamine (Gln), Glutamate (Glu), glutathione (GSH), Glycine (Gly), myo-inositol (Ins), Lactate (Lac), N-acetylaspartate (NAA), scyllo-inositol (scyllo-Ins), Taurine (Tau), Ascorbate (Asc), Glucose (Glc), N-acetylaspartylglutamate (NAAG), Glycerophosphorylcholine (GPC) and Phosphorylethanolamine (PE). Spectra were simulated using previously published chemical shifts and coupling constants[129]. A macromolecule spectrum, experimentally measured from the human visual cortex using a metabolite nulling inversion-recovery sequence with TR=2000ms and TI=0.675secs[130]) was also included in the basis set (Fig. 5.3). Prior to insertion into the LCModel basis dataset, the residual signals from NAA and tCr were removed from the macromolecule spectrum using a HLSVD (Hankel Lanczos Sauares Singular Values Decomposition) filter [131] in jMRUI. LCModel analysis was performed on spectra within the chemical shift range 0.2-4.2ppm. The unsuppressed water signal measured from the same VOI was used as an internal reference for the quantification, assuming 80% brain water content. Spectra in each subject acquired during two 9.9-minute resting and two 9.9-minute stimulation periods were summed accordingly and then were quantified. Before metabolites quantification, 0.5Hz line broadening was added, to compensate for BOLD changes in linewidth[125] (appropriate white noise was added back to the spectra to keep signal to noise ratio constent). The absolute concentration values for every cerebral metabolite were rejected if the %SD from LCModel was greater than 20%. Those with %SD smaller than 20% were reported as mol per gram of wet tissue.

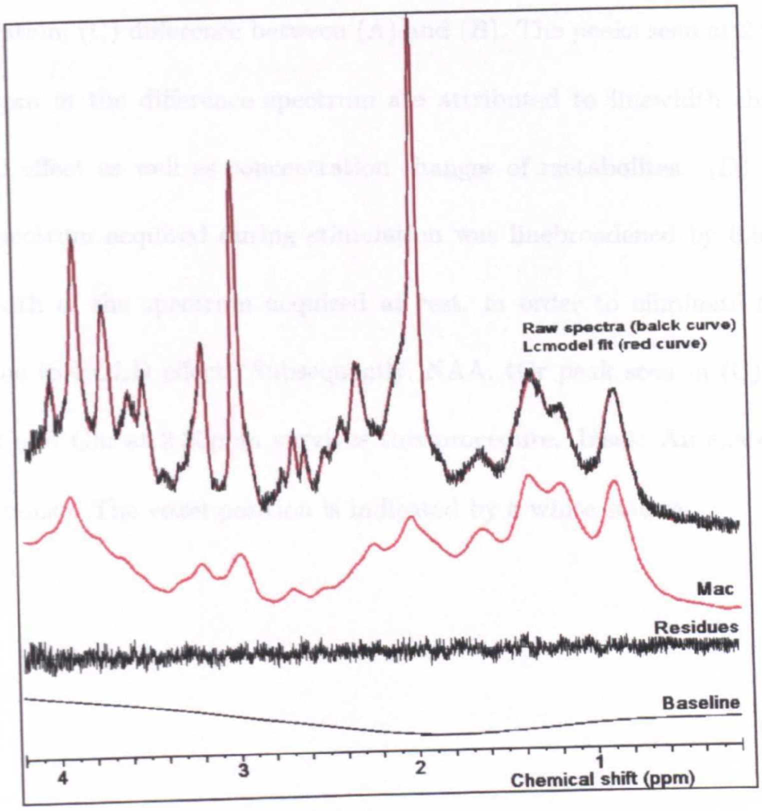

Figure 5.3: *In vivo* ^1H MR spectrum at 7T. From top to bottom: raw spectra data (black curve) and LCModel fit (red curve), macromolecule spectrum, residuals and baseline , at TE= 16 ms. The spectrum was acquired in a $2 \times 2 \times 2cm^3$ VOI in the visual cortex

5.4 Results

5.4.1 Spectral analysis

Fig. 5.4 shows a representative ^{1}H NMR spectrum and a difference spectrum obtained from the paradigm of double 9.9-minute stimulation, using data from 9 subjects (group analysis):(A) averaged spectrum acquired at rest; (B) averaged spectrum acquired during stimulation; (C) difference between (A) and (B). The peaks seen at 2.01, 2.10, 2.35 and 3.03ppm in the difference spectrum are attributed to linewidth changes due to the BOLD effect as well as concentration changes of metabolites. (D) same as (C), but the spectrum acquired during stimulation was linebroadened by 0.5Hz to match the linewidth of the spectrum acquired at rest, in order to eliminate the linewidth changes due to BOLD effect. Subsequently, NAA, tCr peak seen in (C) were largely minimized and Glu at 2.35ppm survives this procedure. Inset: An example acquired BOLD response. The voxel position is indicated by a white square.

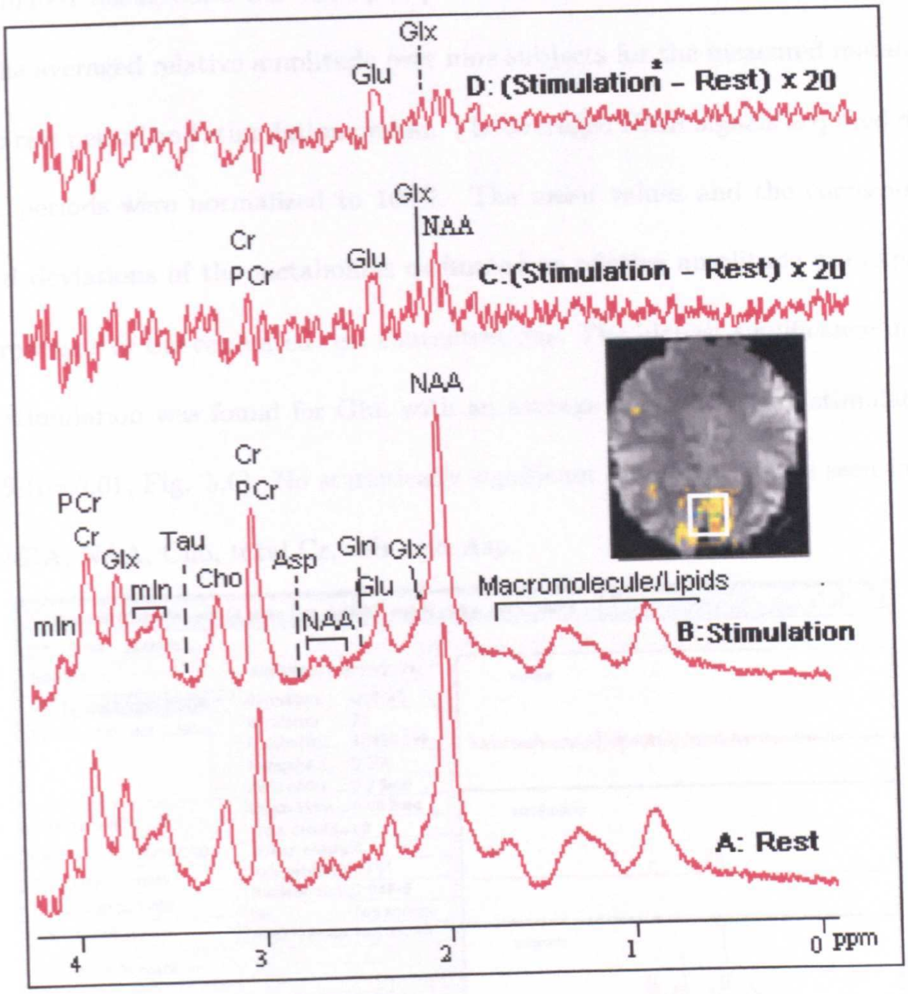

Figure 5.4: ^{1}H MRS spectra for the double stimulation paradigm using data from 9 subjects (group analysis) during (A) rest (two 9.9-min periods) and (B) stimulation (two 9.9-min periods). Difference spectrum before (C) and after compensation for the BOLD effect (D). The peaks ascribed to Glu (2.35ppm) is clearly evident in the compensated difference spectrum.

5.4.2 Quantitative analysis of metabolites using jMRUI QUEST

Fig. 5.5 presents the resulting fit from Subtract-QUEST in jMRUI. As can be seen, the estimated background fits the lipid peaks at 0.89 and 1.3 ppm well. Fig. 5.6 shows the averaged relative amplitude over nine subjects for the measured metabolites between rest period and stimulation period. The averaged NMR signals acquired during the rest periods were normalized to 100%. The mean values and the corresponding standard deviations of the metabolites estimated as relative amplitude are expressed as a percentage of the estimated rest concentrations. The highest significance increase during stimulation was found for Glu, with an average increase during stimulation of 6% ± 5%(p=0.01, Fig. 5.6). No statistically significant difference can be seen for Gln, Lac, GABA, NAA, Cho, total Cr, mIn and Asp.

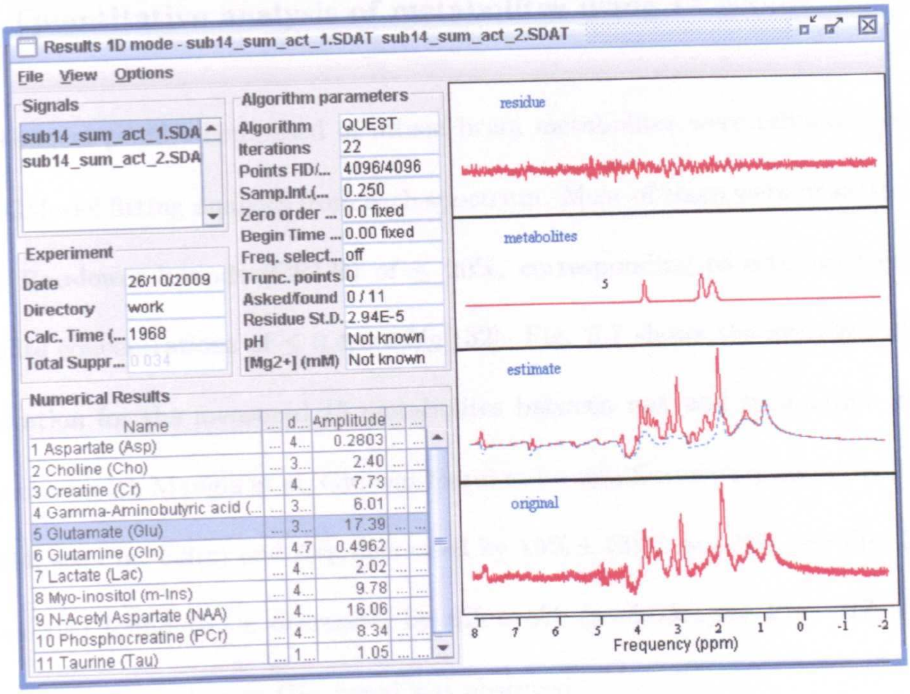

Experiment

Date 26/10/2009
Directory work
Calc. Time (... 1968
Total Suppr... 0.034

Algorithm parameters

Algorithm QUEST
Iterations 22
Points FID/... 4096/4096
Samp.Int.(... 0.250
Zero order ... 0.0 fixed
Begin Time ... 0.00 fixed
Freq. select... off
Trunc. points 0
Asked/found 0 / 11
Residue St.D. 2.94E-5
pH Not known
[Mg2+] (mM) Not known

Numerical Results

Name	...	d...	Amplitude	...	...
1 Aspartate (Asp)	...	4...	0.2803	...	...
2 Choline (Cho)	...	3...	2.40	...	...
3 Creatine (Cr)	...	4...	7.73	...	...
4 Gamma-Aminobutyric acid (...	...	3...	6.01	...	...
5 Glutamate (Glu)	...	3...	17.39	...	...
6 Glutamine (Gln)	...	4.7	0.4962	...	...
7 Lactate (Lac)	...	4...	2.02	...	...
8 Myo-inositol (m-Ins)	...	4...	9.78	...	...
9 N-Acetyl Aspartate (NAA)	...	4...	16.06	...	...
10 Phosphocreatine (PCr)	...	4...	8.34	...	...
11 Taurine (Tau)	...	1...	1.05	...	...

Figure 5.5: jMRUI QUEST Quantitation result window. From bottom to top, original spectrum; estimated spectrum and background (dashed line) using Sub-QUEST; selective Glutamate spectrum; and residue. As can be seen, the estimated background fits the lipid peaks at 0.89 and 1.3 ppm well.

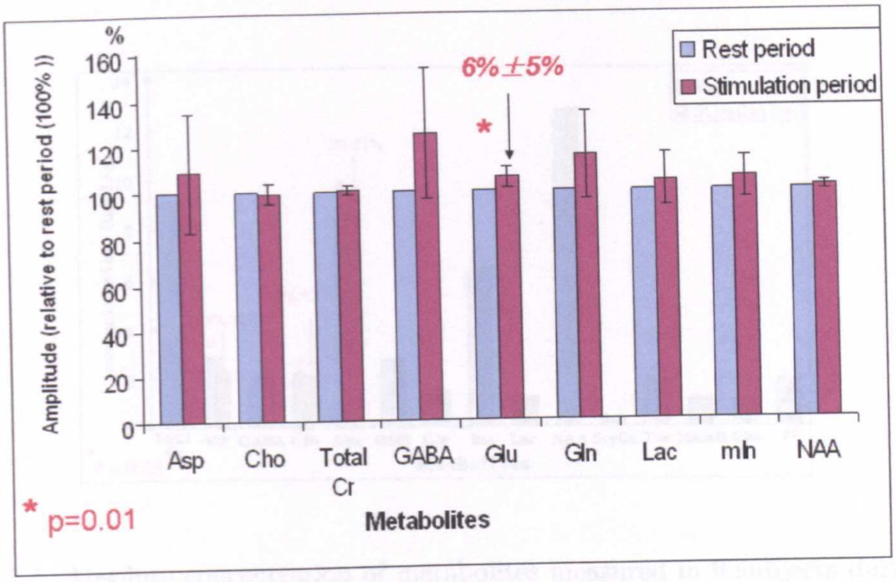

Figure 5.6: Averaged relative metabolite amplitudes over nine subjects between rest and stimulation measured by Sub-QUEST.

5.4.3 Quantitative analysis of metabolites using LCModel

Neurochemical profiles composed of fifteen brain metabolites were reliably quantified using LCModel fitting analysis from each spectrum. Most of them were quantified with Cramer Rao-lower bounds (CRLB) of $\leq 20\%$, corresponding to estimated errors in metabolite concentrations of $\leq 0.4\mu mol/g$[132]. Fig. 5.7 shows the averaged absolute concentration for the measured 15 metabolites between rest and stimulation periods. In agreement with Mangia et al, Glu was found to be significantly increased by $2\% \pm 1\%$ (p=0.044, see Fig. 5.8(c) and Asp decreased by $19\% \pm 13\%$(p=0.021, see Fig. 5.8(a)). Gln was also found to be decreased by $6\% \pm 3\%$ (p=0.038, see Fig. 5.8(b)). No significant change in Lac or Glc signal was observed.

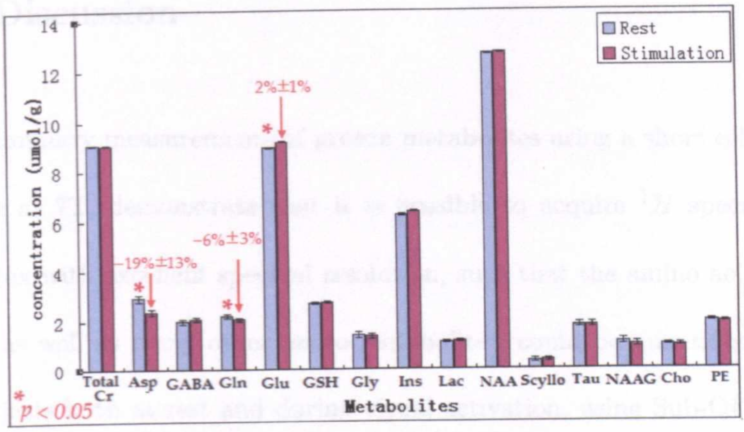

Figure 5.7: Absolute concentration of metabolites measured in 9 subjects during rest and stimulation periods using LCModel. Data are $mean \pm SD$ (N=9).

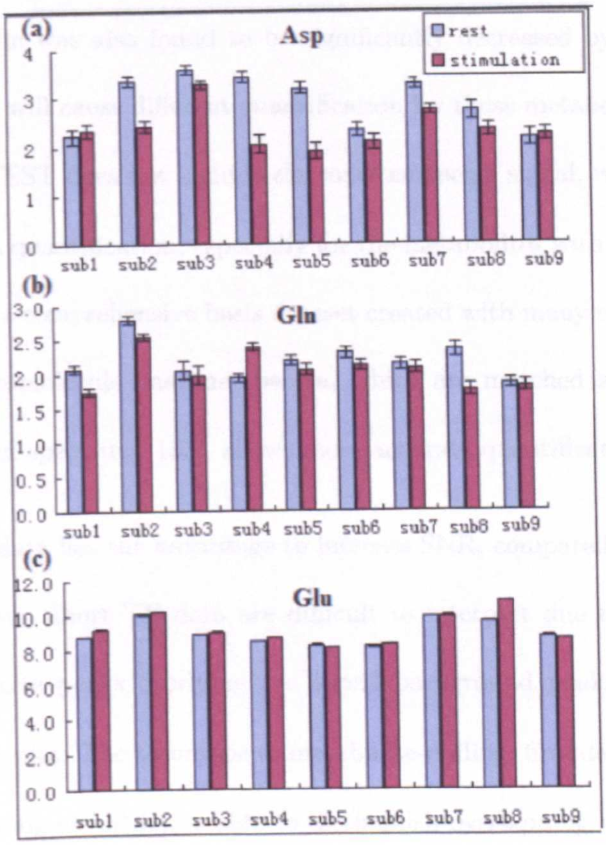

Figure 5.8: Absolute concentration of Asp (a), Gln (b) and Glu (c) for 9 subjects measured in rest and stimulation periods using LCModel. Data are $mean \pm SD$ (N=9).

5.5 Discussion

Our preliminary measurements of proton metabolites using a short echo time STEAM sequence at 7T, demonstrate that it is possible to acquire ^1H spectra from the visual cortex with excellent spectral resolution, such that the amino acids Glu, Gln and GABA, as well as many other neuro metabolites, could be quantified. Measurement in 9 subjects both at rest and during visual activation, using Sub-QUEST in jMRUI, indicates a significant increase in Glu by $6\% \pm 5\%$ during visual stimulation. However, using a LCModel basis dataset with 21 metabolites and macromolecule baseline, more metabolites with small concentrations can be observed. In agreement with Mangia *et al*, Glu was found to be significantly increased by $2\% \pm 1\%$ and Asp decreased by $19\% \pm 13\%$. Gln was also found to be significantly decreased by $6\% \pm 3\%$. A small phase variation will cause different quantification for those metabolites with small concentration. QUEST does not include the macromolecule signal, which might also bias the metabolites quantification, especially for the metabolites with lower concentration. LCModel with a comprehensive basis dataset created with many more metabolites and measured macromolecule baseline spectra, which are matched and scaled to fit the observed subject spectrum [133], allows more accurate quantification of metabolites.

Short TE data has the advantage to increase SNR, compared with long echo time studies. However, short TE data are difficult to interpret due to the multiplicity of narrow metabolite peaks overlying the broad background peaks arising from lipids and macromolecules. The technique of metabolite-nulling, first demonstrated in stroke patients by Hwang et al[134], is able to distinguish overlapping metabolites and lipid and macromolecule signals in short-echo $^1H - MRS$. The technique is based on the observation that lipids and macromolecule signals have short T_1 relaxation times (100-200 msec), metabolites have much longer T_1 relaxation times (1200-2000 msec). Using the inversion recovery technique (see Chapter 2.6.3)[135], metabolite-nulled spectra are obtained, which contained signals mainly from lipids and macromolecules with minimal contribution from the residual signals of NAA and Cr (which can be removed by HSLVD in jMRUI[131]). The difference between a standard short echo time spectrum and a metabolite-nulled spectrum yields a different spectrum composed of metabolites with the lipids and macromolecule resonance removed, thereby allowing the accurate quantitation of Glu and other metabolites.

Neurotransmitter cycling fluxes known as the Glu/GABA-Gln cycle[113], describes the release of neurotransmitter Glu or GABA from neurons and subsequent uptake into astrocytes. In return, astrocytes release Gln to be taken up into neurons for use as neurotransmitter precursor. Our observations of increased Glu with decreased Gln in the visual cortex during stimulation at 7T, uising LCModel, might indicate a stimulus driven increase in excitatory neurotransmitter cycling. Glu plus Gln did not change, further implying a shift in the Glu-Gln interconversion. We did not find any significant change in GABA during the stimulation. Possible reasons for this is that GABA concentrations are relatively low in the human brain and changes will be correspondingly small. Our findings of decreased Asp and increased Glu during repeated periods of visual stimulation are in good agreement with Mangia *et al.* [23] who interpreted them as an increase in the activity of the malate-aspartate shuttle (MAS), which plays an important role in maintaining the cytosolic redox potential $NADH/NAD^+$, required for the oxidative metabolism of Glc and for synthesis of brain neurotransmitters.

More detail discussions of these changed metabolites due to stimulation can be found in the following two chapters.

5.6 Conclusions

Taking advantage of the increased signal and spectral resolution at 7T and using a LCModel basis dataset with 21 metabolites at ultra-short TE, more metabolites with small concentrations can be observed. Measured increases in Glu with decreases in Gln indicate an increase in excitatory neurotransmitter cycling in the visual cortex during stimulation. The observed oppositive changes in decreased Asp and increased Glu support the hypothesis reported by Mangia [23] that sustained neuronal activation raises oxidative metabolism to a new steady state. No significant change in Lac or Glc signal was observed. This may be due to poor signal to noise for the low concentration metabolites, if changes are present they are certainly small (less than 0.2mol/g [23]).

Chapter 6

Investigating the metabolic changes due to visual stimulation using functional ^{1}H MRS at 7T: single and double stimulus paradigm

6.1 Introduction

Proton Magnetic Resonance Spectroscopy (^{1}H-MRS) is a powerful tool for investigating human metabolism *in vivo* and has been used to demonstrate metabolic changes in the visual cortex on visual stimulation[22, 7, 6, 120, 121, 23]. These previous studies focused mainly on Lac changes under a variety of experimental conditions and functional paradigms. However, the increased spectral resolution and SNR available at 7T enables improved discrimination between Glu, Gln and GABA and enables a large number of separate reliable quantification of brain metabolites[1, 130], thus providing a clearer understanding of metabolic changes due to visual stimulation. Mangia *et al.* used a checkerboard stimulus to investigate metabolic changes at 7T during two paradigms of visual stimulation lasting 5.3 and 10.6 minutes[23]: a new steady state of increased oxidative metabolism was observed, characterized by Lac increased by 23% ± 5%, Glu increased by 3% ± 1%, Asp decreased by 15% ± 6% and Glc concentration showed a tendency to decrease. The decrease in Glc is interpreted as driving an increased flux of Glc into the cell, the increase in Lac as reflecting an increase in Pyr and hence an increased flux into the TCA cycle. This is sustained by an increase in the activity of the malate aspartate shuttle (MAS), reflected in the increase in Glu and decrease in Asp concentrations as a consequence of the rate limiting Glu-Asp antiporter, characterized by the increased forward rate of reaction to Glu but decreased backward rate of reaction back to Asp, at the inner mitochondrial membrane [136]. This work has significantly improved our understanding of how brain energy metabolism underpins brain function.

Our initial feasibility study, used a LED goggles at 7T and a LCModel basis dataset with 21 metabolites(see Chapter 5), found increased Glu by 2%±1% and decreased Asp by 19%±13% during visual stimulation, which are consistent with previous reports and suggests stimulus driven increase in oxidative energy metabolism [23]. Interestingly, a decreased Gln by 6% ± 3% was also found under the activation. Our observation with increased Glu and decreased Gln might indicate an increase in excitatory neurotransmitter cycling in the visual cortex during stimulation. One reason for believing there could be is the knowledge that vesicular Glu released into the synaptic cleft is taken up by surrounding glial cells, converted to Gln and returned to neurons where it is converted back to Glu. The first MR observation of this Glu-Gln cycle was by

Badar-Gofer*et al.* [32] using ^{13}C labelled acetate in studies of superfused brain slices. Subsequently, ^{13}C labelled glucose studies in humans enabled the cycling rate to be accurately measured [33]. Measuring changes in this rate during visual stimulation has proven to be a challenge in humans[34]. However, in animal studies, it has been possible to demonstrate that almost all of this cycling is associated with neurotransmitter cycling [103]. A similar GABA-Glu-Gln cycle exists for the recycling of GABA. If recycling rates of Glu and or GABA are increased it is likely that there will be a relative change in the proportions of the neurotransmitters and of Gln, most probably an increase in the former and a decrease in the latter.

Given that the metabolite changes observed due to visual stimulation were relatively small. We therefore decided to use a more intense visual stimulus to try to elicit larger changes in the levels of Glc, Lac, Glu and Asp and to investigate the time course of post-stimulus recovery. We undertook two experiments. The first one consisted of 6.6 min baseline followed by 13.2 min of visual stimulation and 19.8 min recovery, to confirm and quantify the changes in the levels of Glc, Lac, Glu and Asp and to further investigate GABA and Gln in response to functional visual stimulation as well as to observe post-stimulus recovery. The second one involved two 9.9 min rest periods interleaved with two 9.9 min stimulation periods, in order to investigate whether the response to further periods of stimulation are identical or differ from the initial response. In doing so, we hope to establish a clear picture of brain metabolism and neurotransmitter activity during neuronal activation.

6.2 Aim

To confirm and quantify the changes in the levels of Glc, Lac, Glu and Asp and to further investigate GABA and Gln in response to functional visual stimulation as well as to observe post-stimulus recovery.

6.3 Materials and methods

6.3.1 Human subjects

Ten healthy subjects (7M, 3F, $age = 25 \pm 3$) without history of neurological disorders participated in this study which was conducted over a three month period. Nine subjects were involved in each of the two functional paradigms (8 subjects participated in both). Informed consent was obtained before MR examination according to procedures approved by the University of Nottingham Medical School Ethics Committee.

6.3.2 Visual stimulation

The visual stimulus was projected onto a screen using a LED projector, coupled to a PC, and was viewed with prism spectacles. A small cross in the centre of the field of view was used as fixation point. A median grey background was presented during rest periods and the stimulation paradigm comprised of contrast-defined wedges, moving towards or away from the fixation cross and randomized by the computer (see Fig6.1). This stimulation paradigm has been shown to lead to less neural adaptation over time compared to a checkerboard [137].

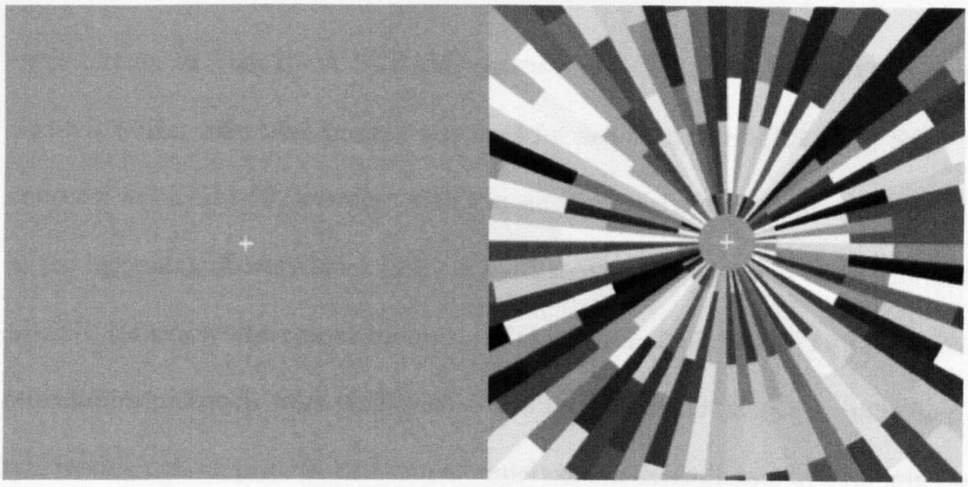

Figure 6.1: Stimuli used in the fMRI scanning. In the rest period, a cross appeared at the centre of the grey background. In the stimulus condition, a moving full-scree flickering contrast-defined wedges randomized by the computer was presented.

6.3.3 Magnetic resonance imaging and spectroscopy

All MR measurements were acquired using a Philips Achieva 7T MR system with reception employing a 16-channel SENSE head coil and transmission on a surrounding volume coil. First and second order shim terms were automatically adjusted using FASTMAP with EPI readout[138]. Head movement was minimized by positioning two pieces of foam surrounding the subjects head.

fMRI measurement: An initial fMRI scan (EPI, TE=26ms, TR=2200ms, spatial resolution=$2mm^3$ isotropic voxels, functional paradigm: 4.4s stimulation and 28.6s rest, 8 repeats) was performed prior to spectroscopic acquisition, in order to determine the region of maximum activation in the visual cortex. fMRI data were analysed in real-time using IViewBOLD on the Philips system, in order to determine the region of maximum activation in the visual cortex.

MRS Measurement: A cubic VOI of $2 \times 2 \times 2cm^3$ was positioned inside the region exhibiting significant BOLD change on stimulation for functional MRS acquisition (see inset picture in Fig6.2). A STEAM sequence (TE/TM/TR=15/17/3000ms, spectral width 4000Hz, 4096 time points) was used for acquiring the MRS data. Spectra were collected in blocks of 32 averages with 1 acquisition without water suppression acquired at the beginning of every block (99s per block). Water suppression was performed using MOIST (Multiply Optimized Insensitive Suppression Train)[139]. Two different visual stimulation protocols were employed. The first functional paradigm comprised a 6.6-min resting period, prior to 13.2-min of visual stimulation followed by 19.8-min recovery, according to an acquisition protocol: OFF (4 blocks)-ON(8 blocks)-OFF(12 blocks). The second functional paradigm consisted of two 9.9-min rest periods interleaved with two 9.9-min stimulation periods, according to an acquisition protocol: OFF(6 blocks)-ON(6 blocks)-OFF(6 blocks)-ON(6 blocks). The total duration for each functional session was 39.6 minutes.

MRI measurement: A 3D T1-weighted MPRAGE image was acquired (Field of View $(FOV) = 192 \times 192 \times 52.5mm^3$ with 1.5mm isotropic voxels, TE/TI/TR =1.5/965/14ms) to allow the tissue content of the MRS voxel to be calculated. The anatomical image was first masked to show only image voxels contained within the MRS voxel. The tissue content was then assessed by segmenting the MRS voxel based on the image intensity (threshold, manually chosen by an observer, set to the upper threshold for CSF tissue).

6.3.4 Post-processing

Spectra were saved separately and were frequency aligned to the NAA peak at 2.02ppm using an inhouse built program in MATLAB [http://www.mathworks.com] before phase correction in jMRUI [http://www.mrui.uab.es/muri/]. Spectra were then averaged into groups for further analysis in LCModel. For the single visual stimulation paradigm, spectra from each subject acquired during 6.6-min rest (4 blocks), 13.2-min stimulation (8 blocks) and 19.8-minutes recovery (12 blocks) were averaged across each of the conditions. In addition, spectra were averaged into groups of 4 blocks for each subject. For the double stimulation paradigm, all stimulation spectra were averaged as were all rest spectra for each subject. In addition, spectra were also averaged across the individual rest and stimulation periods for each subject. Finally, time courses of metabolites for both functional paradigms were achieved separately by quantifying every spectrum (time resolution of 99s) for each subject, and averaged inter-subject trajectories of metabolites were calculated from all 9 subjects. A group difference spectrum was generated from the double visual stimulation paradigm using spectra from 8 subjects (one subject was excluded due to the noise within the chemical shift range 3.0-4.0 ppm). The group averaged stimulation spectrum (12 spectral blocks per subject, 96 spectral blocks in total) was subtracted from the group averaged rest period spectrum. 0.5Hz Lorentzian line broadening was added to the group spectrum in order to compensate for Blood Oxygen Level Dependent (BOLD) changes in linewidth [125]. Appropriate white noise was added back to the spectra to keep signal to noise ratio constant. This resulted in a "BOLD free" difference spectrum.

6.3.5 Metabolite quantification

LCModel was used to do metabolites quantification (detail information about LCModel basis dataset can be found in Chapter 5.3.6). For both functional paradigms, the averaged spectrum for each subject was quantified separately using LCModel. Time courses of metabolites for both functional paradigms were achieved separately by quantifying every spectrum (time resolution of 99s) for each subject, and averaged inter-subject trajectories of metabolites were calculated from all 9 subjects. They were rejected if the

%SD from LCModel was greater than 20% (Glc was quantified with %$SD \leq 30\%$). The unsuppressed water signal, was used as an internal reference for metabolite quantification. The absolute concentration values for every cerebral metabolite were determined as μ mol per gram of wet tissue, assuming a brain water content of 80%. Measured concentrations for all metabolites, excluding Lac [140], Glc [141], Gln [140] and GSH [142] which exist in significant concentrations in the cerebrospinal fluid (CSF), were corrected for the VOI tissue fraction, with the MPRAGE anatomical image .

6.3.6 Statistical analysis

A Wilcoxon signed rank test was conducted to compare the metabolites changes during different time scales of stimulation versus resting periods for both functional paradigms. Values are presented as $mean \pm SD$ and $p \leq 0.05$ is considered as statistically significant.

6.4 Results

6.4.1 Spectral analysis

Fig. 6.2 shows a representative in vivo ^{1}H NMR spectra, obtained from the single visual stimulation paradigm during a 6.6-min resting period (Fig. 6.2(A)) and 13.2-min of visual stimulation (Fig. 6.2(B)) for a single subject. Spectral quality (resolution and SNR) was highly reproducible between subjects and functional sessions. Small, narrow peaks (line width around 5Hz) at the positions of the strong singlet resonances of NAA (2.01ppm) and tCr (3.0ppm) were visible in the difference spectra (Fig6.2(C)), which were attributed to the linewidth changes due to the BOLD effect[125]. BOLD effect on the height of the total Cr signal at 3.03ppm was persistent, increased by approximately $\sim$ 3%, during the whole functional paradigm periods (see Fig. 6.3).

This confirmed that the VOIs were positioned in the activated visual cortex during the experimental session. Following Lorentzian linebroadening (0.5Hz), the residual signal of NAA and tCr in the difference spectrum is largely eliminated (Fig. 6.2(D)). The localization performance of the sequence and efficient MOIST water suppression resulted in spectra with minimal distortion and a flat baseline over the entire chemical shift range. In particular, contamination by signals from extracellular lipids was not detectable at 1.5 ppm. The flat residual obtained on subtracting summed averaged spectra during stimulation and rest conditions verified the high stability of the system and reproducibility of the measures within each experimental session.

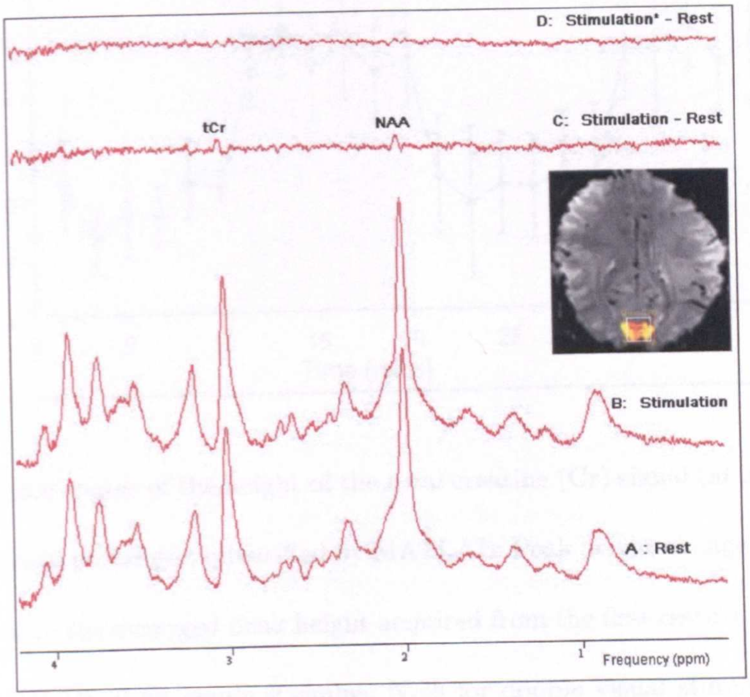

Figure 6.2: Representative 7T ^1H MRS spectrum acquired during 6.6-min resting (A) and 13.2-min stimulation periods (B) from a single subject. Difference spectra between (A) and (B). Inset picture: representative example of BOLD response with the voxel position for MRS indicated by a white square (the yellow box shows the shim volume).

Fig. 6.4 depicts the group difference spectrum between stimulation (Fig. 6.4(ii)) and resting periods (Fig. 6.4(i)), obtained from the double 9.9-min stimulation paradigm

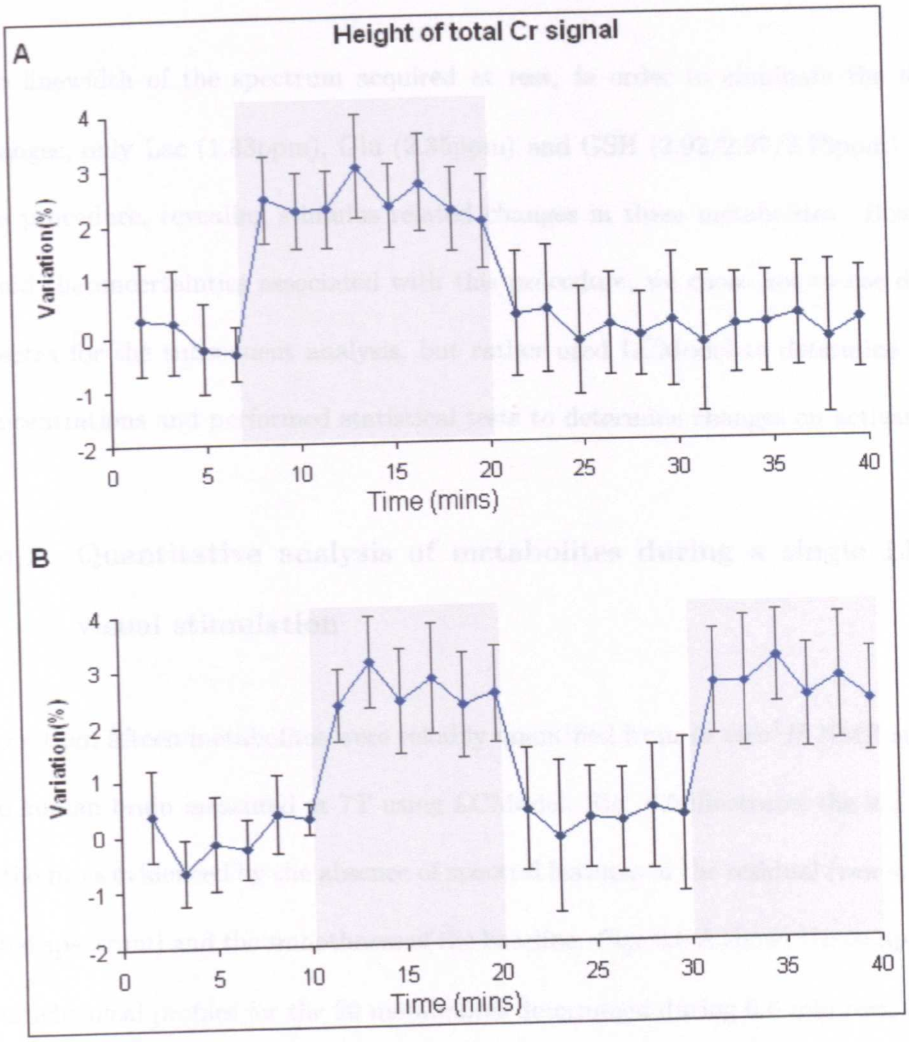

Figure 6.3: Time course of the height of the total creatine (Cr) signal (at 3.03ppm) during the functional paradigm, quantified by MATLAB. Peak height change are expressed as a % relative to the averaged peak height acquired from the first resting periods. Data are *mean* ± *SD* (N=9 for single stimulus; N=8 for double visual stimulus), temporal resolution is 99s. The shaded areas show the periods of visual stimulation.

using data from 8 subjects (group analysis). The peaks seen at 1.33ppm (Lac), 2.01ppm (NAA), 2.35ppm (Glu), 2.92 and 2.97ppm (GSH), 3.03ppm (tCr), 3.18ppm (Cho), 3.78ppm(GSH) in the difference spectrum (Fig. 6.4 C) are attributed to linewidth changes due to the BOLD effect as well as concentration changes of metabolites[23]. When the spectrum acquired during stimulation was linebroadened by 0.5Hz to match the linewidth of the spectrum acquired at rest, in order to eliminate the linewidth changes, only Lac (1.33ppm), Glu (2.35ppm) and GSH (2.92/2.97/3.78ppm) survived the procedure, revealing stimulus related changes in these metabolites. However, to avoid the uncertainties associated with this procedure, we chose not to use difference spectra for the subsequent analysis, but rather used LCModel to determine absolute concentrations and performed statistical tests to determine changes on activation.

6.4.2 Quantitative analysis of metabolites during a single 13.2-min visual stimulation

More than fifteen metabolites were reliably quantified from *in vivo*^1H NMR spectra of the human brain measured at 7T using LCModel. Fig. 6.5 illustrates the high quality of the fit as evidenced by the absence of spectral features in the residual (raw spectrum-fitted spectrum) and the smoothness of the baseline. Fig. 6.6 A shows the comparison of neurochemical profiles for the 20 metabolites determined during 6.6-min rest, 13.2-min stimulation and 19.8-min recovery periods ($mean \pm SD$, N=9). The significant changes are summarised in Table. 6.1. In good agreement with previously published results at 7T [23], during stimulation Glu was found to be increased by 2%±1% (equivalent to 0.22 $\mu mol/g$, p=0.011), Asp decreased by 9%±8% (equivalent to 0.32 $\mu mol/g$, p=0.038), Lac increased by 10%±6% (equivalent to 0.1 $\mu mol/g$, p=0.044), and Glc showed a tendency to decrease by 22% ± 18% (equivalent to 0.40 μ mol/g) but did not reach statistical significance because of the higher SD for this metabolite. Separating the 13.2-min stimulation into two 6.6-min blocks, allows further insight into the time course of these changes. It can be seen that the elevation in Lac ($26\% \pm 7\%$, approximately $0.2 \mu mol/g$, p=0.038), is only evident during the first 6.6-min of activation, with a tendency to return towards baseline thereafter, despite the ongoing visual stimulation (Fig. 6.6B).

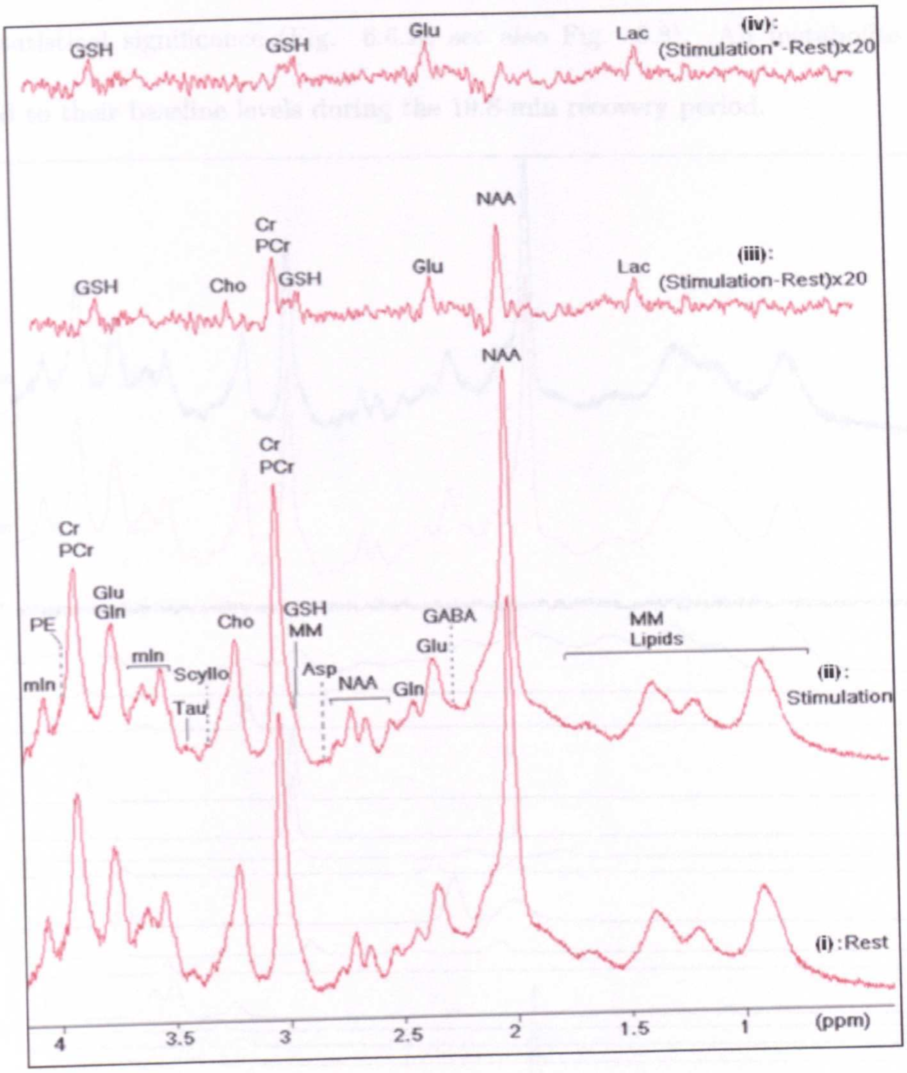

Figure 6.4: ^{1}H MRS spectra for the double stimulation paradigm using data from 8 subjects (group analysis) during (i) rest (two 9.9-min periods) and (ii) stimulation (two 9.9-min periods). Difference spectrum before (iii) and after compensation for the BOLD effect (iv). Peaks ascribed to Lac (1.33ppm), Glu (2.35ppm) and GSH (2.92/2.97/3.78ppm) are clearly evident in the compensated difference spectrum.

Interestingly, during the 13.2-min of visual stimulation, the brain GSH concentration was found to be elevated by $7\% \pm 4\%$ (equivalent to 0.17 $\mu mol/g$, p=0.021), in parallel with decreased brain Gln and Gly, by $8\% \pm 5\%$ (equivalent to 0.18 $\mu mol/g$, p=0.038) and $11\% \pm 6\%$ (equivalent to 0.20$\mu mol/g$, p=0.015), respectively. GABA exhibited a tendency to increase throughout the period of stimulation, but the increase did not reach statistical significance (Fig. 6.6.A, see also Fig. 6.8). All metabolite levels returned to their baseline levels during the 19.8-min recovery period.

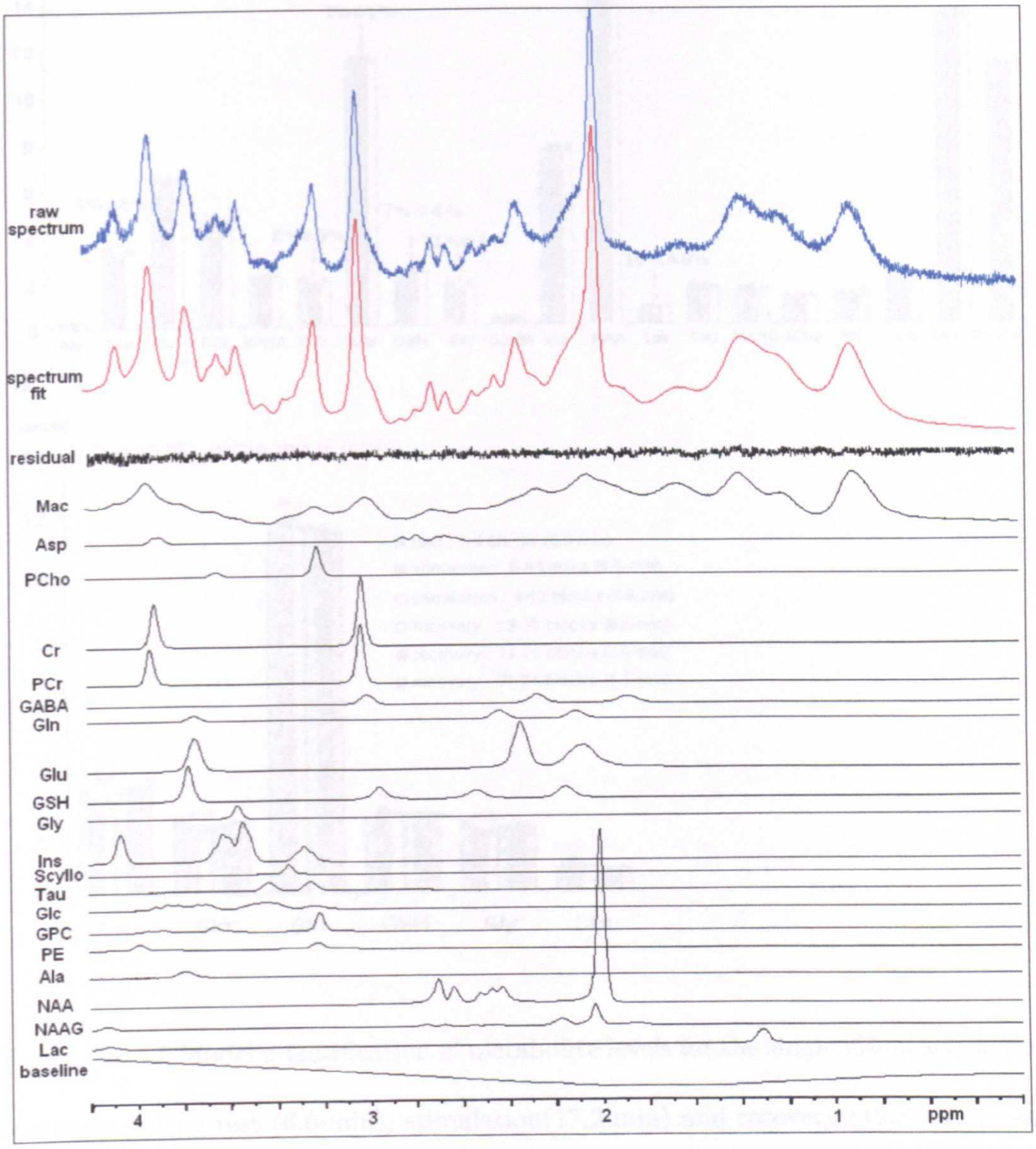

Figure 6.5: ^1H 7T MRS spectrum (STEAM sequence: TE/TM/TR=15/17/3000ms, BW 4000Hz, 4096 points, NSA 32) obtained from a $2 \times 2 \times 2cm^3$ volume in the visual cortex (uppermost spectrum), LCModel fit (second spectrum from top) in the range 0.2 to 4.2 ppm and residual (third spectrum from top). The LCModel basis components, macromolecule and baseline contributions to the fit are shown in the lower traces.

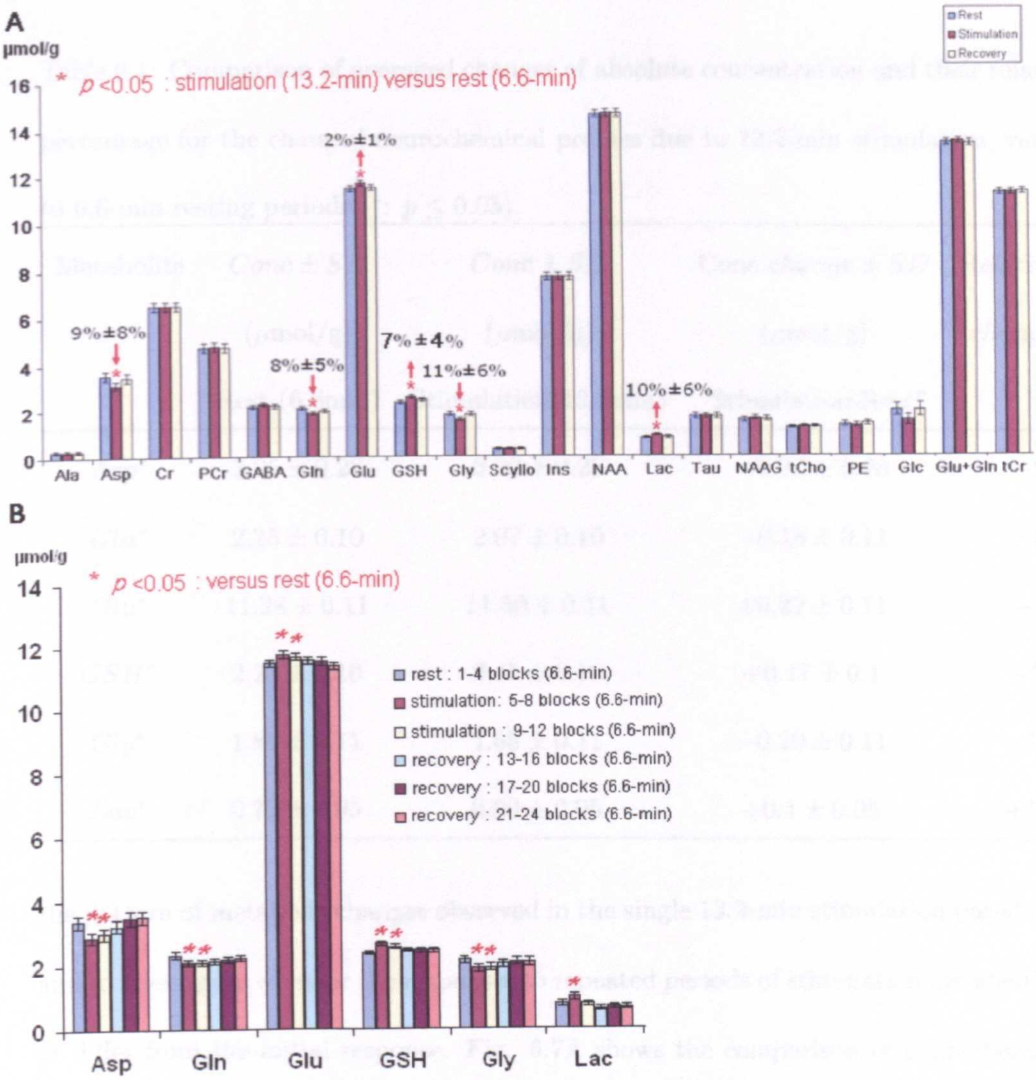

Figure 6.6: LCModel quantification of metabolite levels for the single visual stimulation paradigm during rest (6.6-min), stimulation(13.2-min) and recovery (19.8-min). Data are shown for metabolites for which the CRLB is less than 20% (Glc was quantified with $CRLB < 30\%$) and are $mean \pm SD$ (N=9). B. For the metabolites showing significant change on stimulation the data have been further analyzed in blocks of 6.6 min duration: rest, stimulation, recovery, 1, 2 and 3 blocks, respectively.

6.4.3 Quantitative analysis of metabolites during repeated 9.9-min visual stimulations

The second experimental paradigm involved two periods of rest (each of 9.9-min duration) interleaved with two 9.9-min stimulation periods. It was undertaken to confirm

Table 6.1: Comparison of averaged changes of absolute concentration and their relative percentage for the changed neurochemical profiles due to 13.2-min stimulation, versus to 6.6-min resting periods (*: $p \leq 0.05$).

Metabolite	$Conc \pm SD$ (μmol/g) Rest (6.6min)	$Conc \pm SD$ (μmol/g) Stimulation(13.2min)	Conc $change \pm SD$ (μmol/g) "Stimulation-Rest"	Relative percentage $change \pm SD$ (%)
*Asp**	3.25 ± 0.28	3.20 ± 0.28	−0.32 ± 0.28	−9% ± 8%
*Gln**	2.25 ± 0.10	2.07 ± 0.10	−0.18 ± 0.11	−8% ± 5%
*Glu**	11.28 ± 0.11	11.50 ± 0.11	+0.22 ± 0.11	+2% ± 1%
*GSH**	2.28 ± 0.10	2.45 ± 0.10	+0.17 ± 0.1	+7% ± 4%
*Gly**	1.85 ± 0.11	1.65 ± 0.11	−0.20 ± 0.11	−11% ± 6%
*Lac**	0.79 ± 0.05	0.89 ± 0.05	+0.1 ± 0.05	+10% ± 6%

the pattern of metabolic changes observed in the single 13.2-min stimulation paradigm, and to investigate whether the responses to repeated periods of stimulation are identical or differ from the initial response. Fig. 6.7A shows the comparison of neurochemical profiles for the 20 metabolites measured (*mean* ± *SD*, N=8). The significant changes are summarised in Table. 6.2. In good agreement with our previous findings from the single stimulation, significant stimulation related changes were found in Glu (increased by 3%±1% (p=0.021)), Asp (decreased by 10%±7% (p=0.044)), Lac (increased by 9% ± 7% (p=0.015)), GSH (increased by 8% ± 2% (p=0.011)), Gln (decreased by 6% ± 4% (p=0.044)) and Gly (decreased by 12% ± 6% (p=0.038)). Again, Glc exhibited a tendency to decrease (by 30% ± 19%) and GABA showed a slight increase during stimulation but neither effect reached significance.

Changes in Asp, Glu, Gln, GSH and Gly during the second 9.9-min stimulation period were comparable to those found during the first 9.9-min stimulation period (Fig.

6.7B). However, Lac only showed significant elevation in the first 9.9-min stimulation (30% ± 7%, equivalent to 0.21mol/g) with no significant accumulation evident in the second 9.9-min stimulation (Table. 6.2). In addition, Glu and GSH showed a significantly enhanced increase in the second stimulation period, by 1% ± 1% (equivalent to 0.15 mol/g, p=0.021) and 3% ± 2% (equivalent to 0.1 μ mol/g, p=0.011), respectively. A possible reason for the increased elevation in Glu and GSH in the second phase of activation might be their slow recovery rate, such that their levels hadn't returned to baseline during the second 9.9-min resting period. In support of this, we find significant elevation of Glu (by 1% ± 1% equivalent to 0.12 μ mol/g, (p=0.021)) and GSH (by 5% ± 3% equivalent to 0.15 mol/g, (p=0.038)), in the second compared to the first resting period.

Table 6.2: Changes of averaged absolute concentration and relative percentage of changed metabolites in the first and second 9.9-min stimulation periods, versus to the initial 9.9-mins resting periods. (*: $p \leq 0.05$).

Metabolite	First 9.9-min stim		Second 9.9-min stim	
	changes ± *SD* μmol/g	*changes* ± *SD* (%)	*changes* ± *SD* μmol/g	*changes* ± *SD* (%)
Asp^*	−0.4 ± 0.23	−12% ± 7%	−0.33 ± 0.26	−9% ± 7%
Gln^*	−0.21 ± 0.10	−8% ± 4%	−0.29 ± 0.10	−11% ± 4%
Glu^*	+0.20 ± 0.10	+2% ± 1%	+0.35 ± 0.10	+3% ± 1%
GSH^*	+0.26 ± 0.07	+7% ± 2%	+0.36 ± 0.07	+10% ± 2%
Gly^*	−0.23 ± 0.14	+11% ± 6%	−0.32 ± 0.14	−15% ± 6%
Lac^*	+0.21 ± 0.05	+30% ± 7%	-	-

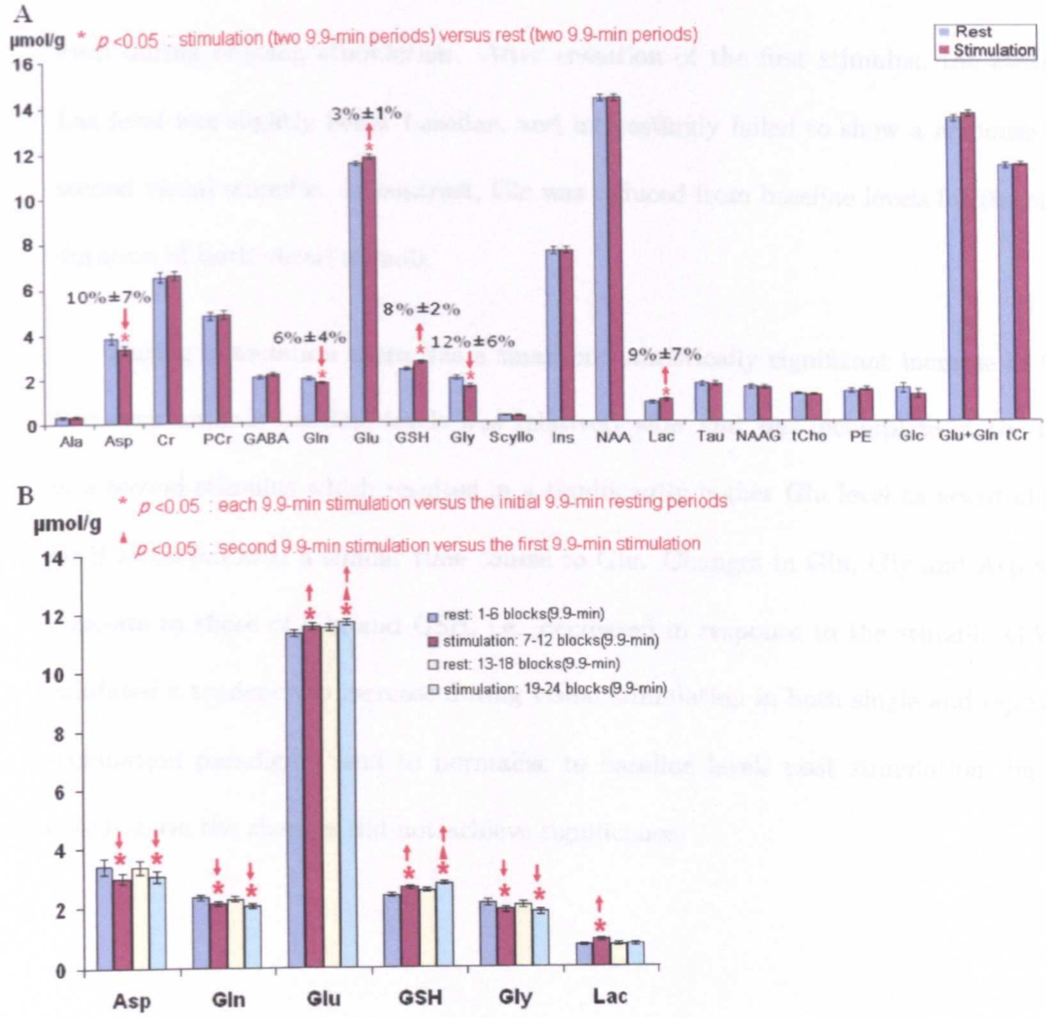

Figure 6.7: LCModel quantification of metabolite levels for the repeated (double) visual stimulation paradigm, comparing rest (two 9.9-min periods) and stimulation (two 9.9-min periods). Data are shown for metabolites for which the CRLB is less than 20% (Glc was quantified with $CRLB < 30\%$) and are $mean \pm SD$ (N=8). B. Data for individual rest and stimulation blocks for metabolites demonstrating significant change on activation.

6.4.4 Metabolic time courses

Metabolic time courses with a 99s time resolution are shown for the single and repeated visual stimulation paradigms in Fig. 6.8. They reveal that Lac increases to a maximum level within the first 99s of activation, followed by a decrease towards the basal level even during ongoing stimulation. After cessation of the first stimulus, the averaged Lac level was slightly below baseline, and interestingly failed to show a response to a second visual stimulus. In contrast, Glc was reduced from baseline levels for the entire duration of both visual stimuli.

During stimulation there was a small but statistically significant increase in Glu. Recovery towards baseline levels was relatively slow and was incomplete at the time of a second stimulus which resulted in a significantly higher Glu level as noted above. GSH levels followed a similar time course to Glu. Changes in Gln, Gly and Asp were opposite to those of Glu and GSH, i.e. decreased in response to the stimuli. GABA exhibited a tendency to increase during visual stimulation in both single and repeated stimulation paradigms, and to normalize to baseline levels post stimulation, but as noted above the changes did not achieve significance.

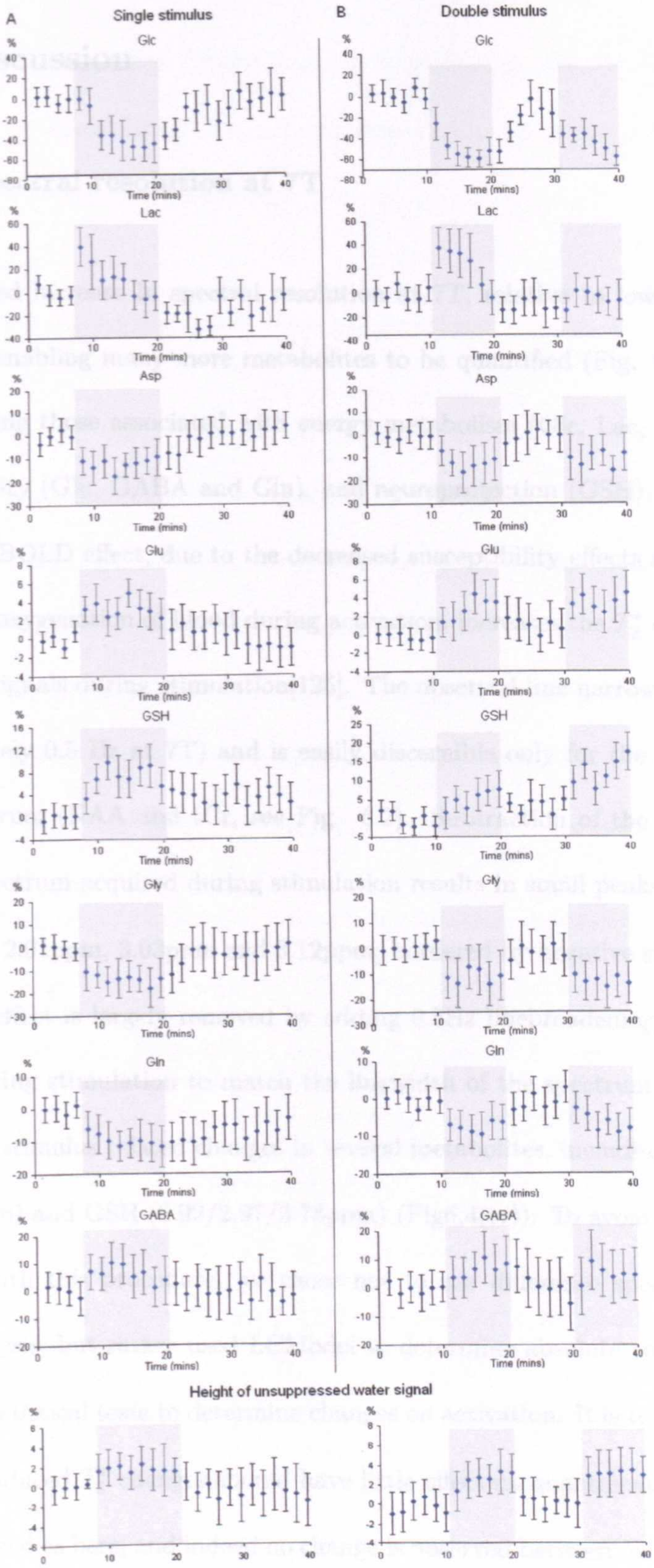

Figure 6.8: Time courses of metabolites and BOLD effect on the water peak height during the single (A) and double (B) visual stimulation paradigms. Changes are expressed as a % relative to the averaged level acquired from the first resting periods. Data are *mean* ± *SD* (N=9 for single stimulus; N=8 for double visual stimulus), temporal resolution is 99s. The shaded areas show the periods of visual stimulation.

6.5 Discussion

6.5.1 Spectral resolution at 7T

The expected increase in spectral resolution at 7T, relative to lower field strengths, is realised, enabling many more metabolites to be quantified (Fig. 6.6, Fig. 6.7, Fig. 6.8), including those associated with energy metabolism (Glc, Lac, Asp), neurotransmitter activity (Glu, GABA and Gln), and neuroprotection (GSH). As previously reported, the BOLD effect, due to the decreased susceptibility effects resulting from the local hyper-oxygenation of blood during activation, increases the T_2^* of both water and metabolite signals during stimulation[125]. The observed line narrowing effect is small (approximately 0.5 Hz at 7T) and is easily discernible only for the strongest singlets in the spectrum (NAA and tCr, see Fig. 6.2). Subtraction of the resting spectrum from the spectrum acquired during stimulation results in small peaks in the difference spectrum at 2.01ppm, 3.03ppm and 3.12ppm, bordered by negative sidelobes (Fig. 6.4 (iii)). This effect is largely removed by adding 0.5Hz linebroadening to the spectrum acquired during stimulation to match the linewidth of the spectrum acquired at rest. This reveals stimulus related changes in several metabolites, including Lac (1.33ppm), Glu (2.35ppm) and GSH (2.92/2.97/3.78ppm) (Fig6.4(iv)). To avoid the uncertainties associated with this procedure, we chose not to use difference spectra for the subsequent analysis, but rather used LCModel to determine absolute concentrations and performed statistical tests to determine changes on activation. It is to be expected that the BOLD-induced T_2^* changes should have little effect on quantification if a short TE sequence is used as here, and indeed no change is observed between rest and stimulation for NAA (Fig. 6.6, Fig. 6.7), lending confidence to this assertion. It also suggests that the TR we have chosen (3s) is sufficiently long for any stimulation induced changes in

T_1 values to be negligible. There is one proviso, namely that if stimulation leads to movement of metabolites between compartments with substantially different relaxation behaviours this may not be the case.

6.5.2 Stimulation induced changes in brain energy metabolism

The brain's energy requirement is met primarily by Glc, delivered from plasma via the Glc transporter (Fig. 6.9). Reversibility of this Glc transporter[143] suggests that the increased Glc flux, required to meet the increased energy demand during visual stimulation, can be achieved by a decrease in brain Glc concentration, slowing down reverse transport until a new steady state is reached, in which net Glc influx is equal to CMR_{glc}[23]. In our experiments, basal Glc levels in the visual cortex ($1.9 \pm 0.35 \mu mol/g$) were reduced by approx 32% ± 8% throughout the stimulation periods.

Although the trends in the Glc time courses are clear, the changes did not reach statistical significance. This is a result of a higher SD associated with the Glc quantitation, probably because more than 80% of the signal intensity of glucose is in the $3.2 \sim 3.9$ ppm spectral region [144], where there is overlap with the much stronger resonances of Glu, Gln, myo-inositol (mIn), and taurine (Tau). The observed decrease in Glc under stimulation in our experiments is in good agreement with previous reports[23], leading weight to the idea that decreased tissue Glc does indeed reflect increased CMR_{glc} during visual stimulation.

Several ^{1}H MRS studies have reported elevated brain lactate during visual stimulation and we too observe increases above baseline of up to 0.2mol/g (26% ± 7%) in the early stage of approximate 1.67 minutes stimulation (Fig. 6.6.B, Fig. 6.7.B and Fig. 6.8). In contrast to the studies by Mangia *et al*, which showed a transient decrease in lactate over the first 5s following a short (1s) visual stimulus [20], and an increase to a new steady state during a longer stimulus [23], comparable in duration to ours, we observed a transient increase, with a subsequent return towards baseline (Fig. 6.8). This is consistent with the first report of Lac increase during sustained visual stimulation [17], later confirmed by Frahm et al [6]. However, the feasibility of measuring Lac changes under stimulation has been challenged by other authors: Merboldt *et.al* [7] could not detect any Lac accumulation during several kinds of visual stimulation; Boucard *et. al* [19] failed to detect the Lac signal during visual stimulation. The reasons for these differences in Lac response, measured by ^1HMRS, is unclear. It is possible that the transient responses reflect adaptation or a decrease in attention. However, we specifically chose a visual stimulus designed to minimise these effects [137]. It is also possible that different acquisition sequences or experimental protocol have different sensitivities to possible changes in relaxation times associated with changes in intracellular milieu or movement between compartments. Again, we chose an acquisition sequence to try to minimise these effects (see above).

The initial increase in Lac during the early stimulation period most probably reflects an increase in anaerobic glycolysis. It also implies an increase in pyruvate (Pyr) (because of the dynamic equilibrium between the Lac and Pyr mediated by Lac dehydrogenase (LDH see Fig. 6.9 and Fig. 6.10)). This rise in Pyr has been suggested to stimulate activation of pyruvate dehydrogenase (PDH), leading to an increased flux into the oxidative pathway [145]. Mangia et al[23] argue that a new steady state of increase Lac sustains this increased flux into the TCA cycle. However, it could also be argued that an increased flux through PDH could lead to a decrease in Lac as we observe. Because of the permeability of the blood-brain barrier (BBB) to Lac, the increased brain Lac concentration during stimulation could also lead to an increased Lac efflux to blood, accounting for the decreased brain Lac level we observe in the later stages of the visual stimulation. Lac export to the extracellular compartment is believed to occur approximately 30 secs to 1 min after the start of stimulation [146]. The observed peak in brain Lac then represents a balance between production and efflux which is likely to depend strongly on the nature of the stimulation paradigm. It is possible that the changes in Lac we observe reflect changes in its utilisation as energy substrate by neurons as suggested by several authors [11]. However, as noted by Mangia *et al*[23], modelling of this lactate shuttle hypothesis suggests that activation should result in a sustained increase in lactate, rather than a transient increase as noted above [147]. It is also possible, though unlikely in our case, that the changes we see reflect movement of Lac between compartments with radically different relaxation times.

Of great interest is the lack of Lac response to a second period of visual stimulation (Fig.6.8), suggesting that processes switched on during the first period of visual stimulation, remain active or "primed" during the ensuing rest period. This observation is reminiscent of previously reported ischaemic preconditioning effects [148] and merits further investigation regarding its origin and longevity. This is the subject of further studies in our laboratory.

Our findings of decreased Asp and increased Glu during single and repeated periods of visual stimulation are in good agreement with (Mangia et al. 2007a) who interpreted them as an increase in the activity of the malate-aspartate shuttle (MAS) (Fig.6.9), which plays an important role in maintaining the cytosolic redox potential $NADH/NAD^+$, required for the oxidative metabolism of Glc and for synthesis of brain neurotransmitters[136]. The rate limiting step in this shuttle is the Glu-Asp antiporter located in the inner mitochondrial membrane [23] and an increase in shuttle activity would therefore be expected to lead to the changes observed by Mangia *et al.* (2007) and confirmed in our studies.

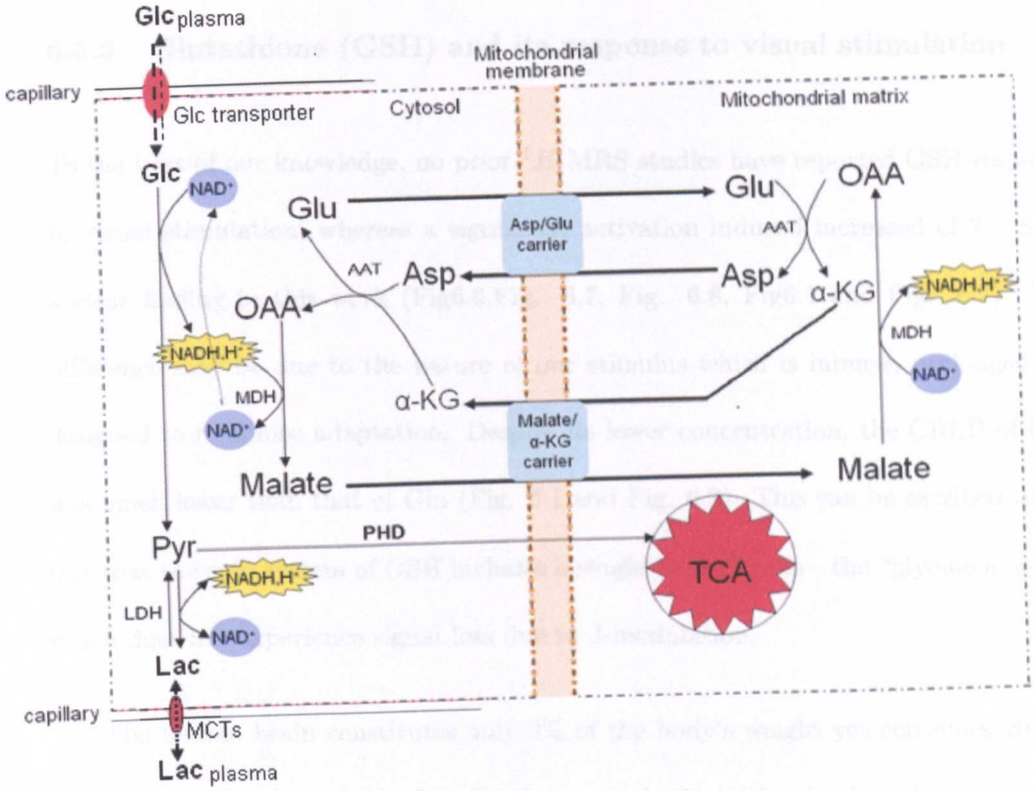

Figure 6.9: Schematic illustration of malate-aspartate shuttle (MAS). First, oxaloacetate (OAA) on the cytosol side is reduced by NADH, creating malate and NAD^+. Malate and the electrons it carries are transported into the mitochondria across the inner mitochondrial membrane, in exchange for alpha-ketoglutarate ($\alpha - KG$) which is transported out of the mitochondria. Once inside, the energy in malate is extracted again by reducing NAD^+ to make NADH, regenerating OAA. This NADH is then free to transfer its high energy electrons to the electron transport chain. The OAA is transaminated with Glu to make Asp and $\alpha - KG$. Asp is returned to the cytosol by the Asp-Glu transporter, which moves Glu into the mitochondria as it transports Asp out. The overall result is that NADH is transported into the mitochondria, and can be used to generate 3 ATP per every NADH transported in from the cytosol, a very efficient process.

6.5.3 Glutathione (GSH) and its response to visual stimulation

To the best of our knowledge, no prior ^1H-MRS studies have reported GSH responses to visual stimulation, whereas a significant activation induced increased of $7-8\%$ is a clear finding in this work (Fig6.6,Fig. 6.7, Fig. 6.8, Fig6.1 and Fig. 6.2). This difference may be due to the nature of our stimulus which is intense, prolonged and designed to minimise adaptation. Despite its lower concentration, the CRLB of GSH was much lower than that of Gln (Fig. 6.1 and Fig. 6.2). This can be ascribed to the fact that the spin system of GSH includes a singlet at 3.77 ppm - the "glycine moiety", which does not experience signal loss due to J-modulation.

The human brain constitutes only 2% of the body's weight yet consumes 20% of the oxygen utilized by the body . Further, visual stimulation leads to large increases $(approaching 50\%)$ in the cerebral metabolic rate in the visual cortex, and though still a matter of contention; this increase is likely to be primarily aerobic[149]. The increase in mitochondrial respiration is inevitably accompanied by an increase in the generation of reactive oxygen species (ROS), such as superoxide anion $(O2^-)$, peroxynitrite $(ONOO^-)$, and hydrogen peroxide (H_2O_2), which cause oxidative damage of nucleic acids, lipids, carbohydrates and proteins [150]. It has become increasingly clear that free radicals can be released towards cytosol where it can be detoxificated by GSH [151, 150]. Brain imaging techniques have demonstrated that functionally active neurons triggered by photic stimulation, show increased metabolic activity and oxygen consumption [152], resulting in increased generation of ROS [153]. ROS generation has to be counter-balanced by GSH to enable a long human life. So it is reasonable to expect that GSH would be present in significant amounts in the brain, and also that prolonged periods of visual stimulation might result in an increase in its level in visual cortex as we observe. During detoxification, GSH is oxidized to glutathione disulfide

(GSSG). However, GSSG does not accumulate, because it is rapidly reduced back to GSH by glutathione reductase, and in normal brain, GSSG constitutes only approximately 1% of total GSH. Maintenance of a highly reduced GSH pool is important to protect against excessive free radical formation. GSH is a tripeptide, made up of the amino acids Glu, cysteine (Cys) and Gly. It is interesting to note that the increase in GSH during visual stimulation is mirrored by a decrease in Gly, one of its metabolic precursors, as might be expected.

An alternative hypothesis for the observed increase in GSH during stimulation relates to the clearance of the increased Glu generated during the intense neuronal activation(Glu is also a metabolic precursor of GSH). Further, activation of the Glu NMDA channels requires simultaneous binding of both Glu and its coagonist Gly [154]. The increased GSH synthesis during prolonged intense visual stimulation will deplete pools of both agonists, and could therefore reduce activation of the NMDA receptor, therefore protecting against Glu-induced excitotoxicity. In addition, it has been known that Glu acts on its receptor via a nitric oxide (NO) mechanism [155]. Free radicals reduce the capacity of high-affinity Glu transport systems presenting in synaptic terminals and astrocytes, to prevent Glu to be taken up and removed from the extracellular space, which would significantly increase extracellular Glu levels, potentiating Glu excitotoxicity [156]. Therefore, GSH reacting with NO can further release the Glu excitotoxicity. (Activation of the NMDA receptor results in the Ca^{2+}-induced activation of nitric oxide synthase which in turn leads to NO production, inhibition of glutamine synthetase and accumulation of Glu[156]).

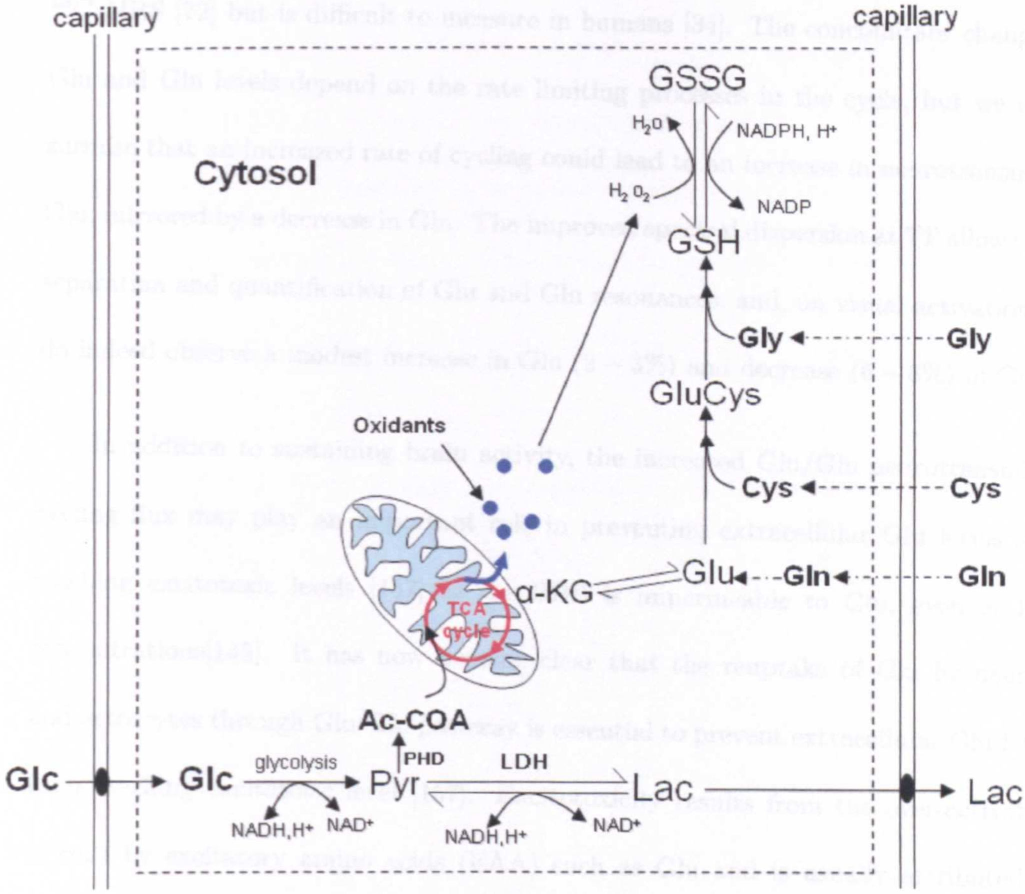

Figure 6.10: Function of GSH as an antioxidant. Free redicals are produced inside the mitochondrion and can be released towards cytosol where it can be detoxificated by GSH.

6.5.4 Stimulus driven changes in neurotransmitter cycling

The principal excitatory neurotransmitter in the cortex of the human brain is Glu. It is released from synaptic vesicles in the pre-synaptic terminal into the synaptic cleft where it activates receptors in the post-synaptic membrane. Glu is then transported, mainly into surrounding astrocytes, where it is first converted into Gln before being returned to the neurons and converted back into Glu (see Fig. 6.11). This Glu/Gln cycle sustains neural activity, and the flux through it would be expected to increase on neural stimulation ~ something that has been demonstrated in animal studies using

^{13}C MRS [72] but is difficult to measure in humans [34]. The concomitant changes in Glu and Gln levels depend on the rate limiting processes in the cycle, but we might surmise that an increased rate of cycling could lead to an increase in neurotransmitter Glu, mirrored by a decrease in Gln. The improved spectral dispersion at 7T allows clear separation and quantification of Glu and Gln resonances, and, on visual activation, we do indeed observe a modest increase in Glu (2 – 3%) and decrease (6 – 8%) in Gln.

In addition to sustaining brain activity, the increased Glu/Gln neurotransmitter cycling flux may play an important role in preventing extracellular Glu levels from reaching excitotoxic levels [157] as the BBB is impermeable to Glu, even at high concentrations[145]. It has now become clear that the reuptake of Glu by neurons and astrocytes through Glu-Gln pathway is essential to prevent extracellular Glu levels from reaching excitototic level [157]. Excitotoxicity results from the over-activation of cells by excitatory amino acids (EAA) such as Glu and is usually attributed to over stimulation of both ionotropic (NMDA and non-NMDA (AMPA and kainate)) and metaboltropic receptors, leading to increased calcium (Ca^{2+}) flux into the cytosol [158]. The Ca^{2+} will trigger a cascade of reactions, including the free radical generation, eicosanoid production, and lipid peroxidation, which will destroy the cell. Non-NMDA and metaboltropic receptors are coupled to Na^{+} channels, though lacking the GluR2 subunit also permeable to Ca^{2+} [159], and they mediate fast glutamatergic transmission. Activation of these latter receptors also contributes to NMDA receptor responses [160]. During neuronal activation, extracellular Glu concentration is increased and the Glu receptors on neurons and astrocytes are exposed to over-stimulation. Due to the impermeability of BBB to Glu even at high concentration [145], clearance of Glu from the extracellular space to maintain extracellular Glu concentrations below toxic level is very important. Therefore, the increase in Glu-Gln cycling flux protect against the development of neurotoxicity by preventing the accumulation of the extracellular Glu.

The inhibitory neurotransmitter GABA is formed by decarboxylation of Glu and is recycled via Gln in a Gln/Glu/GABA (Fig6.11). Again we might surmise that stimulation would lead to an increase in flux through this cycle[161]. In our experiments, GABA, like Glu, exhibited a tendency to increase throughout both the single and double (fig6.8) stimulation periods, but this change did not reach statistical significance.

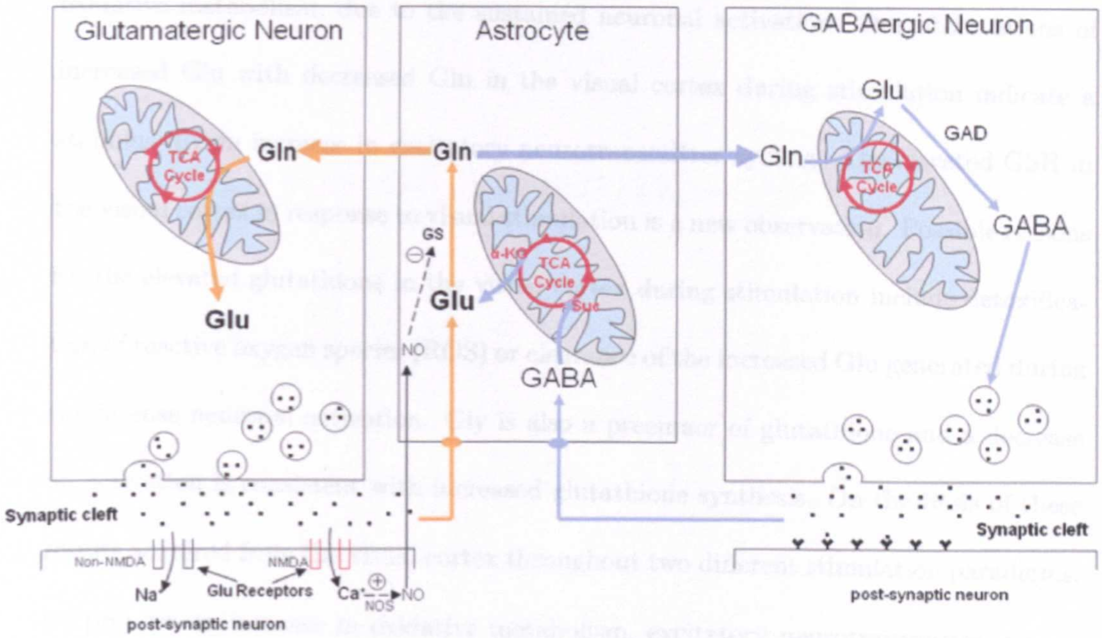

Figure 6.11: Schematic illustrations of Glu/GABA-Gln cycling bewteen neuron (glutamatergic and GABAergic neuron) and astroglia. In neurotransmission, released Glu from the nerve terminals is taken up by surrounding astroglia cells, where it is converted to Gln , then diffuses back to the presynaptic neuron and reconverted to Glu, thereby completing the well-known Glu-Gln cycle. Similarly, in the inhibitory synapse, GABA is released from GABAergic neurons and is taken up into astrocytes, catabolized to the TCA cycle intermediate succinate and subsequently converted to $\alpha-ketoglutarate$ and glutamate, and recycled to GABAergic neurons to form the GABA-glutamine cycle.

6.6 Conclusions

In combination with our results, finding of significant metabolic changes associated to two different visual stimulation paradigms showed that observed constant decrease of Glc and Asp with elevated lactate in response to visual stimulation suggests an increased oxidative metabolism, due to the sustained neuronal activation. Our observations of increased Glu with decreased Gln in the visual cortex during stimulation indicate a stimulus driven increase in excitatory neurotransmitter cycling. The elevated GSH in the visual cortex in response to visual stimulation is a new observation. Possible reasons for the elevated glutathione in the visual cortex during stimulation include detoxification of reactive oxygen species (ROS) or clearance of the increased Glu generated during the intense neuronal activation. Gly is also a precursor of glutathione and a decrease on activation is consistent with increased glutathione synthesis. On the basis of these results acquired from the visual cortex throughout two different stimulation paradigms, we propose an increase in oxidative metabolism, excitatory neurotransmitter cycling and glutathione synthesis, possible related to Glu clearance and ROS detoxification.

Chapter 7

Dynamics of stimulus-induced lactate changes in human visual cortex detected by ^{1}H MRS at 7T

7.1 Introduction

The metabolic events of neuronal energetics during functional activity remain subject to intense debate. Lac plays a crucial role in energy homeostasis in both physiological and pathological conditions[12], and has been receiving special attention in the human brain, since the functional involvement of this metabolite was firstly hypothesized by Fox *et al.*[4], who found an uncoupling between oxygen and glucose consumption during long stimuli and suggested the possibility that certain types of functional activity might selectively stimulate anaerobic glycolysis. Lac production is therefore expected to increase in the absence of a parallel increase in oxidative metabolism.

During the past 20 years, functional ^{1}H MRS has been used in a number of studies, under a variety of experimental conditions and functional paradigms, to non-invasively assess the temporal changes of Lac in the activated human brain[17, 18, 7, 6, 19, 20, 21, 22, 23]. However, studies observing Lac during stimulation have come to various different conclusions. Prichard *et al.*[17] first reported changes in Lac level during sustained visual stimulation, measuring a 60% increase in Lac level during the first 6 min of activation, followed by a decrease back towards baseline over the following 15-20 minutes. Sappey-Marinier *et al.*[18] measured up to a 250% increase of Lac in the first 6.4 min during visual stimulation and a return towards baseline during the second 6.4 min block. Frahm *et al.*[6] observed a 68% increase in the Lac level during the first half of a 6 min stimulation period, followed by a decrease to the basal level during ongoing stimulation. However, the feasibility of measuring Lac changes under stimulation has been challenged by other authors: Merboldt *et al.*[7] could not detect any reproducible time-course of Lac during several kinds of visual stimulation; Boucard *et al.*[19] failed to detect any Lac signal during prolonged stimulation.

In order to gain temporal resolution and avoid the ambiguities related to prolonged stimulation, Mangia *et al.*[20] used a GE 1.5T scanner with a TE=270ms PRESS localized sequence, to analyse the evolution of Lac during the early seconds following a brief visual stimulation. This report showed a marked decrease of Lac below the resting value within 5s from the end of the stimulation, followed by a return to the baseline at about 12s after the end of the stimulation. Mangia postulated that this initial decrease in Lac could be due to its utilization to produce energy during the first few seconds, alternatively, this decrease could be due to locally occurring hypoglycaemia. More recent studies by Mangia *et al.*[23], taking advantage of the increased SNR and spectral resolution at 7T, with ultrashort TE and a long TR, have observed changes in Lac by 23% ± 5% within the first minute of activation, which reach a new steady state level and then came back to baseline after the end of the stimulus. The observed

Lac level during activation at 7T by Mangia *et al.*[23] is different from those measured by Pritchard and Sappey-Marinier, which may be due to differences in experimental protocol. Pritchard and Sappey-Marinier used long TE PRESS sequences to measure Lac, which result in underestimation, as Lac is in a "short T_2 pool", whilst Mangia *et al.* used an ultra-short TE (6ms) and long TR(5s) STEAM sequence, which minimizes T_2 and T_1 relaxation effects, and, ultimately leads to very reproducible results with a high SNR.

Our results, described in Chapter 6, show an early Lac increase above baseline of up to $0.2 \mu mol/g$ (26% ± 7%) with a subsequent return towards baseline (Fig. 6.6.B, Fig. 6.7.B, Fig. 6.8 in chapter 6). This is consistent with the first report of Lac increase during sustained visual stimulation by Prichard *et al.*[17], later confirmed by Frahm *et al.*[6]. The possible reasons for the observed decrease in Lac in the later stage of stimulation, might be due to its utilization instead of Glc as an alternative energy substrate[11]. Also the net increase of Lac efflux to blood through the BBB might also account for its decrease during a prolonged stimulus[146]. Any newly produced Lac was immediately released as lactic acid into the extracellular compartment via a Lac/proton cotransport[162]. Of great interest is the lack of Lac response to a second period of visual stimulation: in a repeated 9.9-min stimulation, significant Lac increase was only evident in the first period of stimulation ($30\% \pm 7\%$), but no Lac accumulation was observed in the second 9.9 min stimulation.

The reasons for the absence of a Lac elevation, under the second stimulation, are unclear. It is possible that processes triggered during the first period of visual stimulation, could continue for a while after stimulation has ended. If this is an important mechanism of the activity-stimulated brain Lac response, then shortening the duration of the first stimulus might lead to an increase in Lac response during the second period of stimulation. With this in mind, we designed a repeated visual stimulation paradigm, varying the duration of first stimulation (shorter than 9.9-min, based on our previous results), to see the effect on the Lac response during the second visual stimulation period.

7.2 Aim

The goal of the present experiments was to further probe the Lac response to repeated stimuli.

7.3 Materials and methods

7.3.1 Human subjects

6 healthy male subjects (age=25 ± 3 year) without history of neurological disorders participated in this experiment. Data for each initial stimulus duration were collected at least two weeks apart. The same subjects participated in all stimulation durations. Informed consent was obtained before MR examination according to procedures approved by the University of Nottingham Medical School Ethics Committee.

7.3.2 Magnetic resonance imaging and spectroscopy

All MR measurements were acquired using a Philips Achieva 7T MR system and a 32-channel head coil. All first and second order shim terms were automatically adjusted using FASTMAP with EPI readout[138]. Head movement was minimized by positioning two pieces of foam surrounding the subjects head.

fMRI Measurement An initial fMRI scan (EPI, TE/TR=26/2200ms, $2 \times 2 \times 2mm^3$ isotropic voxels, functional paradigm: 4.4s stimulation and 28.6s rest, 8 repeats) was performed prior to spectroscopic acquisition, in order to determine the region of maximum activation in the visual cortex (the same visual stimulus as described previously in Chapter 6, was used during the whole experiments). fMRI data were analysed in real-time using IViewBOLD in order to determine the region of maximum activation in the visual cortex.

MRS Measurement MRS Measurement: A cubic VOI of $8cm^3$ was positioned inside the activated region for functional MRS acquisition. ^{1}H MRS data were continuously acquired using a short TE STEAM sequence (TE/TM/TR=13/17/2000ms, spectral width 4000Hz, 4096 time points), employing MOIST water suppression[139]. 2 acquisitions without water suppression were acquired prior to the water suppressed spectra for referencing concentration and for eddy current correction. Four different repeated visual stimulation protocols were investigated (two resting periods interleaved with two stimulation periods), in which the first stimulus duration was 1s, 16s, 48s, and 288s respectively. The two resting periods and the last simulation period was kept constant at 544-s, with the protocol OFF (544s)-ON(1s)-OFF(544s)-ON (544s), OFF (544s)-ON(16s)-OFF(544s)-ON (544s), OFF (544s)-ON(48s)-OFF(544s)-ON (544s) and OFF (544s)-ON(288s)-OFF(544s)-ON (544s),respectively.

7.3.3 Post-processing

Data for each individual spectrum were saved separately and were processed as in Chapter 6, including frequency and phase corrections of each single scan, spectra summation in blocks, and removal of residual eddy currents using the reference water signal from the same VOI. Spectra from each subject acquired during the second 544-s (272 scans) stimulation periods, were averaged into groups of 48 blocks (96s per block), as were all the first and the second resting 272 spectra for each subject. A moving averaging (sliding offset = 16 scans) was performed to increase the nominal time resolution up to 32s in single subject studies (e.g., scans 1-48, 33-80, 65-112, etc.). For the spectra acquired during the longer initial stimulation periods(288s), same spectra summation was performed from each subject. In addition, spectra were averaged across the individual rest and stimulation periods for each subject.

7.3.4 Metabolite quantification

Time courses of Lac were achieved through quantifying every summed spectrum (time resolution =96s) in each subject, using LCModel(see details in Chapter 5 and 6) and averaged inter-subject trajectories of metabolites were calculated from all 6 subjects. Resulting outputs were rejected if the $\%SD$ from LCModel was ¿ 20%. As previously reported, though BOLD effects would change the linewidth of both water and metabolite signals during stimulation[125], the quantification of metabolites was almost unaffected, especially for Lac, by line broadening up to 0.5Hz [21]. The observed line narrowing effect is approximately 0.5 Hz at 7T. Lac changes indicated by LCModel are therefore robust. The percentage change in Lac was calculated with respect to the first 544s basal level of each individual.

7.3.5 Statistical analysis

A Wilcoxon signed rank test was conducted to compare the Lac changes during the second 544-s stimulation versus the first 544-s resting period for the four functional paradigms. Values are presented as $mean \pm SD$ and $p \leq 0.05$ is considered as statistically significant.

7.4 Results

In vivo ^{1}H NMR spectra obtained during the first 544-s rest and the second 544-s stimulation periods from the same subject, with the voxel localized inside the activated visual cortex, are shown in Fig .7.1, as an example of the quality that was routinely achieved throughout the whole study. Narrow small peaks (line width around 0.5Hz) at the positions of the strong singlet resonances of NAA (2.01ppm) and tCr (3.0ppm) were visible in the difference spectra (Fig .7.1(iii)) which were attributed to the linewidth changes due to the BOLD effect [125]. This difference spectrum further confirms that the voxel was positioned in the activated visual cortex during the entire experimental session.

Fig. 7.2 shows the intersubject time-course of Lac percentage variations with respect to the basal level (during the initial 544-s resting periods) of each individual. These variations are expressed as a percentage of the first rest level for each individual, in order to remove the large intersubject variability. A gradual increase in Lac under the second prolonged stimulation, following the first brief stimulation (1s, 16s and 48s, respectively), was observed and maintained at a higher level until the end of this periods (Fig. 7.2 (A),(B),(C)). The averaged Lac concentration, under the second stimulation, was increased above baseline by $28\% \pm 12\%$ ($0.23 \pm 0.1 \mu mol/g$, $p = 0.011$), $28\% \pm 9\%$ ($0.24 \pm 0.08 \mu mol/g$, $p = 0.021$) and $20\% \pm 12\%$ ($0.16 \pm 0.1 \mu mol/g$, $p = 0.038$), respectively(Table 7.1). Similar Lac responses during the second stimulation periods were observed whether the first stimulation was 1s or 16s. However, the observed Lac response was slightly lower when the first stimulation was 48s, compared with that of 1s and 16s (Fig. 7.2.(C)). No significant Lac increase can be evident under the second stimulation periods, when the initial stimulation was 288s (Fig. 7.2.(D)). The averaged Lac level, after cessation of the first 288s stimulus, was significantly below

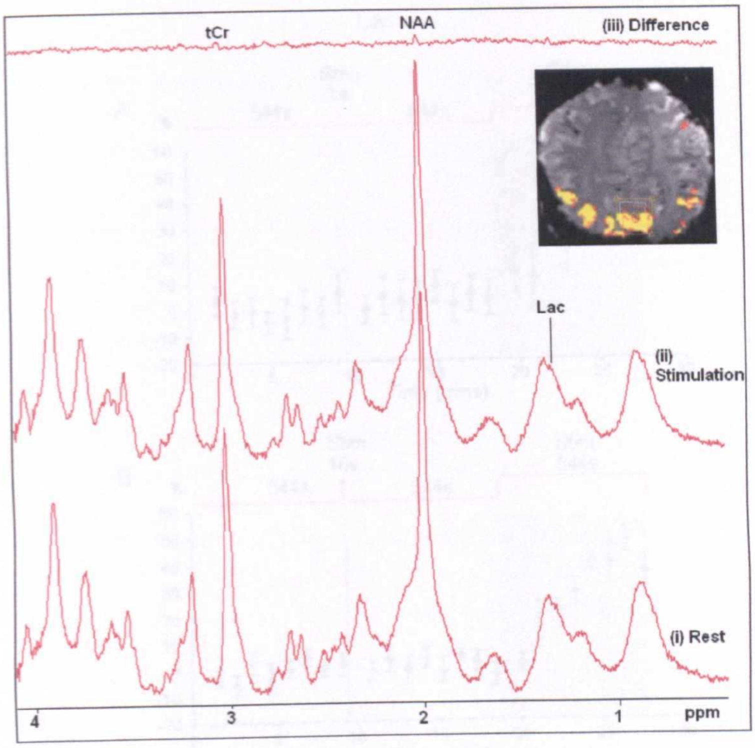

Figure 7.1: Representative 7T ^1H MRS spectrum acquired during the first 544-s resting (i) and the second 544-s stimulation periods; (ii) from a single subject; (iii) difference spectra between (i) and (ii). Inset picture: representative example of BOLD response with the voxel position for MRS indicated by a white square (the yellow box shows the shim volume).

baseline (decreased by $14\% \pm 9\%$ ($0.15 \pm 0.1\mu mol/g$, $p = 0.038$)). In good agreement with our previous results (Chapter 6), during the initial 288s stimulation, Lac elevation ($18\% \pm 11\%$ ($0.16 \pm 0.1\mu mol/g$, $p = 0.044$)) can be observed at the early stage of stimulation, with a slightly tendency to decrease during prolonged stimulation (Fig. 7.2.(D)).

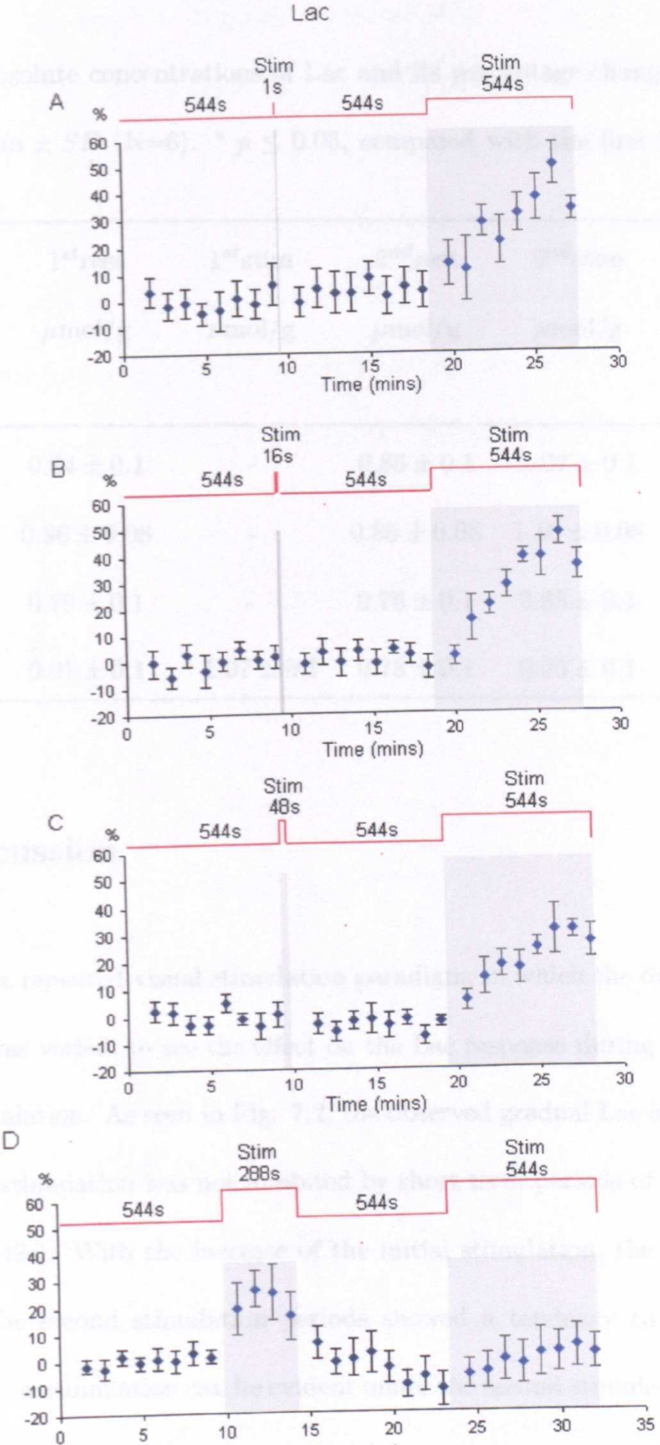

Figure 7.2: Intersubject time-course of Lac quantified with LCModel in 6 subjects, under four different stimulation paradigms(A:OFF (544s)-ON(1s)-OFF(544s)-ON (544s), B:OFF (544s)-ON(16s)-OFF(544s)-ON (544s), C:OFF (544s)-ON(48s)-OFF(544s)-ON (544s), D:OFF (544s)-ON(288s)-OFF(544s)-ON (544s)), expressed as a % relative to the averaged Lac level acquired during the initial 544-s resting period for each individual. Temporal resolution: 64 s in the individual studies. Data points are $means \pm s.e.m.$

Table 7.1: Absolute concentrations of Lac and its percentage changes on stimulation. Data are *mean* ± *SD* (N=6). * $p \leq 0.05$, compared with the first basal value before stimulus.

Initial stimulation (s)	1^{st}rest μmol/g	1^{st}stim μmol/g	2^{nd}rest μmol/g	2^{nd}stim μmol/g	changes 2^{nd}stim-1^{st}rest μmol/g	changes 2^{nd}stim-1^{st}rest %
1	0.84 ± 0.1	-	0.86 ± 0.1	1.07 ± 0.1	$^{*}+0.23 \pm 0.1$	$^{*}+28\% \pm 12\%$
16	0.86 ± 0.08	-	0.85 ± 0.08	1.10 ± 0.08	$^{*}+0.24 \pm 0.08$	$^{*}+28\% \pm 9\%$
48	0.79 ± 0.1	-	0.76 ± 0.1	0.85 ± 0.1	$^{*}+0.16 \pm 0.1$	$^{*}+20\% \pm 12\%$
288	0.91 ± 0.1	* 1.07 ± 0.1	0.78 ± 0.1	0.95 ± 0.1	-	-

7.5 Discussion

We designed a repeated visual stimulation paradigm, in which the duration of the first stimulation was varied, to see the effect on the Lac response during the second period of visual stimulation. As seen in Fig. 7.2, the observed gradual Lac increase during the second 544-s stimulation was not inhibited by short term periods of initial stimulation (1s, 16s and 48s). With the increase of the initial stimulation, the magnitude of Lac increase to the second stimulation periods showed a tendency to decrease, and no significant Lac accumulation can be evident under the second stimulation periods, when the initial stimulation was 288s.

Elevated Lac in the brain has been reported during visual stimulation in several ^{1}H-MRS studies [17, 18, 6, 23, 22], though the results have not been consistent. Our present findings of Lac time course under the second neuronal activation, following the initial brief stimulation (1s, 16s and 48s), showed later and gradual increase during a prolonged stimulus (see Fig. 7.2), which is in good agreement with previous results obtained by Mangia *et al.* at 7T[23]. There are several possible biochemical explanations for the present Lac results. Mostly likely is that the increased in energy demands arising from stimulation, is met by an increase in Glc metabolism, leading to increased glycolytic flux, subsequently, causing increased Pyr and Lac concentrations. Furthermore, Glc metabolism to Pyr generates NADH, which shifts the cytosolic redox state, causing increased Lac production from Pyr by Lac dehydrogenase (Fig. 7.3).

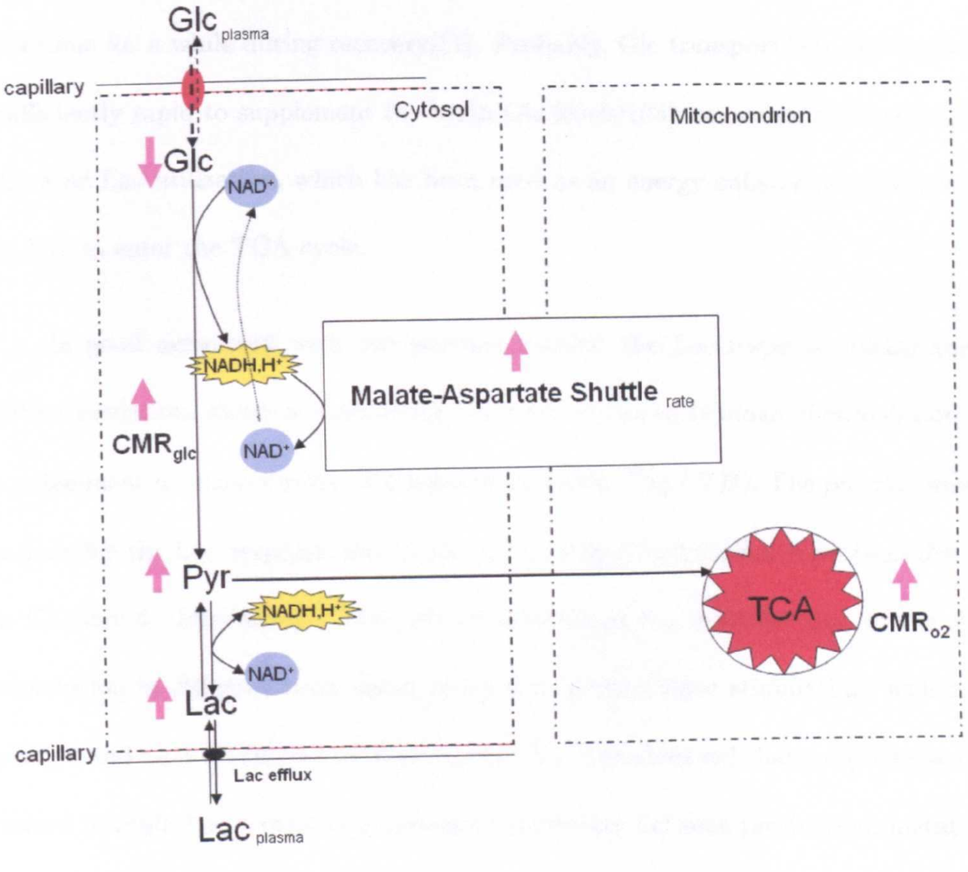

Figure 7.3: Schematics of metabolic events following increased neuronal activity. Increased CMR_{glc} during activation leads to decreased Glc. The increased Pyr, resulting from an increased glycolytic flux, brings about a corresponding increase in Lac. Lac efflux from the brain to the plasma occurs since plasma and brain Lac are supposed to be different.

However, there is no significant Lac accumulation under the second stimulation periods, following the initial longer stimulation of 288s (Fig. 7.2.(D)). It is most likely that the unobservable Lac elevation under the second stimulation might be related to a decreased Lac level during the second resting periods, which probably did not recover back to baseline after the first longer stimulation. In support of this, we found a significantly decreased Lac content by 14% ± 9% under the second resting period. It is possible that the increased glycolytic flux triggered by the initial stimulation would still continue for a while during recovery[11]. Probably, Glc transport into the brain is not sufficiently rapid to supplement the brain Glc levels[163], consequently bringing about elevated Lac utilization, which has been used as an energy substrate, to be converted to Pyr to enter the TCA cycle.

In good agreement with our previous results, the Lac response during the first 288s stimulation, shows a considerably increase at the early stage of stimulation, with a subsequent decrease during prolonged stimulation (Fig.7.2 D). The possible interpretations for the Lac response during the initial longer stimulation have been discussed in Chapter 6. Interestingly, this activity-stimulated Lac response due to the second stimulation is different from those under the initial longer stimulation, which show gradual and later elevation (see Fig.7.2 A, B, C). The observed changes (increase or decrease) in brain Lac represent a dynamic equilibrium between production, metabolism and fluxes between compartments, strongly depends on which is the dominant process. The elevated Lac content in the later stage of second stimulation periods is not likely to be due to a persistent oxygen deficiency, which might reflect a change in the Lac clearance rate relative to the producing rate, possibly mediated by the altered expression of Lac transporters[164, 165]. Lac is produced accompanied with a proton therefore its creation is always together with an increase in the outward proton gradient. This would facilitate Lac/proton outward cotransport and would explain the immediate release of most newly produced Lac. However, a variety of factors affect brain Lac transport system. Increased inward PH will decrease BBB permeability, resulting in decreased Lac efflux[166]. Monocarboxylic acids, pyruvate, can be competitively inhibiting the Lac-proton cotransport[165], which will reverse the direction of the Lac transport system[167], leading to a decreased Lac efflux or an increased Lac influx. Therefore, the possible explanation for the different Lac response, under the first and the second stimulation, might be due to the altered Lac efflux rate, which is mediated by the inner chemical environments.

It is also possible that the Lac changes we see under different stimulation paradigms reflect movement of Lac between compartments with radically different relaxation times. Currently, one of the most debated hypotheses to describe the metabolism of neuronal activation is the so-called astrocyte-neuron Lac shuttle (ANLS) hypothesis , this was produced by Pellerin and Magistretti[168] on the basis of experimental findings obtained in their cell cultures, postulating a major role for astrocyte-produced Lac as metabolic substrate to fuel the activated neurons. The ANLSH relies on the functional metabolic coupling between glutamatergic neurons and astrocytes, and suggests that Glu, released by neurons, whose taken up by glia stimulates Na^{+}-K^{+} ATPase and Gln synthetase activity. This stimulates astrocyte anaerobic glycolysis, thus producing Lac which is then exported to neurons to be converted back to Pyr and enter the neuronal TCA cycle. Since its introduction, many experimental and theoretical efforts have been devoted to examine the ANLS, providing evidence both in favor[169, 170] and against the ANLS[171, 172, 173]. It has been pointed out that the ANLS applies only to glutamatergic neurons and does not address how activity-related energy demands are met in nonglutamatergic neurons[174]. Mangia *et al*[163] utilized the mathematical model introduced by Simpson et al.[175] to study the compartmentalized metabolism *in vivo* during visual stimulation, and found out a mechanism referred to as neuron-to-astrocyte Lac shuttle (NALS). However, these hypothesis could not explain how the Lac relaxation times change between compartments, and could not contribute to the Lac transport mechanisms.

Further experiments are ongoing, varying the duration of second resting periods, to see the effect on the Lac response to the second stimulation.

Chapter 8

Measuring ^{13}C metabolic rates using $^{1}H\{^{13}C\}$ MRS at 7T

8.1 Introduction

The proton is the most commonly employed nucleus in the brain, due to its high abundance and sensitivity in vivo. Unfortunately the ^{1}H spectrum is definitely crowded, due to the small chemical shift range of around 10 ppm and its specificity suffers from the complex peak pattern due to J-coupling. Another difficulty encountered in ^{1}H-spectroscopy is the necessity to eliminate the large water and the lipid signal that obscure the metabolite signals presenting at millimolar or sub-millimolar concentrations.

^{13}C-MRS is analogous to proton MRS and allows the identification of carbon atoms in an organic molecule just as proton MRS identifies hydrogen atoms. ^{13}C MRS can provide "fingerprints" of organic compounds, due to the carbon atom being the fundamental constituent (backbone) of organic compounds. The advantages of ^{13}C-MRS compared with ^{1}H-MRS have been its lack of background signal due to water and its large chemical shift range of 200 ppm for carbon. Also, it allows the measurements of metabolic fluxes, such as the TCA cycle rate and the Glu-Gln cycling rate in different target compartments, which can not be determined by ^{1}H-MRS.

Unfortunately, the natural abundance of ^{13}C is only roughly 1.1% of the total carbon and its gyromagnetic ratio is approximately one-fourth of that of the proton. These two circumstances make ^{13}C-MRS an insensitive technique. A major obstacle to apply ^{13}C MRS to humans is the requirement to use ^{1}H decoupling, which simplifies the spectra considerably and enhances SNR substantially. However, we need avoid temperature elevation, which implies in turn an increased SAR, in the human body. Signal localisation is also a problem. Techniques used for protons, which are reliant on gradients to encode positional information, cannot be applied to ^{13}C due to the spread of ^{13}C resonances. All these things considered, this is a difficult and time-consuming experiment to attempt.

Despite these difficulties, continuing advance in magnet technology and acquisition techniques make ^{13}C MRS a more viable tool for studying human brain metabolism. The low abundance of the ^{13}C nucleus can be turned into advantage through the use of ^{13}C-enriched substrates, to enhance sensitivity, with little or no background interference from endogenous metabolites. This makes ^{13}C interesting to provide specific and quantitative information about metabolites and metabolic pathways. The high chemical specificity of ^{13}C MRS, distinguishes ^{13}C label incorporation not only into different molecules, but also into specific carbon positions within the same molecule, enables ^{13}C label incorporation in active metabolites to be followed and measured non-invasively through metabolic pathways. ^{13}C MRS studies have focused primarily on the metabolism of Lac, Glu, Gln and GABA which are responsible for energy metabolism and neurotransmitter cycling in the brain (see Fig. 3.21). Glu, Gln and GABA can be synthesized relatively rapidly in the brain, with the entire quantities turned over in about an hour. By following the flow of ^{13}C label from glucose, acetate, and other precursors into these metabolites, ^{13}C-MRS can now be used to discriminate many kinds of energy and neurotransmitter cycling fluxes rates including astrocytic and neuronal glucose oxidation, TCA cycling, Glu-Gln neurotransmitter cycling, GABA-Gln cycling, Glu synthesis, pyruvate carboxylase flux, as well as neuronal α-ketoglutarate-Glu exchange and other parameters [176, 177, 178], from the measured time courses of label incorporation and fractional enrichments obtained experimentally with a metabolic model[31]. The Sir Peter Mansfield Magnetic Resonance Centre (SPMMRC) in Nottingham is amongst the few that have expertise in the area of human ^{13}C spectroscopy[179].

^{13}C metabolic studies commonly involve four steps. (1) To select suitable ^{13}C-labeled substrates and infuse them into blood. (2) To detect ^{13}C spectra during infusion of ^{13}C labelled substrate. (3) To analyse ^{13}C-labelling time course of fractional enrichment. (4) To fit the time course through metabolic modelling to obtain quantitative metabolic fluxes through specific biochemical pathways.

8.1.1 Choice of ^{13}C-labelled substrate

Glucose is the main fuel for the brain and it can be oxidized in both neurons and astrocyte. ^{13}C-labelled glucose has been the preferred substrate for metabolic studies in the brain. By infusing ^{13}C-labelled glucose we can track the ^{13}C label as it is transported across the blood brain barrier and metabolized through the TCA cycle. [1-^{13}C]glucose or [1,6-$^{13}C_2$]glucose has been widely used for *in vivo* metabolic studies. Both substrates lead to the formation of [3-^{13}C]pyruvate, with one labeled pyruvate generated per molecule of [1-^{13}C]glucose and two labeled pyruvates generated per molecule of [1,6-^{13}C]glucose. Pyruvate is then metabolized either through pyruvate dehydrogenase(PDH) or pyruvate carboxylase(PC) or Lac dehydrogenase (LDH). Through PDH, [3-^{13}C]pyruvate yields [2-^{13}C]acetyl-CoA, which then combines with an unlabelled molecule of oxaloacetate to generate citrate labeled at the C_4 position. Subsequently, α-ketoglutarate becomes labeled at the C_4 position. The large pool of cytosolic Glu then becomes labeled at the C_4 position through transamination of [4-^{13}C]α-ketoglutarate and transport through the mitochondrial membrane. The ^{13}C-label can then be transferred to Gln and GABA. At the same time, ^{13}C-label continues to flow into the TCA cycle and label succinate. Since succinate is a symmetric molecule, the C_2 and C_3 positions of succinate can not be distinguished and become labeled with equal probability. The first turn of TCA cycle is completed when oxaloacetate becomes labeled at the C_2 and C_3 positions. Labeled molecules of oxaloacetate can combine again with labeled (or unlabeled) acetyl-CoA and will label the C_2 and C_3 positions of Glu in the second turn of the TCA cycle.

The use of glucose as a substrate presents a number of advantages for metabolic modelling in the brain. Firstly, it is generally accepted that brain metabolism is not affected by glucose concentrations[180]. Secondly, under hyperglycemic conditions, the liver releases little glucose into the blood, preventing additional sources of unlabeled substrates from entering the brain through the circulation.

The astrocyte-specific ^{13}C-labelled substrate, [2-^{13}C]acetate, is metabolized exclusively in the astrocyte. Infused [2-^{13}C] acetate only enters the astrocyte TCA cycle via pyruvate dehydrogenase (V_{PHD}) pathway and labels C4-Glu/Gln and C_2-GABA in the first turn of TCA cycle, then C_3-Glu/Gln, C_2-Glu/Gln and C_3/C_4 GABA are labelled in the subsequent turn. [2-^{13}C] acetate has been used in combination with [1-

^{13}C]glucose to provide estimates of metabolic fluxes in different target compartments, namely astrocytes and neurons in the same subject[181, 182].

8.1.2 Detection of ^{13}C NMR spectra

After ^{13}C labelling infusion, the incorporation of ^{13}C label from $[1 -^{13} C]$glucose to Glu, Gln or GABA can be monitored by the changes of NMR spectra during infusion. Fig. 8.1 shows a typical series of ^{13}C spectra, after subtraction of the baseline spectrum [179].

8.1.3 Analysis of the ^{13}C labelling time courses

Quantitative measurements of metabolic fluxes require analysis of the ^{13}C labelling time courses obtained experimentally with a metabolic model. Fig. 8.2 shows an example of the time course of the fractional enrichments of Glu-C_4, Gln-C_4, Glu-C_2, and Gln-C_2, corresponding to a basal study[179].

8.1.4 One-compartment metabolic modelling

When acquiring the time course of fractional enrichment we have to carry out metabolic modelling to get the metabolic cycling rates out. Methods for metabolic modelling have envolved from relatively simple models into complex four-compartment (neuron-astrocyte) models. When choosing a metabolic model we have to consider how many degrees of freedom can be allowed in the fit. The robustness of the fit would be greatly reduced if too many degrees of freedom are allowed together with too little experimental data[183]. For the one-compartment model, up to three free parameters are typically used: the TCA cycle rate V_{TCA}, the exchange rate between $\alpha - ketoglutarate$, Glu (V_x)

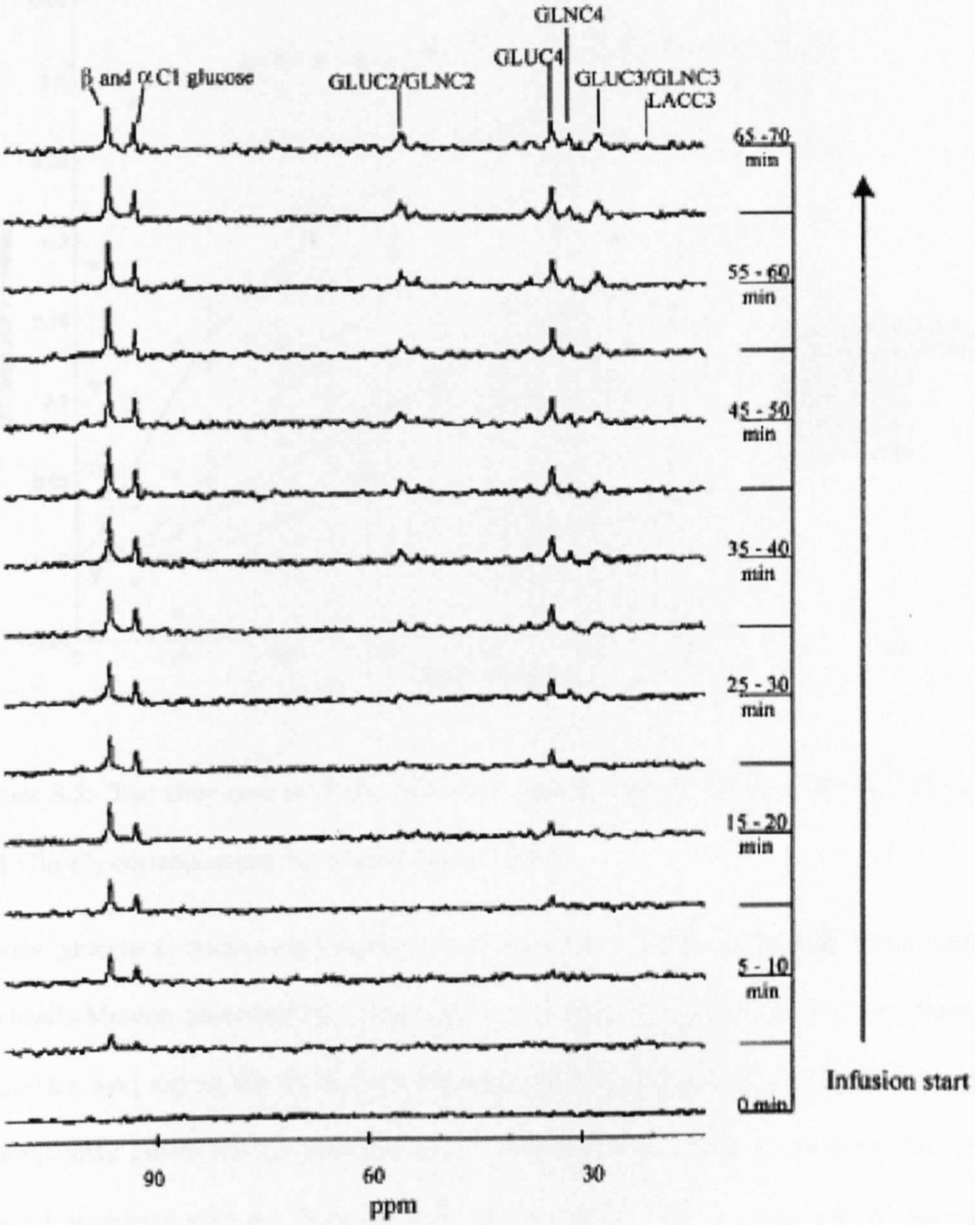

Figure 8.1: Complete spectral time series during ^{13}C labelling infusion [179]. The initial spectrum was taken before [1-^{13}C]glucose infusion.

and the isotopic dilution rate (V_{DIL}) due to exchange of labeled Lac with unlabeled Lac.

The one-compartment model describes the flow of [1-^{13}C]glucose into Glu C_4 and Glu C_3/C_2. ^{13}C incorporation into brain metabolites was modelled as shown Fig. 8.3.

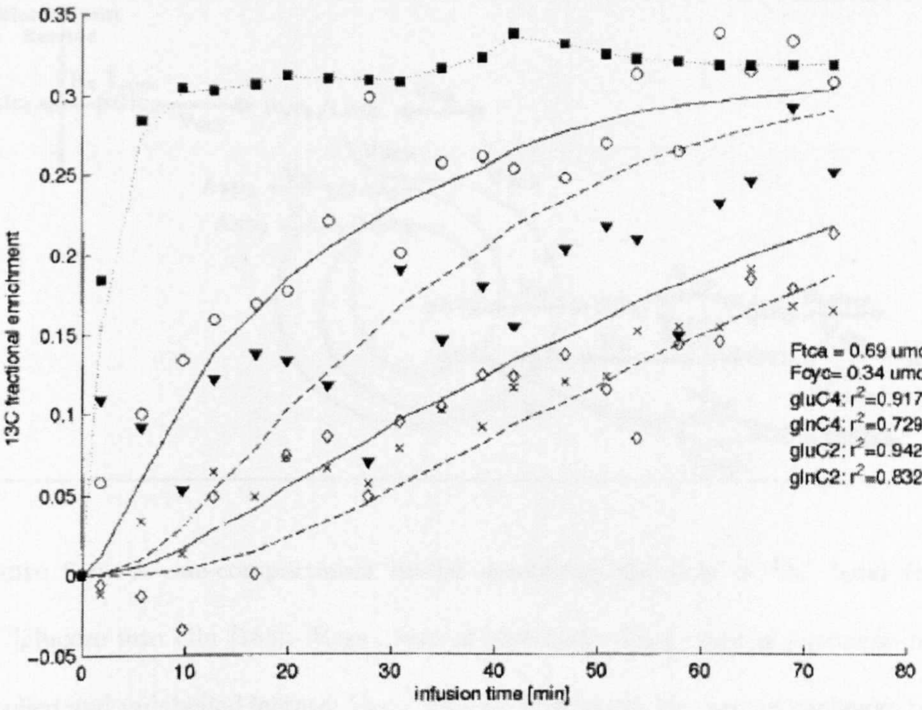

Figure 8.2: The time course of the fractional enrichments of Glu-C_4, Gln-C_4, Glu-C_2, and Gln-C_2 corresponding to a basal study [179].

Firstly, glucose is transported through the blood-brain barrier according to reversible Michaelis-Menten kinetics[184]. Brain glucose is then converted to Pyr/Lac through glycolysis, and enters the TCA cycle through PDH at the rate V_{tca}. The ^{13}C isotope subsequently labels the C_4 position of $\alpha - ketoglutarate$. Glu C_4 becomes labelled through exchange with $\alpha - ketoglutarate$ at the rate V_x. Gln is then labelled through exchange with Glu at the rate of V_{gln}. The ^{13}C isotope is then incorporated into oxaloacetate C_2 and C_3. Aspartate becomes labelled through exchange with oxaloacetate at the rate V_x (equal to the exchange rate between $\alpha - ketoglutarate$ and Glu). In the second turn of the TCA cycle, $\alpha - ketoglutarate$, Glu and Gln are labelled in the C_3 and C_2 positions. Since most Glu is located in neurons, fluxes obtained using this model reflect primarily neuronal metabolism.

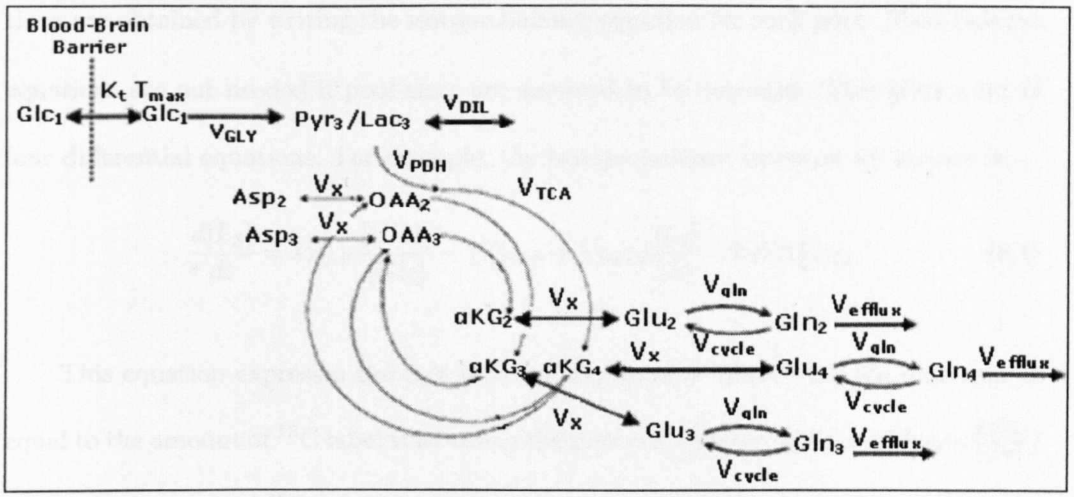

Figure 8.3: A one-compartment model describing the flow of ^{13}C label from [1-^{13}C]glucose into Glu [185]. V_{GLY}, rate of glycolysis; V_{DIL}, rate of exchange between labelled and unlabelled lactate; V_{TCA}, rate of TCA cycle; V_X, rate of exchange between α-ketoglutarate and Glu; V_{GLN}, rate of Gln synthesis; V_{cycle}, rate of Glu/Gln cycle; V_{efflux}, rate of Gln efflux.

8.1.5 Mathematical expression of the one-compartmental model

Once the model has been defined, it is expressed mathematically in a form suitable for numerical calculation. Several programs are currently in use for metabolic modelling. Some have used direct implementation of differential equations in Matlab[186]. Other programs feature a graphic interface that allows the user to define the model graphically (e.g., SAAM, CWAVE). The program then automatically generates the equations for the numerical calculations. These programs are very convenient to use, but may sometimes be less flexible than Matlab, e.g., to perform Monte Carlo simulation.

Consider the one-compartment model in Fig. 8.3: four differential equations are needed to express the model in a mathematical form, one for each pool in the model: pyruvate/Lac(considered as a single pool), α-ketoglutarate, Glu and Gln. These equations are obtained by writing the isotope balance equation for each pool. Mass balance equations are not needed if pool sizes are assumed to be constant. This gives a set of four differential equations. For example, the isotope balance equation for lactate is:

$$\frac{d[L_3]}{dt} = V_{GLY}\frac{[Glc1]}{[Glc]} - (V_{TCA} + V_{DIL})\frac{[L_3]}{[L]} + 0.011V_{DIL} \qquad (8.1)$$

This equation expresses the fact that the variation of labeled lactate over time is equal to the amount of ^{13}C label that enters the pool coming from glucose ($V_{GLY} * \frac{[Glc1]}{[Glc]}$) minus the amount of ^{13}C label that exits the pool to the TCA cycle ($(V_{TCA})\frac{[L_3]}{[L]}$) and through the exchange with unlabeled lactate ($(V_{DIL})\frac{[L_3]}{[L]}$). In this equation, $[L_3]$ is the concentration of lactate labeled at the C_3 position and [L] is the total (and constant) concentration of lactate. Similarly, [Glc$_1$] is the concentration of brain glucose labeled at the C_1 position and [Glc] is the total brain glucose concentration (not constant in general). V_{GLY} is the rate of glycolysis and is always assumed to be half of V_{TCA} because one molecule of glucose generates two molecules of pyruvate through glycolysis. Similar equations are obtained for the other metabolic pools (see Appendix).

Finally, the time course of brain glucose enrichment ([Glc$_1$]/[Glc]) can be obtained from the time course of plasma glucose concentration and isotopic enrichment by adding two more equations for glucose transport (one for mass balance and one for isotope balance)[187]. The mass balance equation is needed for glucose since brain glucose concentration is not constant when going from euglycemia to hyperglycemia at the beginning of the ^{13}C-glucose infusion.

$$\frac{d[Glc]_{brain}}{dt} = T_{max}\frac{[Glc]_{plasma}}{K_t + \frac{[Glc]_{brain}}{V_d} + [Glc]_{plasma}} - T_{max}\frac{[Glc]_{brain}}{V_d(K_t + [Glc]_{plasma}) + [Glc]_{brain}} - V_{GLY} \qquad (8.2)$$

$$\frac{d[Glc_1]_{brain}}{dt} = T_{max}\frac{[Glc_1]_{plasma}}{K_t + \frac{[Glc_1]_{brain}}{V_d} + [Glc_1]_{plasma}} - T_{max}\frac{[Glc_1]_{brain}}{V_d(K_t + [Glc_1]_{plasma}) + [Glc_1]_{brain}} - V_{GLY}\frac{[GlC]}{[GlC_1]} \tag{8.3}$$

Brain glucose concentrations can be expressed by the following equation[188].

$$[G_{brain}] = V_d\frac{[G_{plasma}](\frac{T_{max}}{V_{GLY}} - 1) - K_t}{\frac{T_{max}}{V_{GLY}} + 1} \tag{8.4}$$

where K_t (3.3 mmol/L) denotes the apparent Michaelis-Menten constant of glucose transport, T_{max} ($\mu mol g^{-1} min^{-1}$) is the corresponding maximal transport rate and the ratio of T_{max} relative to CMR_{glc}, T_{max}/CMR_{glc}, was 2.7 and V_d (0.77 ml/g) is the physical distribution space of glucose in the brain[189]. V_{GLY} is the rate of glycolysis and is assumed to be half of V_{TCA} because one molecule of glucose generates two molecules of pyruvate through glycolysis. Transport parameters as determined in α-chloralose anaesthetized rats(K_t=3.3mmol/L and T_{max}=2.7*V_{GLY}) were used in the model[190].

8.2 Initial experiments of parameter optimization for sensitivity enhancement in ^{13}C MRS at 7T

8.2.1 Experiment 1: Flip angle (FA) optimization

Background

The flip angle (FA) is the angle to which the net magnetization vector produced by a radio frequency (RF) pulse at the Larmor frequency is rotated relative to the direction of the main magnetic B_0 field. There exists a FA, for which the best SNR can be achieved for a given experiment(for a given tissue, echo time, repetition time, slice thickness, etc), which leads to increased reproducibility of MRS. However, the optimal FA cannot be obtained empirically because many parameters influence the actual FA. Hence it is important to find the optimal FA, according to a given experimental protocol.

Aim

To optimize the FA for Block pulses to obtain the best SNR for ^{13}C MRS.

Methods

A simple experiment was implemented using a Philips Achieva 7T MR system and a half-volume dual $^{1}H/^{13}$C channel coil system. ^{13}C spectra with Nuclear Overhauser Effect (NOE) enhancement were acquired using the pulse sequence (TE:shortest, TR:10000ms). A range of arbitrary FAs (from 10^o to 1000^o) for a Block pulse (defined on the scanner) was explored in intervals of 30^o for the range from 10^o to 570^o and intervals of 35^o from 580^o to 1000^o. A 2.5 cm spherical phantom containing [1-^{13}C] glucose was placed at a distance of 4cm from the centre of the coil. SNR (peak fitting) of the [1-^{13}C] glucose spectrum for each specific FA was measured using an inhouse built program in MATLAB.

Results

The relationship between FA and the SNR of a [1-^{13}C] glucose spectrum is shown in Fig. 8.4. As can be seen from this graph, the SNR for the [1-^{13}C] glucose spectrum increases dramatically and reaches its highest level (normalized to 100%) when the FA is 220^o, then drops to approx 45% level when the FA is 400^o, and gradually grows up again to 65% level, at approximate 560^o, and then slowly decreases again with the increasing FA.

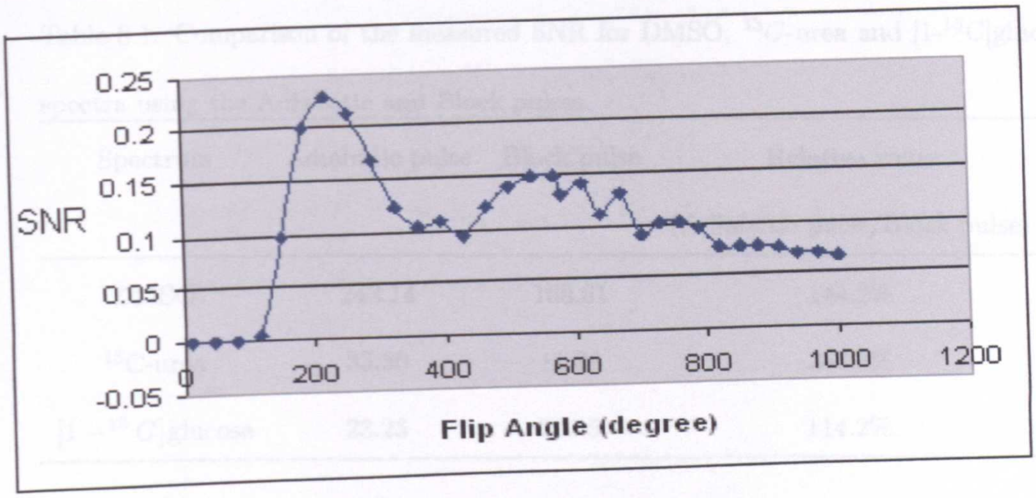

Figure 8.4: Relationship between FA and signal intensity in [1-^{13}C] glucose spectrum

Discussion

The optimum FA the for Block pulse is 220^o, in such condition the SNR for [1-^{13}C] glucose spectrum is maximum. However, the SNR distribution is not sine-shaped with increasing FA. Possible reason might be that there is a considerable variation in B_1 with this coil, even over the relatively small sample.

8.2.2 Experiment 2: Comparison of SNR between Adiabatic and Block pulses

Aim

To compare the SNR between Adiabatic and Block pulses.

Table 8.1: Comparison of the measured SNR for DMSO, ^{13}C-urea and [1-^{13}C]glucose spectra using the Adiabatic and Block pulses.

Spectrum	Adiabatic pulse	Block pulse	Relative value (Adiabatic pulse/Block pulse)
DMSO	243.14	168.61	144.2%
^{13}C-urea	33.30	11.88	280.3%
$[1-^{13}C]$glucose	23.23	20.35	114.2%

Methods

The DMSO phantom, ^{13}C-urea phantom and [1-^{13}C] glucose phantom were scanned respectively using both an Adiabatic and a Block pulse with an optimum FA of 220° (acquired from the first experiment). A distance of 4cm and identical parameters (TE, TR, NSA and samples) were used for both pulses. The SNR for each spectrum was measured using the built-in software at 7T.

Result

Comparison of the measured SNR for three spectra, acquired using Adiabatic and Block pulses, are shown in Table. 8.1. The SNR in DMSO, ^{13}C-urea and [1-^{13}C] glucose spectra acquired using the Adiabatic pulse were all higher than those acquired using the Block pulse.

Discussion

An adiabatic pulse is more effective for NMR spectroscopy, compared to Block pulses. Adiabatic pulses are a special class of RF pulses that can be used to achieve uniform flip angles in the presence of a nonuniform B_1 field, which offers a distinct advantage over Block pulses, to improve excitation homogeneity [191].

8.2.3 Experiment 3: Comparison of proton decoupling effect between standard broadband decoupling and WALTZ-16

Background

Although J-coupling can give valuable information on the chemical structure of compounds, the splitting often complicates spectra with overlapping peaks and further reduces sensitivity. This is because the multiple structures can be lost in the baseline noise as the peak heights decrease on splitting. In order to maximize the singal-to-noise ratio and spectral resolution in ^{13}C NMR spectra, proton decoupling can be applied during data acquisition, resulting in a simplified spectral pattern and enhancement of sensitivity.

Broadband ^{1}H decoupling is essential, since the protons of the metabolites of interest have chemical shifts distributed over about 5 ppm. There are two main broadband proton decoupling methods: standard broadband decoupling (BB) and composite pulse decoupling (WALTZ). They differ in the type of modulation of the proton frequencies. BB uses a continuous irradiation of proton frequencies with a train of rectangular pulses of identical duration and opposite phase[192], whereas the WALTZ pulse train uses blocks of ^{1}H pulses of different pulse lengths and phases. In practice, WALTZ is the most commonly used technique for proton decoupling as it has proved the most efficient and the most robust decoupling sequence, allowing decoupling of ^{13}C spectra using less decoupler power and diminishing the potential dielectric heating of the sample[193].

However, broadband decoupling at high field strengths requires high RF power and may cause tissue heating, subsequently induce an increased SAR [194]. Efficient ^{1}H decoupling minimizes local RF absorption. Therefore, it is still necessary to evaluate the decoupling performance of broadband decoupling techniques between WALTZ and BB, with respect to the SNR measurement of required peak and average RF powers.

Aim

To evaluate the decoupling performance of WALTZ-16 and BB decoupling, with respect to the SNR and average RF powers.

Methods

The 2.5cm spherical [1-^{13}C] glucose phantom was placed at a distance of 2cm from the coil. Acquisitions with identical parameters (TE: shortest, TR: 6000ms, NSA:256), were used for both WALTZ-16 and BB. Decoupling amplitude was changed in the range from $3\mu T$ to $20\mu T$, with an interval of $2\mu T$. The SNR of the spectrum was measured using the built-in software at 7T. SPSS statistical software was used to evaluate the significant difference in SNR and SAR between the two broadband decoupling methods.

Results

When the decoupling amplitude is $7\mu T$, well-decoupled Glc1α and Glc1β spectrum can be obtained using standard BB decoupling. However, the lowest optimum decoupling amplitude for WALTZ-16 is $13\mu T$, which is much higher than that of standard BB decoupling. There is no significant difference in SNR between Standard BB and WALTZ-16. However the SAR for WALTZ-16 is higher than that of standard BB (see

Table. 8.2).

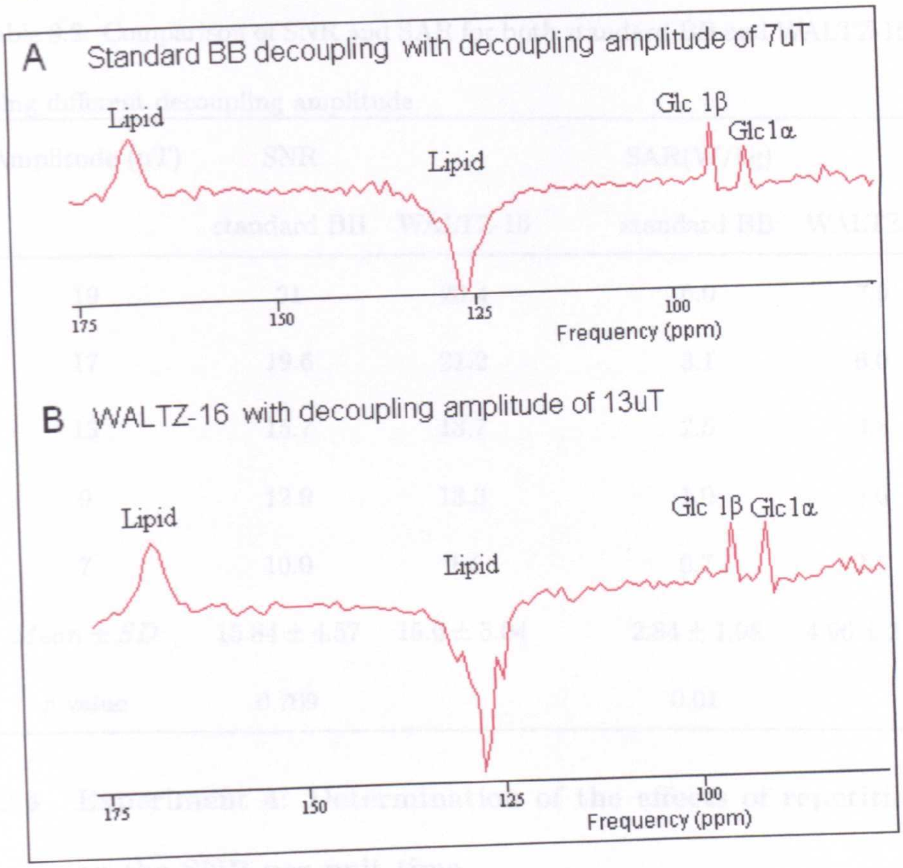

Figure 8.5: Examples of well-decoupled $[1-^{13}C]$ glucose spectra acquired using standard BB decoupling (A) and WALTZ-16 (B), with decoupling amplitude of $7\mu T$ and $13\mu T$, respectively.

Conclusions

Lower optimum decoupling B_1 ($7\mu T$) is needed for the standard BB decoupling method, to achieve well-decoupled $[1-^{13}C]$ glucose spectra, compared to WALTZ-16 ($13\mu T$). There is no significant difference in SNR gained in the glucose spectrum between standard BB and WALTZ-16. However the SAR value for WALTZ-16 is significantly higher than that using Standard BB decoupling. In summary, standard BB decoupling can provide superior decoupling performance than WALTZ-16.

Table 8.2: Comparison of SNR and SAR for both standard BB and WALTZ-16 through using different decoupling amplitude.

Amplitude (uT)	SNR		SAR(W/kg)	
	standard BB	WALTZ-16	standard BB	WALTZ-16
19	21	20.4	6.0	7.9
17	19.6	21.2	3.1	6.0
13	15.7	13.7	2.5	4.8
9	12.9	13.3	1.9	3.6
7	10.0	9.4	0.7	2.5
$Mean \pm SD$	15.84 ± 4.57	15.6 ± 5.04	2.84 ± 1.98	4.96 ± 2.10
p value	0.709		0.01	

8.2.4 Experiment 4: Determination of the effects of repetition time on the SNR per unit time

Background: The optimum flip angle for a given repetition time is given by the equation:

$$cos\theta = exp(\frac{-T}{T_1}) \tag{8.5}$$

where θ is the optimum flip angel or Ernst angle and T is the repetition time (Ernst 1996). The relative magnetization to M(T), or signal, changes with flip angle according to the equation:

$$\frac{M(T)}{M_0} = \frac{[1 - exp(\frac{-T}{T_1})]}{1 - cos\theta exp(\frac{-T}{T_1})} sin\theta \tag{8.6}$$

where M(T) is the z-magnetization at the delay time, and M_0 is the magnetization at equilibrium.

At the optimum pulse angle, it is important to know how the SNR varies with the pulse repetition time (T). An equation can be derived which allows this relationship to be investigated. Relative SNR per unit time is proportional to:

$$\propto \frac{M(T)}{M_0}\frac{1}{T^{\frac{1}{2}}} \tag{8.7}$$

where the $\frac{1}{T^{\frac{1}{2}}}$ term represents the square root of the number of FIDs accumulated in unit time.

From equations (8.5) and (8.6) and since: $sin\theta = [1 - cos^2\theta]^{\frac{1}{2}}$, the maximum signal-to-noise ratio per unit time at the Ernst angle:

$$\propto \frac{M(T)}{M_0}\frac{1}{T^{\frac{1}{2}}} \tag{8.8}$$

$$\propto \frac{[1 - exp(\frac{-T}{T_1})]sin\theta}{1 - cos\theta exp(\frac{-T}{T_1})}\frac{1}{T^{\frac{1}{2}}} \tag{8.9}$$

$$\propto \frac{[1 - exp(\frac{-T}{T_1})] * [1 - cos^2\theta]^{\frac{1}{2}}}{1 - cos\theta exp(\frac{-T}{T_1})}\frac{1}{T^{\frac{1}{2}}} \tag{8.10}$$

$$\propto \frac{[1 - exp(\frac{-T}{T_1})] * [1 - exp(\frac{-2T}{T_1})]^{\frac{1}{2}}}{1 - exp(\frac{-T}{T_1})exp(\frac{-T}{T_1})}\frac{1}{T^{\frac{1}{2}}} \tag{8.11}$$

$$\propto \frac{[1 - exp(\frac{-T}{T_1})]}{[1 - exp(\frac{-2T}{T_1})]^{\frac{1}{2}}}\frac{1}{T^{\frac{1}{2}}} \tag{8.12}$$

If the expression is multiplied by $\sqrt{T_1}$, it can be expressed solely in terms of the dimensionless parameter, $(\frac{T}{T_1})$

$$\propto \frac{[1 - exp(\frac{-T}{T_1})]}{[1 - exp(\frac{-2T}{T_1})]^{\frac{1}{2}}}\sqrt{\frac{T_1}{T}} \tag{8.13}$$

Results Plotting equation (8.13) for different values of T/T_1 allows us to observe how SNR changes with pulse repetition time (T) at the Ernst angle. The maximum value of this expression is 0.7068 (See Fig. 8.6) and is obtained when T tends to 0. The maximum SNR per unit time (Equation 8.13) is therefore, $\propto \frac{1}{\sqrt{T_1}}$.

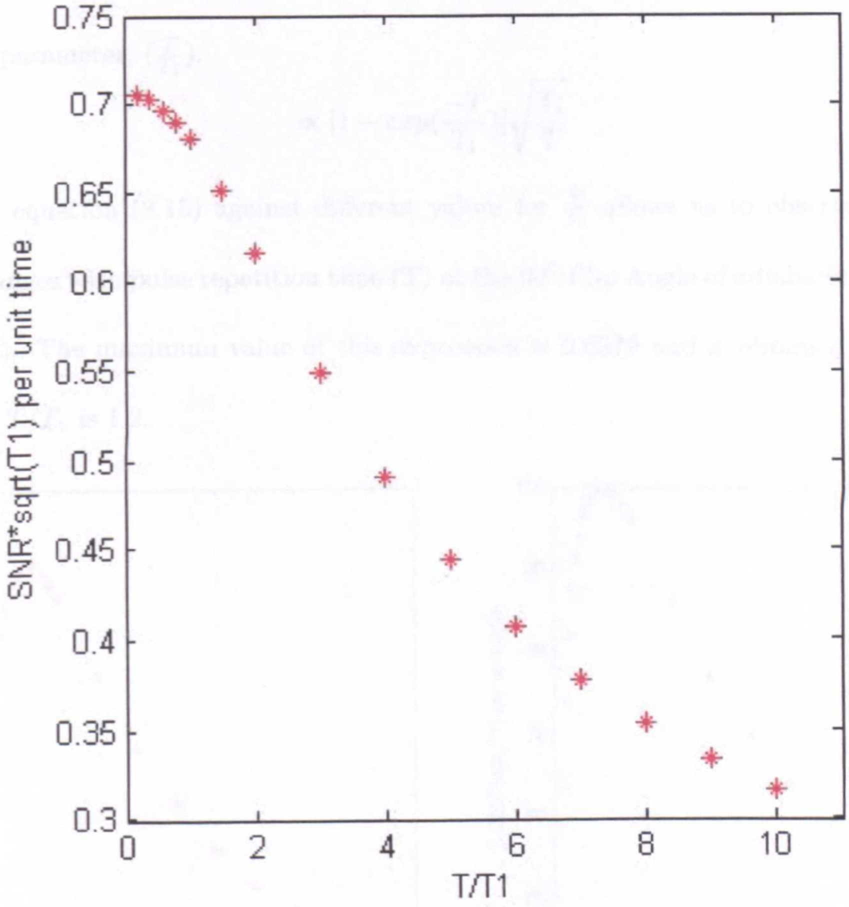

Figure 8.6: Relationship between relative SNR and pulse repetition time at the Ernst Angle.

Maximum signal-to-noise per unit time at 90^0 Flip Angle in Adiabatic Pulse can be derived from Equation (8.9)

$$\propto [1 - exp(\frac{-T}{T_1})]\frac{1}{T^{\frac{1}{2}}} \tag{8.14}$$

If the expression is multiplied by $\sqrt{T_1}$, it can be expressed solely in terms of the dimensionless parameter, $(\frac{T}{T_1})$.

$$\propto [1 - exp(\frac{-T}{T_1})]\sqrt{\frac{T_1}{T}} \tag{8.15}$$

Plotting equation (8.15) against different values for $\frac{T}{T_1}$ allows us to observe how the SNR changes with pulse repetition time (T) at the 90^0 Flip Angle of adiabatic pulse(See Fig. 8.7). The maximum value of this expression is 0.6379 and is obtained when the value of T/T_1 is 1.2.

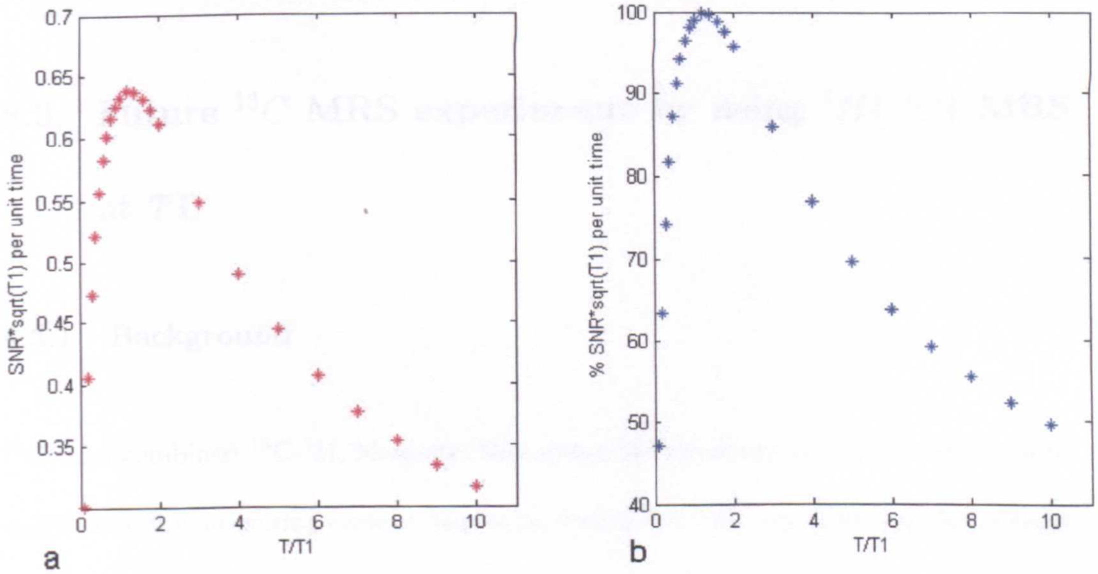

Figure 8.7: Relationship between relative SNR and pulse repetition time at 90^0 Flip Angle (a) and with relative SNR expressed as a percentage of the maximum (b).

Plotting equations (8.13) and (8.15) against different values of T/T_1 allows to compare the relative maximum SNR between the Ernst angle and a 90^0 Flip Angle (See Fig. 8.8). The relative maximum SNR * $sqrt(T_1)$ per unit time for Ernst Angle and 90 degree is 0.7068 and 0.6379 respectively.

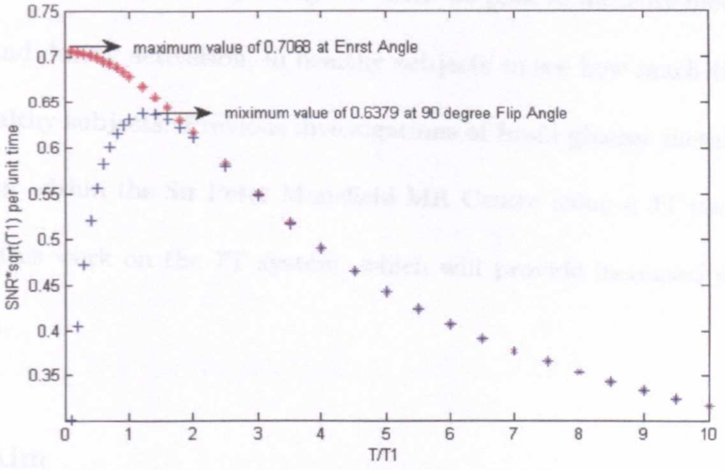

Figure 8.8: Comparison of the effects of repetition time on SNR between an Ernst Angle and 90^0 Flip Angle excitations.

8.3 Future ^{13}C MRS experiments by using $^1H\{^{13}C\}$ MRS at 7T

8.3.1 Background

^{13}C, and combined ^{13}C-^{1}H, Magnetic Resonance Spectroscopy have been shown to be useful tools for measuring various metabolic fluxes[195, 196]. By following the incorporation of ^{13}C labeled substrates (such as glucose or acetate) into different metabolites in the human brain, it is possible to measure metabolic rates including the TCA cycle rate (an important pathway for energy production) and neurotransmitters cycling rates. These rates have been shown to increase in the brain when the brain is performing tasks, requiring more energy. It is thought that perturbed metabolism may be involved in many neurodegenerative diseases. However, currently very little is know about variations in healthy metabolic rates and so little can be inferred by measuring rates in diseased subjects. By using ^{13}C MRS we plan to measure metabolic rates both at rest, and during activation, in healthy subjects to see how much these can vary between healthy subjects. Previous investigations of brain glucose metabolism have been carried out within the Sir Peter Mansfield MR Centre using a 3T magnet. We aim to continue this work on the 7T system, which will provide increased signal and better resolution.

8.3.2 Aim

Future work will:

(1) measure metabolic cycling rates in the human brain including TCA cycle, Glu/Gln cycle.

(2) investigate the feasibility of measuring Gln/GABA cycle rate.

(3) distinguish the cycling rates in neurons and astrocytes separately using [1-^{13}C]glucose and [2-^{13}C]acetate.

8.3.3 Experimental protocol and methods

MRS Protocol: MR scanning will be performed on the Philips Achieva 7T system at the Sir Peter Mansfield Magnetic Resonance Centre. Following a short anatomical MRI, MR spectra will be obtained for measurement of baseline metabolite levels (~10 minutes). Subjects will then be briefly removed from the scanner for the initial bolus of the infusion substrate. Following infusion, subjects will be returned to the magnet and will undergo 40 minutes of repeated, identical ^{13}C scans with pulse-acquire sequence without decoupling while we continue to infuse the substrate. Fig. 8.9 shows the schematic illustrations of the MRS protocol.

Infusion Protocol: To optimise the effectiveness of the measurements, the natural abundance of ^{13}C glucose (a non radioactive isotope) within the body is increased by infusing ^{13}C glucose. An initial bolus of substrate will be infused and then the labeled blood glucose level is maintained using a continuous infusion. Blood glucose and insulin levels will be regularly monitored using arterialised blood obtained from a dorsal foot vein using a hot air heater. This technique has previously been approved by the University of Nottingham Ethics Committee (ETHICS).

Stimulation protocol: Visual stimulation will be delivered during ^{13}C-labelling infusion using a flickering contrast-defined wedges pattern. The paradigm will comprise two 10 minutes stimulation periods interleaved with two 10 minute rest periods. It has previously been used at the Sir Peter Mansfield Magnetic Resonance Centre and has already been safety tested.

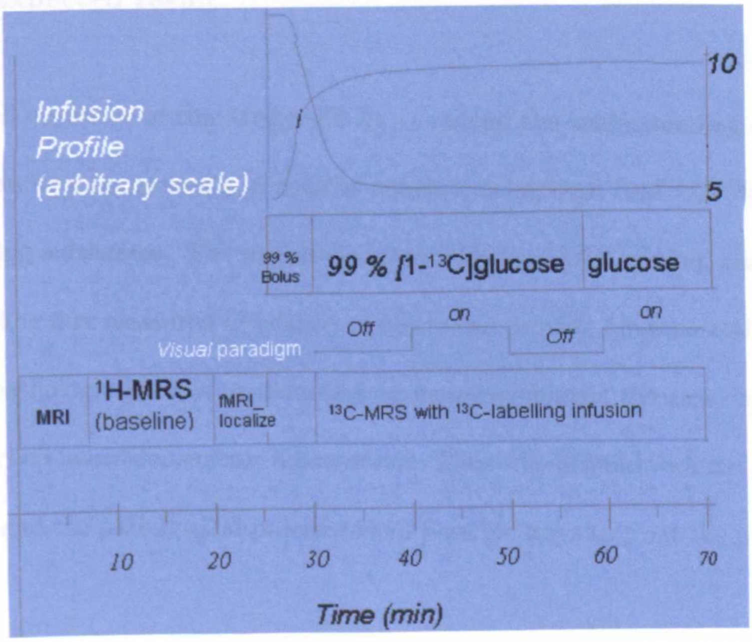

Figure 8.9: Schematic illustrations of MRS protocol

8.3.4 Assessment and analysis

Data Analysis Blood glucose will be measured using a Hemocue (HemoCue Ltd, Sheffield, UK) glucose analyzer, and the results will be used to adjust the rate of supply of labeled glucose that was infused through an antecubital vein on the left forearm after acquisition of 10 $\sim$ 15 min of baseline ^{13}C spectra. MR spectra will be analysed by post-processing in jMRUI and metabolite levels will be calculated using LCModel. Segmentation within the voxel will be carried out using matlab programme to assess the tissue to allow calculation of absolute metabolite concentrations. The time course of ^{13}C label incorporation in brain amino acids will be measured in occipital cortex during infusion of ^{13}C-labelling substrates and then be fitted using a 2-compartment metabolic model to determine CMRglc(ox), TCA cycle rate and neurotransmitter cycling rate.

8.3.5 Expected result

The overall objective of this study will be to extend the understanding of energy and neurotransmitter homeostasis in healthy subjects using high field $^{1}H\{^{13}C\}$ MRS with ^{13}C-labelling substrates. The metabolic rates including TCA cycling and neurotransmitter cycling flux measured in healthy subjects can provide fundamental and valuable basis for pathologic process or disorders in neuropsychiatric diseases, which thought have disturbed neurotransmitter homeostasis. Thus, the groundwork for increased understanding of the pathological processes and possible ways to treat the process can be obtained.

Chapter 9

Conclusions

The main objective of this thesis was to investigate metabolic changes in human visual cortex under visual stimulation. Particular emphasis was placed on assessing the oxidative metabolism, excitatory neurotransmitter cycling and GSH synthesis during brain activation. This work was presented in May 2010 at the International Society for Magnetic Resonance in Medicine (ISMRM), in Sweden (Stockholm) and in May 2011 at ISMRM in Canada (Montreal). The main conclusions draw from this research are outlined below.

Our initial functional ^{1}H-MRS study at 7T, using Light Emitting Diode (LED) goggles, found increased Glu (2% ± 1%) and decreased Asp (19% ± 13%) during two 9.9-min stimulation paradigms, which is consistent with previous reports and suggests a stimulus driven increase in oxidative energy metabolism. Furthermore, decreased Gln (6% ± 3%) was also found during stimulation. Increased Glu and decreased Gln might indicate an increase in excitatory neurotransmitter cycling in the visual cortex during stimulation.

Since metabolite changes observed due to visual stimulation were relatively small, we decided to use a long, intense visual stimulus, designed to retain attention, to try to elicit maximal changes in ^{1}H metabolites during stimulation. The stimulus consisted of contrast-defined wedges, moving towards or away from the fixation cross, and have been shown to lead to less neural adaptation over time compared to a checkerboard[137]. Two different stimulation paradigms, were designed to confirm and quantify the changes in the levels of Glu, GABA, Gln, Glc, Lac and Asp and to investigate the time course of post-stimulus recovery. Many more metabolite changes during the two different time scales of stimulation were observed in these experiments. In good agreement with previous results, during a 13.2-min stimulation period, Glu was found to be significantly increased by $2\% \pm 1\%$ (equivalent to 0.22 $\mu mol/g$, p=0.011), Asp decreased by $9\% \pm 8\%$ (equivalent to 0.32 $\mu mol/g$, p=0.038), Lac increased by $10\% \pm 6\%$ (equivalent to 0.1 $\mu mol/g$, p=0.044), and Glc showed a tendency to decrease by $22\% \pm 18\%$ (equivalent to 0.4 $\mu mol/g$, but did not reach statistical significance because of a higher SD). However, the significant increase in Lac is only evident in the early 6.6-min of activation, with increases up to as much as $26\% \pm 7\%$ (approximate 0.2 $\mu mol/g$). No significant Lac accumulation could be observed in the later 6.6-min prolonged stimulation. Interestingly, the brain GSH concentration was found to be elevated by $7\% \pm 4\%$ (equivalent to 0.17 $\mu mol/g$, p=0.021) during 13.2-min of neuronal activation, in parallel with decreased brain Gln and Gly, by $8\% \pm 5\%$ (equivalent to 0.18 $\mu mol/g$, p=0.038) and $11\% \pm 6\%$ (equivalent to 0.20 $\mu mol/g$, p=0.015), respectively. All the metabolite levels, perturbed due to stimulation, normalized to baseline level during a 20 minute recovery period. Consistent metabolite changes have also been observed in the second experiment involved two periods of stimulation (9.9 min duration) interleaved with two 9.9-min rest periods. The response of Glu, Gln, GSH, Gly, Asp during the second 9.9 min stimulation were comparable to those observed in the initial 9.9 min stimulation, But Lac, did not show significant change in the second 9.9 min stimulation. The analyzed time courses of changed metabolites exhibited good agreement during the two different functional sessions. GABA showed *a tendency to increase* throughout 13.2 min of stimulation and the two 9.9 min stimulations, but did not reach significance. The observed decrease of Glc with elevated Lac in response to visual stimulation indicates an increased energy metabolism. Opposite changes in Glu and Asp during visual stimulation might suggest an increase in malate-aspartate shuttle (MAS)activity, to maintain the cytosolic redox potential $NADH/NAD^+$, due to the sustained neuronal activation. Our observations of increased Glu with decreased Gln in the visual cortex during stimulation indicate a stimulus driven increase in excitatory neurotransmitter cycling. The elevated GSH in the visual cortex in response to visual stimulation is a new observation. Possible reasons for the elevated GSH in the visual cortex during stimulation include detoxification of reactive oxygen species (ROS) or clearance of the increased glutamate, generated during the intense neuronal activation. Gly is also a precursor of GSH and a decrease on activation is consistent with increased GSH synthesis. On the basis of these results acquired from the visual cortex throughout two different stimulation paradigms, we propose an increase in oxidative metabolism, excitatory neurotransmitter cycling and GSH synthesis, possible related to glutamate clearance and ROS detoxification.

Given that the Lac response was confined to the first visual stimulus, further repeated visual stimulation paradigm were designed, varying the duration of first stimulation , to see the effect on the Lac response during the second visual stimulation period. The short term initial stimulation did not inhibit the Lac response under the second prolonged stimulation. With the increase in the first visual stimulus duration, the Lac response was slightly diminished. When the initial stimulation periods was increased up to 288s, no significant Lac response can be evident under the second stimulation periods, and its averaged Lac level was significantly below baseline after cessation of the first stimulus. It is possible that the increased glycolytic flux would still continue for a while during recovery from stimulation, accounting for the decreased brain Lac level during resting periods from stimulation .

Chapter 10

Appendix

$$\frac{d[\alpha KG_4]}{dt} = V_{TCA}\frac{[L_3]}{[L]} + V_X\frac{[Glu_4]}{[Glu]} - (V_{TCA} + V_X)\frac{[\alpha KG_4]}{[\alpha KG]} \tag{10.1}$$

$$\frac{d[\alpha KG_3]}{dt} = V_{TCA}\frac{[OAA_2]}{[OAA]} + V_X\frac{[Glu_3]}{[Glu]} - (V_{TCA} + V_X)\frac{[\alpha KG_3]}{[\alpha KG]} \tag{10.2}$$

$$\frac{d[\alpha KG_2]}{dt} = V_{TCA}\frac{[OAA_3]}{[OAA]} + V_X\frac{[Glu_2]}{[Glu]} - (V_{TCA} + V_X)\frac{[\alpha KG_2]}{[\alpha KG]} \tag{10.3}$$

$$\frac{d[Glu_4]}{dt} = V_X\frac{[\alpha KG_4]}{[\alpha KG]} - (V_X + V_{cycle})\frac{[Glu_4]}{[Glu]} + V_{Gln}\frac{[Gln_4]}{[Gln]} \tag{10.4}$$

$$\frac{d[Glu_3]}{dt} = V_X\frac{[\alpha KG_3]}{[\alpha KG]} - (V_X + V_{cycle})\frac{[Glu_3]}{[Glu]} + V_{Gln}\frac{[Gln_3]}{[Gln]} \tag{10.5}$$

$$\frac{d[Glu_2]}{dt} = V_X \frac{[\alpha KG_2]}{[\alpha KG]} - (V_X + V_{cycle})\frac{[Glu_2]}{[Glu]} + V_{Gln}\frac{[Gln_2]}{[Gln]} \tag{10.6}$$

$$\frac{d[Gln_4]}{dt} = V_{Gln}\frac{[Glu_4]}{[Glu]} - (V_{efflux} + V_{cycle})\frac{[Gln_4]}{[Gln]} \tag{10.7}$$

$$\frac{d[Gln_3]}{dt} = V_{Gln}\frac{[Glu_3]}{[Glu]} - (V_{efflux} + V_{cycle})\frac{[Gln_3]}{[Gln]} \tag{10.8}$$

$$\frac{d[Gln_2]}{dt} = V_{Gln}\frac{[Glu_2]}{[Glu]} - (V_{efflux} + V_{cycle})\frac{[Gln_2]}{[Gln]} \tag{10.9}$$

$$\frac{d[Asp_3]}{dt} = V_X(\frac{[OAA_3]}{[OAA]} - \frac{[Asp_3]}{[Asp]}) \tag{10.10}$$

$$\frac{d[Asp_2]}{dt} = V_X(\frac{[OAA_2]}{[OAA]} - \frac{[Asp_2]}{[Asp]}) \tag{10.11}$$

$$\frac{d[OAA_3]}{dt} = \frac{1}{2}V_{TCA}(\frac{[\alpha KG_4] + [\alpha KG_3]}{[\alpha KG]}) + V_X\frac{[Asp_3]}{[Asp]} - (V_{TAC} + V_X)\frac{[OAA_3]}{[OAA]} \tag{10.12}$$

$$\frac{d[OAA_2]}{dt} = \frac{1}{2}V_{TCA}(\frac{[\alpha KG_4] + [\alpha KG_3]}{[\alpha KG]}) + V_X\frac{[Asp_2]}{[Asp]} - (V_{TAC} + V_X)\frac{[OAA_2]}{[OAA]} \tag{10.13}$$

$$V_{PDH} = V_{TCA} \tag{10.14}$$

Bibliography

[1] I. Tkc, P. Andersen, G. Adriany, H. Merkle, K. Ugurbil, and R. Gruetter, "In vivo 1h nmr spectroscopy of the human brain at 7 t.," *Magn Reson Med*, vol. 46, pp. 451–456, Sep 2001.

[2] R. Mekle, V. Mlynrik, G. Gambarota, M. Hergt, G. Krueger, and R. Gruetter, "Mr spectroscopy of the human brain with enhanced signal intensity at ultrashort echo times on a clinical platform at 3t and 7t.," *Magn Reson Med*, vol. 61, pp. 1279–1285, Jun 2009.

[3] P. T. Fox and M. E. Raichle, "Focal physiological uncoupling of cerebral blood flow and oxidative metabolism during somatosensory stimulation in human subjects.," *Proc Natl Acad Sci U S A*, vol. 83, pp. 1140–1144, Feb 1986.

[4] P. T. Fox, M. E. Raichle, M. A. Mintun, and C. Dence, "Nonoxidative glucose consumption during focal physiologic neural activity.," *Science*, vol. 241, pp. 462–464, Jul 1988.

[5] W. Chen, E. J. Novotny, X. H. Zhu, D. L. Rothman, and R. G. Shulman, "Localized 1h nmr measurement of glucose consumption in the human brain during visual stimulation.," *Proc Natl Acad Sci U S A*, vol. 90, pp. 9896–9900, Nov 1993.

[6] J. Frahm, G. Krger, K. D. Merboldt, and A. Kleinschmidt, "Dynamic uncoupling and recoupling of perfusion and oxidative metabolism during focal brain activation in man.," *Magn Reson Med*, vol. 35, pp. 143–148, Feb 1996.

[7] K. D. Merboldt, H. Bruhn, W. Hnicke, T. Michaelis, and J. Frahm, "Decrease of glucose in the human visual cortex during photic stimulation.," *Magn Reson Med*, vol. 25, pp. 187–194, May 1992.

[8] F. Giove, S. Mangia, M. Bianciardi, G. Garreffa, F. D. Salle, R. Morrone, and B. Maraviglia, "The physiology and metabolism of neuronal activation: in vivo studies by nmr and other methods.," *Magn Reson Imaging*, vol. 21, pp. 1283–1293, Dec 2003.

[9] R. G. Shulman, F. Hyder, and D. L. Rothman, "Lactate efflux and the neuroenergetic basis of brain function.," *NMR Biomed*, vol. 14, no. 7-8, pp. 389–396, 2001.

[10] H. R. Zielke, C. L. Zielke, and P. J. Baab, "Oxidation of (14)c-labeled compounds perfused by microdialysis in the brains of free-moving rats.," *J Neurosci Res*, vol. 85, pp. 3145–3149, Nov 2007.

[11] Y. Hu and G. S. Wilson, "A temporary local energy pool coupled to neuronal activity: fluctuations of extracellular lactate levels in rat brain monitored with rapid-response enzyme-based sensor.," *J Neurochem*, vol. 69, pp. 1484–1490, Oct 1997.

[12] J.-P. Revelly, L. Tappy, A. Martinez, M. Bollmann, M.-C. Cayeux, M. M. Berger, and R. L. Chiolro, "Lactate and glucose metabolism in severe sepsis and cardiogenic shock.," *Crit Care Med*, vol. 33, pp. 2235–2240, Oct 2005.

[13] H. S. Waagepetersen, I. J. Bakken, O. M. Larsson, U. Sonnewald, and A. Schousboe, "Comparison of lactate and glucose metabolism in cultured neocortical neurons and astrocytes using 13c-nmr spectroscopy.," *Dev Neurosci*, vol. 20, no. 4-5, pp. 310–320, 1998.

[14] T. M. Bliss and R. M. Sapolsky, "Interactions among glucose, lactate and adenosine regulate energy substrate utilization in hippocampal cultures.," *Brain Res*, vol. 899, pp. 134–141, Apr 2001.

[15] A. Schurr, "Lactate: the ultimate cerebral oxidative energy substrate?," *J Cereb Blood Flow Metab*, vol. 26, pp. 142–152, Jan 2006.

[16] A. Schurr and R. S. Payne, "Lactate, not pyruvate, is neuronal aerobic glycolysis end product: an in vitro electrophysiological study.," *Neuroscience*, vol. 147, pp. 613–619, Jul 2007.

[17] J. Prichard, D. Rothman, E. Novotny, O. Petroff, T. Kuwabara, M. Avison, A. Howseman, C. Hanstock, and R. Shulman, "Lactate rise detected by 1h nmr in human visual cortex during physiologic stimulation.," *Proc Natl Acad Sci U S A*, vol. 88, pp. 5829–5831, Jul 1991.

[18] D. Sappey-Marinier, G. Calabrese, G. Fein, J. W. Hugg, C. Biggins, and M. W. Weiner, "Effect of photic stimulation on human visual cortex lactate and phosphates using 1h and 31p magnetic resonance spectroscopy.," *J Cereb Blood Flow Metab*, vol. 12, pp. 584–592, Jul 1992.

[19] C. C. Boucard, J. P. Mostert, F. W. Cornelissen, J. D. Keyser, M. Oudkerk, and P. E. Sijens, "Visual stimulation, 1h mr spectroscopy and fmri of the human visual pathways.," *Eur Radiol*, vol. 15, pp. 47–52, Jan 2005.

[20] S. Mangia, G. Garreffa, M. Bianciardi, F. Giove, F. D. Salle, and B. Maraviglia, "The aerobic brain: lactate decrease at the onset of neural activity.," *Neuroscience*, vol. 118, no. 1, pp. 7–10, 2003.

[21] S. Mangia, I. Tkc, R. Gruetter, P.-F. V. D. Moortele, F. Giove, B. Maraviglia, and K. Uaurbil, "Sensitivity of single-voxel 1h-mrs in investigating the metabolism of the activated human visual cortex at 7 t.," *Magn Reson Imaging*, vol. 24, pp. 343–348, May 2006.

[22] S. Mangia, I. Tkc, N. K. Logothetis, R. Gruetter, P.-F. V. de Moortele, and K. Uaurbil, "Dynamics of lactate concentration and blood oxygen level-dependent effect in the human visual cortex during repeated identical stimuli.," *J Neurosci Res*, vol. 85, pp. 3340–3346, Nov 2007.

[23] S. Mangia, I. Tkc, R. Gruetter, P.-F. V. de Moortele, B. Maraviglia, and K. Uaurbil, "Sustained neuronal activation raises oxidative metabolism to a new steady-state level: evidence from 1h nmr spectroscopy in the human visual cortex.," *J Cereb Blood Flow Metab*, vol. 27, pp. 1055–1063, May 2007.

[24] R. G. Shulman and D. L. Rothman, "Interpreting functional imaging studies in terms of neurotransmitter cycling.," *Proc Natl Acad Sci U S A*, vol. 95, pp. 11993–11998, Sep 1998.

[25] A. B. Patel, R. A. de Graaf, G. F. Mason, T. Kanamatsu, D. L. Rothman, R. G. Shulman, and K. L. Behar, "Glutamatergic neurotransmission and neuronal glucose oxidation are coupled during intense neuronal activation.," *J Cereb Blood Flow Metab*, vol. 24, pp. 972–985, Sep 2004.

[26] I.-Y. Choi, H. Lei, and R. Gruetter, "Effect of deep pentobarbital anesthesia on neurotransmitter metabolism in vivo: on the correlation of total glucose consump-

tion with glutamatergic action.," *J Cereb Blood Flow Metab*, vol. 22, pp. 1343–1351, Nov 2002.

[27] R. A. de Graaf, G. F. Mason, A. B. Patel, D. L. Rothman, and K. L. Behar, "Regional glucose metabolism and glutamatergic neurotransmission in rat brain in vivo.," *Proc Natl Acad Sci U S A*, vol. 101, pp. 12700–12705, Aug 2004.

[28] G. Oz, D. A. Berkich, P.-G. Henry, Y. Xu, K. LaNoue, S. M. Hutson, and R. Gruetter, "Neuroglial metabolism in the awake rat brain: Co2 fixation increases with brain activity.," *J Neurosci*, vol. 24, pp. 11273–11279, Dec 2004.

[29] L. Pellerin, "Lactate as a pivotal element in neuron-glia metabolic cooperation.," *Neurochem Int*, vol. 43, no. 4-5, pp. 331–338, 2003.

[30] N. R. Sibson, A. Dhankhar, G. F. Mason, D. L. Rothman, K. L. Behar, and R. G. Shulman, "Stoichiometric coupling of brain glucose metabolism and glutamatergic neuronal activity.," *Proc Natl Acad Sci U S A*, vol. 95, pp. 316–321, Jan 1998.

[31] P.-G. Henry, G. Adriany, D. Deelchand, R. Gruetter, M. Marjanska, G. Oz, E. R. Seaquist, A. Shestov, and K. U?urbil, "In vivo 13c nmr spectroscopy and metabolic modeling in the brain: a practical perspective.," *Magn Reson Imaging*, vol. 24, pp. 527–539, May 2006.

[32] R. S. Badar-Goffer, H. S. Bachelard, and P. G. Morris, "Cerebral metabolism of acetate and glucose studied by 13c-n.m.r. spectroscopy. a technique for investigating metabolic compartmentation in the brain.," *Biochem J*, vol. 266, pp. 133–139, Feb 1990.

[33] N. Chhina, E. Kuestermann, J. Halliday, L. J. Simpson, I. A. Macdonald, H. S. Bachelard, and P. G. Morris, "Measurement of human tricarboxylic acid cycle

rates during visual activation by (13)c magnetic resonance spectroscopy.," *J Neurosci Res*, vol. 66, pp. 737–746, Dec 2001.

[34] P. Morris and H. Bachelard, "Reflections on the application of 13c-mrs to research on brain metabolism.," *NMR Biomed*, vol. 16, no. 6-7, pp. 303–312, 2003.

[35] I. L. Doerr and J. J. Fox, "Nucleosides. xl. the introduction of a 2,3'-imino bridge into pyrimidine nucleosides.," *J Am Chem Soc*, vol. 89, pp. 1760–1761, Mar 1967.

[36] P. Jezzard, S. Duewell, and R. S. Balaban, "Mr relaxation times in human brain: measurement at 4 t.," *Radiology*, vol. 199, pp. 773–779, Jun 1996.

[37] S. Majumdar, A. Gmitro, S. C. Orphanoudakis, D. Reddy, and J. C. Gore, "An estimation and correction scheme for system imperfections in multiple-echo magnetic resonance imaging.," *Magn Reson Med*, vol. 4, pp. 203–220, Mar 1987.

[38] V. Govindaraju, K. Young, and A. A. Maudsley, "Proton nmr chemical shifts and coupling constants for brain metabolites.," *NMR Biomed*, vol. 13, pp. 129–153, May 2000.

[39] O. Gonen, S. Gruber, B. S. Li, V. Mlynrik, and E. Moser, "Multivoxel 3d proton spectroscopy in the brain at 1.5 versus 3.0 t: signal-to-noise ratio and resolution comparison.," *AJNR Am J Neuroradiol*, vol. 22, pp. 1727–1731, Oct 2001.

[40] P. B. Barker, D. O. Hearshen, and M. D. Boska, "Single-voxel proton mrs of the human brain at 1.5t and 3.0t.," *Magn Reson Med*, vol. 45, pp. 765–769, May 2001.

[41] A. D. Costanzo, F. Trojsi, M. Tosetti, T. Schirmer, S. M. Lechner, T. Popolizio, and T. Scarabino, "Proton mr spectroscopy of the brain at 3 t: an update.," *Eur Radiol*, vol. 17, pp. 1651–1662, Jul 2007.

[42] J. A. de Zwart, P. J. Ledden, P. van Gelderen, J. Bodurka, R. Chu, and J. H. Duyn, "Signal-to-noise ratio and parallel imaging performance of a 16-channel receive-only brain coil array at 3.0 tesla.," *Magn Reson Med*, vol. 51, pp. 22–26, Jan 2004.

[43] H. P. Hetherington, J. W. Pan, W. J. Chu, G. F. Mason, and B. R. Newcomer, "Biological and clinical mrs at ultra-high field.," *NMR Biomed*, vol. 10, pp. 360–371, Dec 1997.

[44] R. Gruetter, S. A. Weisdorf, V. Rajanayagan, M. Terpstra, H. Merkle, C. L. Truwit, M. Garwood, S. L. Nyberg, and K. U?urbil, "Resolution improvements in in vivo 1h nmr spectra with increased magnetic field strength.," *J Magn Reson*, vol. 135, pp. 260–264, Nov 1998.

[45] R. Bartha, D. J. Drost, R. S. Menon, and P. C. Williamson, "Comparison of the quantification precision of human short echo time (1)h spectroscopy at 1.5 and 4.0 tesla.," *Magn Reson Med*, vol. 44, pp. 185–192, Aug 2000.

[46] S. Gruber, V. Mlynrik, and E. Moser, "High-resolution 3d proton spectroscopic imaging of the human brain at 3 t: Snr issues and application for anatomy-matched voxel sizes.," *Magn Reson Med*, vol. 49, pp. 299–306, Feb 2003.

[47] B. S. Li, J. Regal, and O. Gonen, "Snr versus resolution in 3d 1h mrs of the human brain at high magnetic fields.," *Magn Reson Med*, vol. 46, pp. 1049–1053, Dec 2001.

[48] R. Frayne, B. G. Goodyear, P. Dickhoff, M. L. Lauzon, and R. J. Sevick, "Magnetic resonance imaging at 3.0 tesla: challenges and advantages in clinical neurological imaging.," *Invest Radiol*, vol. 38, pp. 385–402, Jul 2003.

[49] H. P. Hetherington, J. W. Pan, G. F. Mason, D. Adams, M. J. Vaughn, D. B. Twieg, and G. M. Pohost, "Quantitative 1h spectroscopic imaging of human brain at 4.1 t using image segmentation.," *Magn Reson Med*, vol. 36, pp. 21–29, Jul 1996.

[50] J. W. Pan, G. F. Mason, G. M. Pohost, and H. P. Hetherington, "Spectroscopic imaging of human brain glutamate by water-suppressed j-refocused coherence transfer at 4.1 t.," *Magn Reson Med*, vol. 36, pp. 7–12, Jul 1996.

[51] A. D. Costanzo, F. Trojsi, M. Tosetti, G. M. Giannatempo, F. Nemore, M. Piccirillo, S. Bonavita, G. Tedeschi, and T. Scarabino, "High-field proton mrs of human brain.," *Eur J Radiol*, vol. 48, pp. 146–153, Nov 2003.

[52] F. A. Howe, R. J. Maxwell, D. E. Saunders, M. M. Brown, and J. R. Griffiths, "Proton spectroscopy in vivo.," *Magn Reson Q*, vol. 9, pp. 31–59, Mar 1993.

[53] P. C. V. Zijl and P. B. Barker, "Magnetic resonance spectroscopy and spectroscopic imaging for the study of brain metabolism.," *Ann N Y Acad Sci*, vol. 820, pp. 75–96, May 1997.

[54] H. Bruhn, J. Frahm, M. L. Gyngell, K. D. Merboldt, W. Hnicke, and R. Sauter, "Cerebral metabolism in man after acute stroke: new observations using localized proton nmr spectroscopy.," *Magn Reson Med*, vol. 9, pp. 126–131, Jan 1989.

[55] C. Majs, M. Juli-Sap, J. Alonso, M. Serrallonga, C. Aguilera, J. J. Acebes, C. Ars, and J. Gili, "Brain tumor classification by proton mr spectroscopy: comparison of diagnostic accuracy at short and long te.," *AJNR Am J Neuroradiol*, vol. 25, no. 10, pp. 1696–1704, 2004.

[56] H. B. Larsson, P. Christiansen, M. Jensen, J. Frederiksen, A. Heltberg, J. Olesen, and O. Henriksen, "Localized in vivo proton spectroscopy in the brain of patients with multiple sclerosis.," *Magn Reson Med*, vol. 22, pp. 23–31, Nov 1991.

[57] P. J. Pouwels and J. Frahm, "Regional metabolite concentrations in human brain as determined by quantitative localized proton mrs.," *Magn Reson Med*, vol. 39, pp. 53–60, Jan 1998.

[58] J. W. Pan, D. B. Twieg, and H. P. Hetherington, "Quantitative spectroscopic imaging of the human brain.," *Magn Reson Med*, vol. 40, pp. 363–369, Sep 1998.

[59] J. Frahm, T. Michaelis, K. D. Merboldt, W. Hnicke, M. L. Gyngell, and H. Bruhn, "On the n-acetyl methyl resonance in localized 1h nmr spectra of human brain in vivo.," *NMR Biomed*, vol. 4, pp. 201–204, Aug 1991.

[60] T. Wallimann, M. Wyss, D. Brdiczka, K. Nicolay, and H. M. Eppenberger, "Intracellular compartmentation, structure and function of creatine kinase isoenzymes in tissues with high and fluctuating energy demands: the 'phosphocreatine circuit' for cellular energy homeostasis.," *Biochem J*, vol. 281 (Pt 1), pp. 21–40, Jan 1992.

[61] R. J. Gillies and D. L. Morse, "In vivo magnetic resonance spectroscopy in cancer.," *Annu Rev Biomed Eng*, vol. 7, pp. 287–326, 2005.

[62] M. J. Firbank, R. M. Harrison, and J. T. O'Brien, "A comprehensive review of proton magnetic resonance spectroscopy studies in dementia and parkinson's disease.," *Dement Geriatr Cogn Disord*, vol. 14, no. 2, pp. 64–76, 2002.

[63] P. A. Narayana, "Magnetic resonance spectroscopy in the monitoring of multiple sclerosis.," *J Neuroimaging*, vol. 15, no. 4 Suppl, pp. 46S–57S, 2005.

[64] K. L. Malisza, P. Kozlowski, and J. Peeling, "A review of in vivo 1h magnetic resonance spectroscopy of cerebral ischemia in rats.," *Biochem Cell Biol*, vol. 76, no. 2-3, pp. 487–496, 1998.

[65] D. Attwell and S. B. Laughlin, "An energy budget for signaling in the grey matter of the brain.," *J Cereb Blood Flow Metab*, vol. 21, pp. 1133–1145, Oct 2001.

[66] A. Schousboe, N. Westergaard, H. S. Waagepetersen, O. M. Larsson, I. J. Bakken, and U. Sonnewald, "Trafficking between glia and neurons of tca cycle intermediates and related metabolites.," *Glia*, vol. 21, pp. 99–105, Sep 1997.

[67] M. C. McKenna, "The glutamate-glutamine cycle is not stoichiometric: fates of glutamate in brain.," *J Neurosci Res*, vol. 85, pp. 3347–3358, Nov 2007.

[68] F. Schubert, F. Seifert, C. Elster, A. Link, M. Walzel, S. Mientus, J. Haas, and H. Rinneberg, "Serial 1h-mrs in relapsing-remitting multiple sclerosis: effects of interferon-beta therapy on absolute metabolite concentrations.," *MAGMA*, vol. 14, pp. 213–222, Jun 2002.

[69] E. P. Pioro, "Mr spectroscopy in amyotrophic lateral sclerosis/motor neuron disease.," *J Neurol Sci*, vol. 152 Suppl 1, pp. S49–S53, Oct 1997.

[70] R. Hurd, N. Sailasuta, R. Srinivasan, D. B. Vigneron, D. Pelletier, and S. J. Nelson, "Measurement of brain glutamate using te-averaged press at 3t.," *Magn Reson Med*, vol. 51, pp. 435–440, Mar 2004.

[71] P. J. Pouwels and J. Frahm, "Regional metabolite concentrations in human brain as determined by quantitative localized proton mrs.," *Magn Reson Med*, vol. 39, pp. 53–60, Jan 1998.

[72] N. R. Sibson, A. Dhankhar, G. F. Mason, K. L. Behar, D. L. Rothman, and R. G. Shulman, "In vivo 13c nmr measurements of cerebral glutamine synthesis

as evidence for glutamate-glutamine cycling.," *Proc Natl Acad Sci U S A*, vol. 94, pp. 2699–2704, Mar 1997.

[73] R. Dringen and J. Hirrlinger, "Glutathione pathways in the brain.," *Biol Chem*, vol. 384, pp. 505–516, Apr 2003.

[74] R. Cruz, W. A. Melian, and J. A. B. Rosado, "[glutathione in cognitive function and neurodegeneration]," *Rev Neurol*, vol. 36, no. 9, pp. 877–886, 2003.

[75] A. Chi, A. Cucatto, A. A. Terreni, and D. Schiffer, "Reduced glutathione in amyotrophic lateral sclerosis: an open, crossover, randomized trial.," *Ital J Neurol Sci*, vol. 19, pp. 363–366, Dec 1998.

[76] J. Via, A. Lloret, R. Ort, and D. Alonso, "Molecular bases of the treatment of alzheimer's disease with antioxidants: prevention of oxidative stress.," *Mol Aspects Med*, vol. 25, no. 1-2, pp. 117–123, 2004.

[77] Dringen, "Glutathione metabolism and oxidative stress in neurodegeneration," *Eur J Biochem*, vol. 267, p. 4903, Aug 2000.

[78] P. A. Bottomley, "Spatial localization in nmr spectroscopy in vivo.," *Ann N Y Acad Sci*, vol. 508, pp. 333–348, 1987.

[79] I. Tkc, Z. Starcuk, I. Y. Choi, and R. Gruetter, "In vivo 1h nmr spectroscopy of rat brain at 1 ms echo time.," *Magn Reson Med*, vol. 41, pp. 649–656, Apr 1999.

[80] F. Schick, T. Ngele, U. Klose, and O. Lutz, "Lactate quantification by means of press spectroscopy–influence of refocusing pulses and timing scheme.," *Magn Reson Imaging*, vol. 13, no. 2, pp. 309–319, 1995.

[81] D. A. Kelley, L. L. Wald, and J. M. Star-Lack, "Lactate detection at 3t: compensating j coupling effects with basing.," *J Magn Reson Imaging*, vol. 9, pp. 732–737, May 1999.

[82] J. W. van Der Veen, D. R. Weinberger, G. Tedeschi, J. A. Frank, and J. H. Duyn, “Proton mr spectroscopic imaging without water suppression.,” *Radiology*, vol. 217, pp. 296–300, Oct 2000.

[83] D. B. Clayton, M. A. Elliott, J. S. Leigh, and R. E. Lenkinski, “1h spectroscopy without solvent suppression: characterization of signal modulations at short echo times.,” *J Magn Reson*, vol. 153, pp. 203–209, Dec 2001.

[84] A. Haase, J. Frahm, W. Hnicke, and D. Matthaei, “1h nmr chemical shift selective (chess) imaging.,” *Phys Med Biol*, vol. 30, pp. 341–344, Apr 1985.

[85] P.-F. V. de Moortele, J. Pfeuffer, G. H. Glover, K. Ugurbil, and X. Hu, “Respiration-induced b0 fluctuations and their spatial distribution in the human brain at 7 tesla.,” *Magn Reson Med*, vol. 47, pp. 888–895, May 2002.

[86] A. Naressi, C. Couturier, J. M. Devos, M. Janssen, C. Mangeat, R. de Beer, and D. Graveron-Demilly, “Java-based graphical user interface for the mrui quantitation package.,” *MAGMA*, vol. 12, pp. 141–152, May 2001.

[87] A. Naressi, C. Couturier, I. Castang, R. de Beer, and D. Graveron-Demilly, “Java-based graphical user interface for mrui, a software package for quantitation of in vivo/medical magnetic resonance spectroscopy signals.,” *Comput Biol Med*, vol. 31, pp. 269–286, Jul 2001.

[88] T. Jao, C.-Y. Chang, C.-W. Li, D.-Y. Chen, E. Wu, C.-W. Wu, C.-H. Tsou, C.-C. Ho, and J.-H. Chen, “Development of ntu standard chinese brain template: morphologic and functional comparison with mni template using magnetic resonance imaging.,” *Conf Proc IEEE Eng Med Biol Soc*, vol. 2009, pp. 4779–4782, 2009.

[89] T. Laudadio, N. Mastronardi, L. Vanhamme, P. V. Hecke, and S. V. Huffel, "Improved lanczos algorithms for blackbox mrs data quantitation.," *J Magn Reson*, vol. 157, pp. 292–297, Aug 2002.

[90] B. S. Y. Li, H. Wang, and O. Gonen, "Metabolite ratios to assumed stable creatine level may confound the quantification of proton brain mr spectroscopy.," *Magn Reson Imaging*, vol. 21, pp. 923–928, Oct 2003.

[91] Hass, Tamor, Anthony, and Banholzer, "Lattice dynamics and raman spectra of isotopically mixed diamond.," *Phys Rev B Condens Matter*, vol. 45, pp. 7171–7182, Apr 1992.

[92] M. Krssak, K. F. Petersen, R. Bergeron, T. Price, D. Laurent, D. L. Rothman, M. Roden, and G. I. Shulman, "Intramuscular glycogen and intramyocellular lipid utilization during prolonged exercise and recovery in man: a 13c and 1h nuclear magnetic resonance spectroscopy study.," *J Clin Endocrinol Metab*, vol. 85, pp. 748–754, Feb 2000.

[93] J. Rico-Sanz, M. Moosavi, E. L. Thomas, J. McCarthy, G. A. Coutts, N. Saeed, and J. D. Bell, "In vivo evaluation of the effects of continuous exercise on skeletal muscle triglycerides in trained humans.," *Lipids*, vol. 35, pp. 1313–1318, Dec 2000.

[94] K. Brechtel, A. M. Niess, J. Machann, K. Rett, F. Schick, C. D. Claussen, H. H. Dickhuth, H. U. Haering, and S. Jacob, "Utilisation of intramyocellular lipids (imcls) during exercise as assessed by proton magnetic resonance spectroscopy (1h-mrs).," *Horm Metab Res*, vol. 33, pp. 63–66, Feb 2001.

[95] J. Dcombaz, M. Fleith, H. Hoppeler, R. Kreis, and C. Boesch, "Effect of diet on the replenishment of intramyocellular lipids after exercise.," *Eur J Nutr*, vol. 39,

pp. 244–247, Dec 2000.

[96] S. R. Stannard, M. W. Thompson, K. Fairbairn, B. Huard, T. Sachinwalla, and C. H. Thompson, "Fasting for 72 h increases intramyocellular lipid content in nondiabetic, physically fit men.," *Am J Physiol Endocrinol Metab*, vol. 283, pp. E1185–E1191, Dec 2002.

[97] R. Gruetter, G. Adriany, I.-Y. Choi, P.-G. Henry, H. Lei, and G. Oz, "Localized in vivo 13c nmr spectroscopy of the brain.," *NMR Biomed*, vol. 16, no. 6-7, pp. 313–338, 2003.

[98] R. A. de Graaf, G. F. Mason, A. B. Patel, K. L. Behar, and D. L. Rothman, "In *vivo 1h-[13c]-nmr* spectroscopy of cerebral metabolism.," *NMR Biomed*, vol. 16, no. 6-7, pp. 339–357, 2003.

[99] M. A. Garca-Espinosa, T. B. Rodrigues, A. Sierra, M. Benito, C. Fonseca, H. L. Gray, B. L. Bartnik, M. L. Garca-Martn, P. Ballesteros, and S. Cerdn, "Cerebral glucose metabolism and the glutamine cycle as detected by in vivo and in vitro 13c nmr spectroscopy.," *Neurochem Int*, vol. 45, no. 2-3, pp. 297–303, 2004.

[100] G. F. Mason and J. H. Krystal, "Mr spectroscopy: its potential role for drug development for the treatment of psychiatric diseases.," *NMR Biomed*, vol. 19, pp. 690–701, Oct 2006.

[101] G. F. Mason, R. Gruetter, D. L. Rothman, K. L. Behar, R. G. Shulman, and E. J. Novotny, "Simultaneous determination of the rates of the tca cycle, glucose utilization, alpha-ketoglutarate/glutamate exchange, and glutamine synthesis in human brain by nmr.," *J Cereb Blood Flow Metab*, vol. 15, pp. 12–25, Jan 1995.

[102] G. F. Mason, D. L. Martin, S. B. Martin, D. Manor, N. R. Sibson, A. Patel, D. L. Rothman, and K. L. Behar, "Decrease in gaba synthesis rate in rat cortex

following gaba-transaminase inhibition correlates with the decrease in gad(67) protein.," *Brain Res*, vol. 914, pp. 81–91, Sep 2001.

[103] N. R. Sibson, A. Dhankhar, G. F. Mason, D. L. Rothman, K. L. Behar, and R. G. Shulman, "Stoichiometric coupling of brain glucose metabolism and glutamatergic neuronal activity.," *Proc Natl Acad Sci U S A*, vol. 95, pp. 316–321, Jan 1998.

[104] R. Gruetter, E. R. Seaquist, and K. Ugurbil, "A mathematical model of compartmentalized neurotransmitter metabolism in the human brain.," *Am J Physiol Endocrinol Metab*, vol. 281, pp. E100–E112, Jul 2001.

[105] V. Lebon, K. F. Petersen, G. W. Cline, J. Shen, G. F. Mason, S. Dufour, K. L. Behar, G. I. Shulman, and D. L. Rothman, "Astroglial contribution to brain energy metabolism in humans revealed by 13c nuclear magnetic resonance spectroscopy: elucidation of the dominant pathway for neurotransmitter glutamate repletion and measurement of astrocytic oxidative metabolism.," *J Neurosci*, vol. 22, pp. 1523–1531, Mar 2002.

[106] G. F. Mason, R. Gruetter, D. L. Rothman, K. L. Behar, R. G. Shulman, and E. J. Novotny, "Simultaneous determination of the rates of the tca cycle, glucose utilization, alpha-ketoglutarate/glutamate exchange, and glutamine synthesis in human brain by nmr.," *J Cereb Blood Flow Metab*, vol. 15, pp. 12–25, Jan 1995.

[107] J. Shen, "13c magnetic resonance spectroscopy studies of alterations in glutamate neurotransmission.," *Biol Psychiatry*, vol. 59, pp. 883–887, May 2006.

[108] L. Leybaert, "Neurobarrier coupling in the brain: a partner of neurovascular and neurometabolic coupling?," *J Cereb Blood Flow Metab*, vol. 25, pp. 2–16, Jan 2005.

[109] M. E. Raichle, "Cognitive neuroscience. bold insights.," *Nature*, vol. 412, pp. 128–130, Jul 2001.

[110] S. Ogawa, R. S. Menon, D. W. Tank, S. G. Kim, H. Merkle, J. M. Ellermann, and K. Ugurbil, "Functional brain mapping by blood oxygenation level-dependent contrast magnetic resonance imaging. a comparison of signal characteristics with a biophysical model.," *Biophys J*, vol. 64, pp. 803–812, Mar 1993.

[111] S. Ogawa, T. M. Lee, A. R. Kay, and D. W. Tank, "Brain magnetic resonance imaging with contrast dependent on blood oxygenation.," *Proc Natl Acad Sci U S A*, vol. 87, pp. 9868–9872, Dec 1990.

[112] R. M. Bryan, R. A. Hawkins, A. M. Mans, D. W. Davis, and R. B. Page, "Cerebral glucose utilization in awake unstressed rats.," *Am J Physiol*, vol. 244, pp. C270–C275, Mar 1983.

[113] D. L. Rothman, K. L. Behar, F. Hyder, and R. G. Shulman, "In vivo nmr studies of the glutamate neurotransmitter flux and neuroenergetics: implications for brain function.," *Annu Rev Physiol*, vol. 65, pp. 401–427, 2003.

[114] D. Nicholls and D. Attwell, "The release and uptake of excitatory amino acids.," *Trends Pharmacol Sci*, vol. 11, pp. 462–468, Nov 1990.

[115] L. Pellerin and P. J. Magistretti, "Glutamate uptake into astrocytes stimulates aerobic glycolysis: a mechanism coupling neuronal activity to glucose utilization.," *Proc Natl Acad Sci U S A*, vol. 91, pp. 10625–10629, Oct 1994.

[116] L. Pellerin and P. J. Magistretti, "Glutamate uptake stimulates na+,k+-atpase activity in astrocytes via activation of a distinct subunit highly sensitive to ouabain.," *J Neurochem*, vol. 69, pp. 2132–2137, Nov 1997.

[117] A. Schurr, J. J. Miller, R. S. Payne, and B. M. Rigor, "An increase in lactate output by brain tissue serves to meet the energy needs of glutamate-activated neurons.," *J Neurosci*, vol. 19, pp. 34–39, Jan 1999.

[118] P. J. Magistretti and L. Pellerin, "Cellular mechanisms of brain energy metabolism and their relevance to functional brain imaging.," *Philos Trans R Soc Lond B Biol Sci*, vol. 354, pp. 1155–1163, Jul 1999.

[119] M. Zonta, M. C. Angulo, S. Gobbo, B. Rosengarten, K.-A. Hossmann, T. Pozzan, and G. Carmignoto, "Neuron-to-astrocyte signaling is central to the dynamic control of brain microcirculation.," *Nat Neurosci*, vol. 6, pp. 43–50, Jan 2003.

[120] S. Mangia, G. Garreffa, M. Bianciardi, F. Giove, F. D. Salle, and B. Maraviglia, "The aerobic brain: lactate decrease at the onset of neural activity.," *Neuroscience*, vol. 118, no. 1, pp. 7–10, 2003.

[121] P. G. Mullins, L. M. Rowland, R. E. Jung, and W. L. Sibbitt, "A novel technique to study the brain's response to pain: proton magnetic resonance spectroscopy.," *Neuroimage*, vol. 26, pp. 642–646, Jun 2005.

[122] A.-L. Lin, P. T. Fox, Y. Yang, H. Lu, L.-H. Tan, and J.-H. Gao, "Time-dependent correlation of cerebral blood flow with oxygen metabolism in activated human visual cortex as measured by fmri.," *Neuroimage*, vol. 44, pp. 16–22, Jan 2009.

[123] L. K. Bak, A. Schousboe, U. Sonnewald, and H. S. Waagepetersen, "Glucose is necessary to maintain neurotransmitter homeostasis during synaptic activity in cultured glutamatergic neurons.," *J Cereb Blood Flow Metab*, vol. 26, pp. 1285–1297, Oct 2006.

[124] R. A. de Graaf and K. Nicolay, "Adiabatic water suppression using frequency selective excitation.," *Magn Reson Med*, vol. 40, pp. 690–696, Nov 1998.

[125] X. H. Zhu and W. Chen, "Observed bold effects on cerebral metabolite resonances in human visual cortex during visual stimulation: a functional (1)h mrs study at 4 t.," *Magn Reson Med*, vol. 46, pp. 841–847, Nov 2001.

[126] H. Ratiney, Y. Coenradie, S. Cavassila, D. van Ormondt, and D. Graveron-Demilly, "Time-domain quantitation of 1h short echo-time signals: background accommodation.," *MAGMA*, vol. 16, pp. 284–296, May 2004.

[127] H. Ratiney, M. Sdika, Y. Coenradie, S. Cavassila, D. van Ormondt, and D. Graveron-Demilly, "Time-domain semi-parametric estimation based on a metabolite basis set.," *NMR Biomed*, vol. 18, pp. 1–13, Feb 2005.

[128] S. W. Provencher, "Estimation of metabolite concentrations from localized in vivo proton nmr spectra.," *Magn Reson Med*, vol. 30, pp. 672–679, Dec 1993.

[129] V. Govindaraju, K. Young, and A. A. Maudsley, "Proton nmr chemical shifts and coupling constants for brain metabolites.," *NMR Biomed*, vol. 13, pp. 129–153, May 2000.

[130] I. Tk? and R. Gruetter, "Methodology of h nmr spectroscopy of the human brain at very high magnetic fields.," *Appl Magn Reson*, vol. 29, pp. 139–157, Mar 2005.

[131] E. Cabanes, S. Confort-Gouny, Y. L. Fur, G. Simond, and P. J. Cozzone, "Optimization of residual water signal removal by hlsvd on simulated short echo time proton mr spectra of the human brain.," *J Magn Reson*, vol. 150, pp. 116–125, Jun 2001.

[132] I. Tkac, J. M. Dubinsky, C. D. Keene, R. Gruetter, and W. C. Low, "Neurochemical changes in huntington r6/2 mouse striatum detected by in vivo 1h nmr spectroscopy.," *J Neurochem*, vol. 100, pp. 1397–1406, Mar 2007.

[133] S. W. Provencher, “Estimation of metabolite concentrations from localized in vivo proton nmr spectra.,” *Magn Reson Med*, vol. 30, pp. 672–679, Dec 1993.

[134] J. H. Hwang, G. D. Graham, K. L. Behar, J. R. Alger, J. W. Prichard, and D. L. Rothman, “Short echo time proton magnetic resonance spectroscopic imaging of macromolecule and metabolite signal intensities in the human brain.,” *Magn Reson Med*, vol. 35, pp. 633–639, May 1996.

[135] K. L. Behar and T. Ogino, “Characterization of macromolecule resonances in the 1h nmr spectrum of rat brain.,” *Magn Reson Med*, vol. 30, pp. 38–44, Jul 1993.

[136] M. C. McKenna, H. S. Waagepetersen, A. Schousboe, and U. Sonnewald, “Neuronal and astrocytic shuttle mechanisms for cytosolic-mitochondrial transfer of reducing equivalents: current evidence and pharmacological tools.,” *Biochem Pharmacol*, vol. 71, pp. 399–407, Feb 2006.

[137] B. A. Wandell, A. A. Brewer, and R. F. Dougherty, “Visual field map clusters in human cortex.,” *Philos Trans R Soc Lond B Biol Sci*, vol. 360, pp. 693–707, Apr 2005.

[138] R. Gruetter and I. Tkc, “Field mapping without reference scan using asymmetric echo-planar techniques.,” *Magn Reson Med*, vol. 43, pp. 319–323, Feb 2000.

[139] E. Tarasw, A. Wierci?ska-Drapa?o, B. Kubas, W. Dzienis, A. Orzechowska-Bobkiewicz, D. Prokopowicz, and J. Walecki, “Cerebral mr spectroscopy in neurologically asymptomatic hiv-infected patients.,” *Acta Radiol*, vol. 44, pp. 206–212, Mar 2003.

[140] J. A. Eckstein, G. M. Ammerman, J. M. Reveles, and B. L. Ackermann, “Analysis of glutamine, glutamate, pyroglutamate, and gaba in cerebrospinal fluid using ion

pairing hplc with positive electrospray lc/ms/ms.," *J Neurosci Methods, vol. 171,* pp. 190–196, Jun 2008.

[141] J. M. Dougherty and R. M. Roth, "Cerebral spinal fluid.," *Emerg Med Clin North Am*, vol. 4, pp. 281–297, May 1986.

[142] R. Kannan, J. F. Kuhlenkamp, M. Ookhtens, and N. Kaplowitz, "Transport of glutathione at blood-brain barrier of the rat: inhibition by glutathione analogs and age-dependence.," *J Pharmacol Exp Ther*, vol. 263, pp. 964–970, Dec 1992.

[143] R. Gruetter, K. Ugurbil, and E. R. Seaquist, "Steady-state cerebral glucose concentrations and transport in the human brain.," *J Neurochem*, vol. 70, pp. 397–408, Jan 1998.

[144] R. Gruetter, D. L. Rothman, E. J. Novotny, G. I. Shulman, J. W. Prichard, and R. G. Shulman, "Detection and assignment of the glucose signal in 1h nmr difference spectra of the human brain.," *Magn Reson Med*, vol. 27, pp. 183–188, Sep 1992.

[145] R. A. Hawkins, "The blood-brain barrier and glutamate.," *Am J Clin Nutr*, vol. 90, pp. 867S–874S, Sep 2009.

[146] J. de Boer, F. Postema, H. Plijter-Groendijk, and J. Korf, "Continuous monitoring of extracellular lactate concentration by microdialysis lactography for the study of rat muscle metabolism in vivo.," *Pflugers Arch*, vol. 419, pp. 1–6, Aug 1991.

[147] R. G. Shulman, F. Hyder, and D. L. Rothman, "Lactate efflux and the neuroenergetic basis of brain function.," *NMR Biomed*, vol. 14, no. 7-8, pp. 389–396, 2001.

[148] C. U. Niemann, R. Hirose, T. Liu, M. Behrends, J. L. Brown, D. F. Kominsky, J. P. Roberts, and N. Serkova, "Ischemic preconditioning improves energy state and transplantation survival in obese zucker rat livers.," *Anesth Analg*, vol. 101, pp. 1577–1583, Dec 2005.

[149] N. Chhina, E. Kuestermann, J. Halliday, L. J. Simpson, I. A. Macdonald, H. S. Bachelard, and P. G. Morris, "Measurement of human tricarboxylic acid cycle rates during visual activation by (13)c magnetic resonance spectroscopy.," *J Neurosci Res*, vol. 66, pp. 737–746, Dec 2001.

[150] R. Dringen, "Metabolism and functions of glutathione in brain.," *Prog Neurobiol*, vol. 62, pp. 649–671, Dec 2000.

[151] D. Han, E. Williams, and E. Cadenas, "Mitochondrial respiratory chain-dependent generation of superoxide anion and its release into the intermembrane space.," *Biochem J*, vol. 353, pp. 411–416, Jan 2001.

[152] T. L. Davis, K. K. Kwong, R. M. Weisskoff, and B. R. Rosen, "Calibrated functional mri: mapping the dynamics of oxidative metabolism.," *Proc Natl Acad Sci U S A*, vol. 95, pp. 1834–1839, Feb 1998.

[153] K. B. Beckman and B. N. Ames, "The free radical theory of aging matures.," *Physiol Rev*, vol. 78, pp. 547–581, Apr 1998.

[154] A. Kuryatov, B. Laube, H. Betz, and J. Kuhse, "Mutational analysis of the glycine-binding site of the nmda receptor: structural similarity with bacterial amino acid-binding proteins.," *Neuron*, vol. 12, pp. 1291–1300, Jun 1994.

[155] V. L. Dawson, T. M. Dawson, D. A. Bartley, G. R. Uhl, and S. H. Snyder, "Mechanisms of nitric oxide-mediated neurotoxicity in primary brain cultures.," *J Neurosci*, vol. 13, pp. 2651–2661, Jun 1993.

[156] S. D. Rao, H. Z. Yin, and J. H. Weiss, "Disruption of glial glutamate transport by reactive oxygen species produced in motor neurons.," *J Neurosci*, vol. 23, pp. 2627–2633, Apr 2003.

[157] P. A. Rosenberg, S. Amin, and M. Leitner, "Glutamate uptake disguises neurotoxic potency of glutamate agonists in cerebral cortex in dissociated cell culture.," *J Neurosci*, vol. 12, pp. 56–61, Jan 1992.

[158] S. N. Murphy and R. J. Miller, "A glutamate receptor regulates ca2+ mobilization in hippocampal neurons.," *Proc Natl Acad Sci U S A*, vol. 85, pp. 8737–8741, Nov 1988.

[159] S. Nakanishi, "Molecular diversity of glutamate receptors and implications for brain function.," *Science*, vol. 258, pp. 597–603, Oct 1992.

[160] P. H. Seeburg, "The tins/tips lecture. the molecular biology of mammalian glutamate receptor channels.," *Trends Neurosci*, vol. 16, pp. 359–365, Sep 1993.

[161] G. A. Dienel, R. Y. Wang, and N. F. Cruz, "Generalized sensory stimulation of conscious rats increases labeling of oxidative pathways of glucose metabolism when the brain glucose-oxygen uptake ratio rises.," *J Cereb Blood Flow Metab*, vol. 22, pp. 1490–1502, Dec 2002.

[162] W. Walz and S. Mukerji, "Lactate release from cultured astrocytes and neurons: a comparison.," *Glia*, vol. 1, no. 6, pp. 366–370, 1988.

[163] S. Mangia, I. A. Simpson, S. J. Vannucci, and A. Carruthers, "The in vivo neuron-to-astrocyte lactate shuttle in human brain: evidence from modeling of measured lactate levels during visual stimulation.," *J Neurochem*, vol. 109 Suppl 1, pp. 55–62, May 2009.

[164] W. G. Kuhr, C. J. van den Berg, and J. Korf, "In vivo identification and quantitative evaluation of carrier-mediated transport of lactate at the cellular level in the striatum of conscious, freely moving rats.," *J Cereb Blood Flow Metab*, vol. 8, pp. 848–856, Dec 1988.

[165] W. Walz and S. Mukerji, "Lactate release from cultured astrocytes and neurons: a comparison.," *Glia*, vol. 1, no. 6, pp. 366–370, 1988.

[166] W. Oldendorf, L. Braun, and E. Cornford, "ph dependence of blood-brain barrier permeability to lactate and nicotine.," *Stroke*, vol. 10, no. 5, pp. 577–581, 1979.

[167] T. L. Spencer and A. L. Lehninger, "L-lactate transport in ehrlich ascites-tumour cells.," *Biochem J*, vol. 154, pp. 405–414, Feb 1976.

[168] L. Pellerin and P. J. Magistretti, "Glutamate uptake into astrocytes stimulates aerobic glycolysis: a mechanism coupling neuronal activity to glucose utilization.," *Proc Natl Acad Sci U S A*, vol. 91, pp. 10625–10629, Oct 1994.

[169] L. Pellerin, A.-K. Bouzier-Sore, A. Aubert, S. Serres, M. Merle, R. Costalat, and P. J. Magistretti, "Activity-dependent regulation of energy metabolism by astrocytes: an update.," *Glia*, vol. 55, pp. 1251–1262, Sep 2007.

[170] L. Pellerin and P. J. Magistretti, "Food for thought: challenging the dogmas.," *J Cereb Blood Flow Metab*, vol. 23, pp. 1282–1286, Nov 2003.

[171] C. P. Chih, P. Lipton, and E. L. Roberts, "Do active cerebral neurons really use lactate rather than glucose?," *Trends Neurosci*, vol. 24, pp. 573–578, Oct 2001.

[172] C.-P. Chih and E. L. R. Jr, "Energy substrates for neurons during neural activity: a critical review of the astrocyte-neuron lactate shuttle hypothesis.," *J Cereb Blood Flow Metab*, vol. 23, pp. 1263–1281, Nov 2003.

[173] G. A. Dienel and N. F. Cruz, "Neighborly interactions of metabolically-activated astrocytes in vivo.," *Neurochem Int*, vol. 43, no. 4-5, pp. 339–354, 2003.

[174] C.-P. Chih and E. L. R. Jr, "Energy substrates for neurons during neural activity: a critical review of the astrocyte-neuron lactate shuttle hypothesis.," *J Cereb Blood Flow Metab*, vol. 23, pp. 1263–1281, Nov 2003.

[175] I. A. Simpson, A. Carruthers, and S. J. Vannucci, "Supply and demand in cerebral energy metabolism: the role of nutrient transporters.," *J Cereb Blood Flow Metab*, vol. 27, pp. 1766–1791, Nov 2007.

[176] G. F. Mason, D. L. Rothman, K. L. Behar, and R. G. Shulman, "Nmr determination of the tca cycle rate and alpha-ketoglutarate/glutamate exchange rate in rat brain.," *J Cereb Blood Flow Metab*, vol. 12, pp. 434–447, May 1992.

[177] G. F. Mason, R. Gruetter, D. L. Rothman, K. L. Behar, R. G. Shulman, and E. J. Novotny, "Simultaneous determination of the rates of the tca cycle, glucose utilization, alpha-ketoglutarate/glutamate exchange, and glutamine synthesis in human brain by nmr.," *J Cereb Blood Flow Metab*, vol. 15, pp. 12–25, Jan 1995.

[178] Y. Shen, T. J. Connor, Y. Nolan, J. P. Kelly, and B. E. Leonard, "Differential effect of chronic antidepressant treatments on lipopolysaccharide-induced depressive-like behavioural symptoms in the rat.," *Life Sci*, vol. 65, no. 17, pp. 1773–1786, 1999.

[179] N. Chhina, E. Kuestermann, J. Halliday, L. J. Simpson, I. A. Macdonald, H. S. Bachelard, and P. G. Morris, "Measurement of human tricarboxylic acid cycle rates during visual activation by (13)c magnetic resonance spectroscopy.," *J Neurosci Res*, vol. 66, pp. 737–746, Dec 2001.

[180] R. B. Duckrow and R. M. Bryan, "Regional cerebral glucose utilization during hyperglycemia.," *J Neurochem*, vol. 48, pp. 989–993, Mar 1987.

[181] F. Chapa, F. Cruz, M. L. Garca-Martn, M. A. Garca-Espinosa, and S. Cerdn, "Metabolism of (1-(13)c) glucose and (2-(13)c, 2-(2)h(3)) acetate in the neuronal and glial compartments of the adult rat brain as detected by [(13)c, (2)h] nmr spectroscopy.," *Neurochem Int*, vol. 37, no. 2-3, pp. 217–228, 2000.

[182] J. Chateil, M. Biran, E. Thiaudire, P. Canioni, and M. Merle, "Metabolism of [1-(13)c]glucose and [2-(13)c]acetate in the hypoxic rat brain..," *Neurochem Int*, vol. 38, pp. 399–407, Apr 2001.

[183] P.-G. Henry, G. Adriany, D. Deelchand, R. Gruetter, M. Marjanska, G. Oz, E. R. Seaquist, A. Shestov, and K. U?urbil, "In vivo 13c nmr spectroscopy and metabolic modeling in the brain: a practical perspective.," *Magn Reson Imaging*, vol. 24, pp. 527–539, May 2006.

[184] R. Gruetter, K. Ugurbil, and E. R. Seaquist, "Steady-state cerebral glucose concentrations and transport in the human brain.," *J Neurochem*, vol. 70, pp. 397–408, Jan 1998.

[185] R. Gruetter, E. R. Seaquist, and K. Ugurbil, "A mathematical model of compartmentalized neurotransmitter metabolism in the human brain.," *Am J Physiol Endocrinol Metab*, vol. 281, pp. E100–E112, Jul 2001.

[186] P.-G. Henry, V. Lebon, F. Vaufrey, E. Brouillet, P. Hantraye, and G. Bloch, "Decreased tca cycle rate in the rat brain after acute 3-np treatment measured by in vivo 1h-[13c] nmr spectroscopy.," *J Neurochem*, vol. 82, pp. 857–866, Aug 2002.

[187] R. Gruetter, E. R. Seaquist, and K. Ugurbil, "A mathematical model of compartmentalized neurotransmitter metabolism in the human brain.," *Am J Physiol Endocrinol Metab*, vol. 281, pp. E100–E112, Jul 2001.

[188] R. Gruetter, K. Ugurbil, and E. R. Seaquist, "Steady-state cerebral glucose concentrations and transport in the human brain.," *J Neurochem*, vol. 70, pp. 397–408, Jan 1998.

[189] I. Y. Choi, S. P. Lee, S. G. Kim, and R. Gruetter, "In vivo measurements of brain glucose transport using the reversible michaelis-menten model and simultaneous measurements of cerebral blood flow changes during hypoglycemia.," *J Cereb Blood Flow Metab*, vol. 21, pp. 653–663, Jun 2001.

[190] I. Y. Choi, S. P. Lee, S. G. Kim, and R. Gruetter, "In vivo measurements of brain glucose transport using the reversible michaelis-menten model and simultaneous measurements of cerebral blood flow changes during hypoglycemia.," *J Cereb Blood Flow Metab*, vol. 21, pp. 653–663, Jun 2001.

[191] J. Moore, M. Jankiewicz, H. Zeng, A. W. Anderson, and J. C. Gore, "Composite rf pulses for b1+-insensitive volume excitation at 7 tesla.," *J Magn Reson*, vol. 205, pp. 50–62, Jul 2010.

[192] E. de Alba and N. Tjandra, "Interference between cross-correlated relaxation and the measurement of scalar and dipolar couplings by quantitative j.," *J Biomol NMR*, vol. 35, pp. 1–16, May 2006.

[193] H. Hu and A. J. Shaka, "Composite pulsed field gradients with refocused chemical shifts and short recovery time.," *J Magn Reson*, vol. 136, pp. 54–62, Jan 1999.

[194] R. A. de Graaf, "Theoretical and experimental evaluation of broadband decoupling techniques for in vivo nuclear magnetic resonance spectroscopy.," *Magn Reson Med*, vol. 53, pp. 1297–1306, Jun 2005.

[195] R. Gruetter, E. R. Seaquist, and K. Ugurbil, "A mathematical model of compartmentalized neurotransmitter metabolism in the human brain.," *Am J Physiol Endocrinol Metab*, vol. 281, pp. E100–E112, Jul 2001.

[196] N. Chhina, E. Kuestermann, J. Halliday, L. J. Simpson, I. A. Macdonald, H. S. Bachelard, and P. G. Morris, "Measurement of human tricarboxylic acid cycle rates during visual activation by (13)c magnetic resonance spectroscopy.," *J Neurosci Res*, vol. 66, pp. 737–746, Dec 2001.